
**Mass spectrometric investigation and determination
of proteome composition of human skin tissues
ablated using picosecond infrared laser (PIRL) in a
'layer by layer' approach**

Dissertation with the aim of achieving a doctoral degree

Doctor rerum naturalium (Dr. rer. nat.)

at the Faculty of Mathematics, Informatics and Natural Sciences

Department of Chemistry

University of Hamburg

Submitted by

Parnian Kiani, M. Sc.

from Ahvaz, Iran

Hamburg

2019

Recommendation of the evaluators for the dissertation:

Supervisor: Prof. Dr. Hartmut Schlüter

Co-advisor: Prof. Dr. Dr. Christian Betzel

Date of Disputation: 22.03.2019

This work was done from January 2015 until June 2018 in the department of clinical chemistry at University Medical Centre Eppendorf, Hamburg (UKE) in the working group of mass spectrometric proteome analytics, under the supervision of Prof. Dr. Hartmut Schlüter.

Dedicated to my lovely mother and father, the best brother of the world and my better half, my fiancée.

Abstract

Skin anatomy, its composition of abundant proteins, and the functions of these proteins are greatly established and explored. The proteome including lower abundant proteins in each type of cell layers of skin – particularly in the five different cell layers of the epidermis - are not accurately defined. The main goal of this study was the investigation of human skin proteomes in all cell layers and determination of protein composition layer-by-layer in the epidermis. Therefore, a proteomic approach was undertaken after ablating the skin tissue layer-by-layer by using an innovative, homogenization method called DIVE (desorption by impulsive vibrational excitation) using PIRL (picosecond infra-red laser). This method is based on absorption of laser energy that induces an excitation of intramolecular vibrational modes of water molecules in the cell at 3 μm Wavelength and leads to blast biomolecules out of tissues on a picosecond timescale in the gas phase. This laser ablates tissues with minimal or no damage because of its ultrafast energy transfer that cannot be converted into thermal energy or in shock waves during this short time. Another aim was to find out if PIRL can replace the conventional, mechanical homogenization methods such as disrupting tissues using bead milling through high-speed shaking with stainless steel beads (in this study termed as: TissueLyser) or grinding/milling of tissues using a mortar and pestle plus liquid nitrogen (in this study termed as grinder & LN₂). Due to the need of generating a protein marker library for each main domains of the human skin tissue: epidermis and dermis, both layers had to be separated by enzymatical treatment using dispase II. The separated epidermis and dermis tissues were homogenized mechanically with either TissueLyser or with grinder & LN₂ as well as with the novel homogenization method PIRL-DIVE. The proteins were analyzed by tandem mass spectrometry (MS/MS) in a bottom-up approach. With the help of existing databases “THE HUMAN PROTEIN ATLAS”, protein markers were verified and categorized. When comparing the number of proteins identified in conventional homogenization methods to those identified in PIRL, the highest number of dermal proteins and the best reproducibility and protein recovery was observed with the PIRL approach. In terms of mass spectrometric proteome identification with classical methods averagely 550 proteins could be identified in dermal tissues whilst with PIRL, about 900 proteins were identified. In the case of epidermal tissues, the protein yields in both conventional, mechanical as well as in PIRL homogenization techniques were quite similar, whereas the reproducibility rate of proteins identified in PIRL-ablated epidermal tissues was higher than in conventional methods. Not forgetting, the contamination risk was reduced by PIRL because of an ultrafast homogenization and less sample preparation steps. Furthermore, the goal of the study was achieved by ablating the human skin tissue layer by layer (approximately 15 μm ablation depth per ablated layer) and

determining the protein composition in each ablated cell layer using tandem mass spectrometry.

Zusammenfassung

Hautanatomie, deren abundante Proteine sowie ihre Funktionen sind zum großen Teil erforscht. Die Proteome unter Berücksichtigung weniger abundanter Proteine in verschiedenen Schichten der Haut, die unterschiedliche Zelltypen beinhalten, insbesondere die Proteome der fünf Schichten verschiedener Zelltypen in der Epidermis, sind nicht genau definiert. Das Hauptziel dieser Studie war die Erforschung der menschlichen Hautproteome in allen Zellschichten und die Bestimmung der Proteinzusammensetzung Schicht für Schicht in der Epidermis. Daher wurde eine massenspektrometrische Proteom-Analyse durchgeführt, um Hautgewebe Schicht für Schicht abzutragen, mit einer Extraktions- und Homogenisierungsmethode namens DIVE (Desorption durch impulsive Schwingungsanregung) unter Verwendung eines Pikosekunden-Infrarotlasers (PIRL). Diese Methode basiert auf der Absorption von Laserenergie durch die Wassermoleküle in der Zelle, die bei 3 µm Wellenlänge eine Anregung intramolekularer Schwingungsmoden ihrer Atome induziert und dazu führt, dass gesamte Zellen zerrissen und in einer Pikosekunden-Zeitskala aus dem Gewebe in der Gasphase gesprengt werden. Dieser Laser zeichnet sich durch die sehr sanfte Ablation von Geweben aus. Zellen, die direkt an die Ablationszone angrenzen bleiben intakt. Dies geschieht aufgrund einer ultraschnellen Übertragung der Laser-Energie, die in dieser kurzen Zeit nicht in thermische Energie oder in Stoßwellen an die Zellen in der Umgebung abgegeben wird. Das zusätzliche Ziel dieser Arbeit bestand darin, herauszufinden, ob PIRL die konventionellen, mechanischen Homogenisierungsmethoden ersetzen kann, z. B. das Aufbrechen von Geweben mit der Kugelmühle durch Hochgeschwindigkeitsschütteln mit Edelstahlperlen (in dieser Arbeit bezeichnet als TissueLyser) oder Mahlen von Geweben mit Mörser und Pistill in Gegenwart von flüssigem Stickstoff (in dieser Arbeit bezeichnet als Grinder & LN₂). Aufgrund der Notwendigkeit eine Proteinmarker-Bibliothek für Epidermis und Dermis zu erstellen, wurden beide Haut-Schichten durch enzymatische Behandlung unter Verwendung von Dispase II getrennt. Die beiden voneinander getrennten Hautgeweben, Epidermis und Dermis, wurden entweder mit TissueLyser oder mit Grinder & LN₂ mechanisch homogenisiert bzw. mit der neuen Homogenisierungsmethode PIRL-DIVE. Die Proteine wurden mittels Bottom-Up-Proteomics analysiert. Mit Hilfe der Datenbanken "The Human Protein Atlas" wurden die Dermis bzw. Epidermis-Proteinmarker verifiziert und kategorisiert. Beim Vergleich der Anzahl der mit konventionellen Homogenisierungsmethoden identifizierten Proteine mit denen, die in PIRL als Homogenisierungsverfahren identifiziert wurden, wurden mit PIRL die höchste Anzahl an dermalen Proteinen und die beste Reproduzierbarkeit und Proteinwiederherstellung beobachtet. In Bezug auf die massenspektrometrische Proteom-Identifizierung mit klassischen Methoden konnten durchschnittlich 550 Proteine in dermalen Geweben identifiziert werden, während mit PIRL rund 900 Proteine identifiziert wurden. Im Fall

von Epidermisgeweben waren die Proteinausbeuten sowohl bei konventionellen, mechanischen als auch bei PIRL-Homogenisierungstechniken ziemlich ähnlich, während die Reproduzierbarkeit von Proteinen identifiziert in den mit PIRL-abgetragenen Epidermisgeweben höher lag als bei herkömmlichen Verfahren. Nicht zu vergessen, dass das Kontaminationsrisiko durch die ultraschnelle Homogenisierung und weniger Probenvorbereitungsschritte durch PIRL reduziert wurde. Darüber hinaus wurde das Ziel der Studie erreicht, indem das Gewebe der menschlichen Haut in jeweils ca. 15 µm dicken Schichten abgetragen wurde und die Proteinzusammensetzung in jeder abgetragenen Schicht mit Hilfe der Bottom-Up-Proteomanalyse bestimmt wurde.

List of published papers:

1. Khosh-Naucke, M., Becker, J., Mesén-Ramírez, P., **Kiani, P.**, Birnbaum, J., Fröhlke, U., Jonscher, E., Schlüter, H., Spielmann, T., Identification of novel parasitophorous vacuole proteins in *P. falciparum* parasites using BioID. *International Journal of Medical Microbiology* 308 (2018) 13-24.
2. Kwiatkowski, M., Wurlitzer, M., Krutilin, A., **Kiani, P.**, Nimer, R., Omid, M., Mannaa, A., Bussmann, T., Bartkowiak, K., Kruber, S., Uschold, S., Steffen, P., Lübberstedt, J., Küpker, N., Petersen, H., Knecht, R., Hansen, N.O., Zarrine-Afsar, A., Robertson, W.D., Miller, R.J., Schlüter, H. (2016) Homogenization of tissues via picosecond-infrared laser (PIRL) ablation: Giving a closer view on the in-vivo composition of protein species as compared to mechanical homogenization. *J Proteomics*. 16 (134):193-202.

Poster presentations:

1. Poster presentation in 50th Annual meeting of the German Society of Mass Spectrometry (DGMS), "Proteomic investigation of skin cell layers by tissue ablation using picosecond infrared laser (PIRL)", Feb – March 2017, Kiel, Germany.
2. Poster presentation in 49th Annual meeting of the German Society of Mass Spectrometry (DGMS), "A proteomic workflow for characterization of human skin biopsies by using picosecond infrared laser (PIRL)", Feb – March 2016, Hamburg, Germany.
3. Poster presentation in 48th Annual meeting of the German Society of Mass Spectrometry (DGMS), "Displacement chromatography as enrichment step in phosphoproteomics", Feb – March 2015, Wuppertal, Germany.

Table of contents

Abstract	5
Zusammenfassung	7
List of published papers:	9
Poster presentations:	9
Table of contents	10
List of abbreviations	13
1 Introduction	15
1.1. Skin and Skinomics	15
1.2. Proteins as biomolecules and proteomics	19
1.2.1. Proteome and protein species.....	19
1.2.2. Proteomics	19
1.3. Homogenization methods	21
1.3.1. Conventional/mechanical homogenization methods.....	21
1.3.2. Picosecond infrared laser (PIRL) homogenization method.....	21
1.4. Background to dispase treatment	23
2 Aim of the study	25
3 Methods and materials	26
3.1. Biopsy collection and sample preparation	26
3.1.1. Collecting of human skin biopsies	26
3.1.2. Dispace separation of epidermal and dermal layers for protein library generation	26
3.1.3. Sample preparation of dispase-separated dermis and epidermis prior to PIRL-DIVE ablation or mechanical homogenization	27
3.2. Library generation for epidermis and dermis layers	28
3.2.1. Classical homogenization methods: TissueLyser and grinder & liquid nitrogen 29	
3.2.1.1. TissueLyser.....	29
3.2.1.2. Grinder & Liquid nitrogen (grinder & LN ₂)	29
3.2.2. PIRL-DIVE ablation and homogenization of skin tissues	30
3.2.2.1. Construction of sample target, trapping system, and PIRL set-up	30

3.2.2.2.	PIRL-DIVE Homogenization of dispase-separated dermis and epidermis	34
3.2.3.	PIRL-DIVE ablation and homogenization of skin biopsies layer-by-layer	34
3.2.3.1.	Parameter optimization of PIRL	34
3.2.3.2.	Layer-by-layer ablation of skin tissues with the optimized laser parameters	36
3.3.	Protein extraction using different extraction buffers	37
3.3.1.	Urea-extraction protocol:	37
3.3.2.	SDC-extraction protocol:	38
3.3.3.	SDC&Urea-extraction protocol:	38
3.4.	In-solution tryptic digestion	39
3.4.1.	Urea-digestion protocol:	39
3.4.2.	SDC-digestion protocol:	39
3.4.3.	SDC&Urea-digestion protocol or Wiśniewski et al.:	40
3.5.	LC-MS/MS analysis	40
3.6.	Data analysis	41
3.7.	Cryosections with cyrocut, H&E staining and microscopy	42
3.8.	Materials	43
3.8.1.	Chemicals and (bio-) materials	43
3.8.2.	Equipment	44
3.8.3.	Softwares	45
4	Results and discussion	46
4.1.	Results of homogenized of dispase-separated skin tissues	46
4.1.1.	Results of homogenized dispase-separated skin tissues by TissueLyser	48
4.1.2.	Results of homogenized dispase-separated skin tissues by grinder & LN ₂	50
4.1.3.	Comparison of both conventional, mechanical homogenization methods: TissueLyser (TL) and grinder & LN ₂	51
4.1.4.	Comparison between different extraction buffers for both mechanical homogenization methods	55
4.1.5.	Results of homogenized dispase-separated skin tissues by PIRL ablation	62
4.1.6.	Comparison between mechanical and PIRL-DIVE homogenization methods	70
4.2.	Generation of the library for protein markers of dermis & epidermis	72
4.3.	The distinction between breast and abdominal skin biopsies	81
4.4.	PIRL ablation and homogenization of skin biopsies layer-by-layer	86
4.4.1.	Parameter optimization of PIRL	86
4.4.1.1.	Experiment PIRL optimization I:	86
4.4.1.2.	Experiment PIRL optimization II:	87
4.4.1.3.	Experiment PIRL optimization III:	91
4.4.1.4.	Experiment PIRL optimization IV:	95

4.4.2.	Layer-by-layer ablation of skin tissues with the optimized laser parameters ..	100
4.4.2.1.	Experiment PIRL layer-by-layer I:	100
4.4.2.2.	Experiment PIRL layer-by-layer II:	116
5	Conclusion and outlooks	129
6	References	131
7	Risk and safety statements	139
8	Supplement	141
9	Acknowledgment	157
10	Declaration	158

List of abbreviations

Abbreviation	Meaning
2DE	two-dimensional gel electrophoresis
ACN	Acetonitrile
AmbiCa	ammonium bicarbonate, NH ₄ OH
<i>area_{elli.}</i>	area of ellipse
AU	absorbance Unit
BCA	bicinchoninic acid
categ.	Category
CID	collision-induced dissociation
CIEF	capillary isoelectric focusing
CO ₂	carbon dioxide
DBPS	dulbecco's phosphate buffered saline
DDA	data-dependent acquisition
DIA	data-independent acquisition
dist.	Distilled
DIVE	desorption by impulsive vibrational excitation
DTT	Dithiothreitol
<i>Ep</i>	pulse energy
EtOH	Ethanol
Er:YAG	erbium YAG, erbium-doped yttrium aluminium garnet, Er:Y ₃ Al ₅ O ₁₂
ESI	electrospray ionization
FA	formic acid
FASP	filter-aided sample preparation
FWHM	full width at half maximum
G&LN ₂	grinder & liquid nitrogen
GO	Gene Ontology
h	Hour
H ₂ O	Water
H&E	hematoxylin and eosin
HCD	higher-energy collisional dissociation
HPLC	high performance liquid chromatography
Hz	Hertz
IAA	Iodoacetamide
ICH	Immunohistochemistry
IT	ion trap
J/cm ²	joule per square centimeter
K	Kilo
λ	wave length
L	Liter
Laser	light amplification by stimulated emission of radiation
LC	liquid Chromatography
LN ₂	liquid nitrogen

μ	micro-
m	milli-
M	Molar
min	Minutes
MeOH	Methanol
MS	mass spectrometry
MS/MS	tandem mass spectrometry
MudPIT	multidimensional protein identification technology
N ₂	nitrogen, N ₂
Nd:YAG	neodymium-doped yttrium aluminum garnet; Nd:Y ₃ Al ₅ O ₁₂
Nd:YLF	neodymium-doped yttrium lithium fluoride; Nd: LiYF ₄
OCT	optical coherence tomography
O-H	hydrogen bond
OPA	optical parametric amplifier
OT	Orbitrap
φp	peak pulse fluence
PIRL	picosecond infrared laser
ps	Picosecond
PSM	number of peptide spectrum matches
PTFE	Teflon® polytetrafluoroethylene
PTM	post-translational modification
Q	Quadrupole
rcf	relative centrifugal force
<i>reprod_{rate}</i>	reproducibility rate
RP-LC	reversed phase liquid chromatography
rpm	rotation per minutes
SDC	sodium deoxycholate
SDS	sodium dodecyl sulfate
sec	Second
TEAB	triethylammonium bicarbonate
TFA	trifluoroacetic acid
TLB	tissue lysis buffer
UPLC	ultra high-performance liquid chromatography
UV	ultraviolet
W	Watt
w	woman (female)

1 Introduction

1.1. Skin and Skinomics

Skin is the largest organ in humans, covering the body of an average adult with 1.8 m² – [1], having fascinating properties and functions. The skin qualifies the first line barrier protection of the internal organs and systems from the external environment. It can react uniquely to each type of various environmental stresses (ultraviolet light, chemical reagents, infectious microorganisms, and further stimuli such as allergens) to keep the biological equilibrium constantly [2]. Also, it possesses of immense regenerative capacity and enormous durability [1].

The skin is segmented in two main structural layers; *epidermis* and *dermis* [3]. In some literature, the *subcutaneous* fat layer (also called *hypodermis*) is mentioned as the third skin layer which insulated the dermis from the inner organs.

Dermis as a cell-poor layer comprises of two parts (figure 1) [7]. The thin upper part is called “*papillary dermis*” (papillary and subpapillary dermal layers), made up largely thin, fine network of fibrous connective tissue: collagens, elastin and fibrillin which are responsible for elasticity, firmness and strength of skin, also fibroblasts, sensory nerve endings, and blood capillaries. That all support the epidermis with required nutrients. The papillary dermis is delimited from epidermis by the dermo-epidermal junction “basal membrane”, but also called basal lamina, basement membrane with a thickness of 100 nm as the thinnest protein layer in the human skin. [1,5,6]

The thick bottom part of the dermis is called “*reticular dermis*” with predominantly sweat glands for regulating the body temperature, sebaceous glands for producing oily secretion, hair follicles as well as blood and lymphatic vessels and connective tissue. In contrast to the fine networked fibers in the papillary dermis, it is composed of tough, dense bundle.

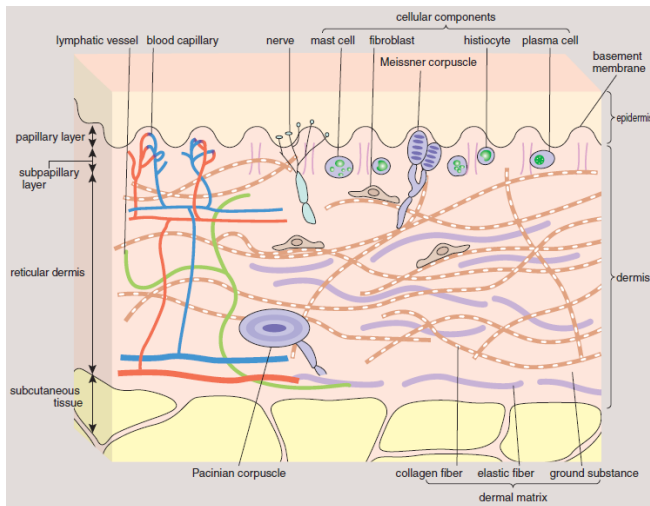


Figure 1: Structure of dermal layer in skin built up of papillary (and subpapillary) dermis and reticular dermis [48]. Dermis is surrounded by epidermis and subcutaneous tissue from top to bottom. 70 – 80% of the dry weight of the skin comprises collagens [8,9].

The most superficial layer of the skin is called the epidermis with its main function being protecting the body from external invasion and infection, and additionally sealing in moisture. In an average adult, the regenerative process in epidermis happens every 28 days by completely renewing itself from the stratum basale to the outermost layer of epidermis (stratum corneum) constantly [1] (figure 2).

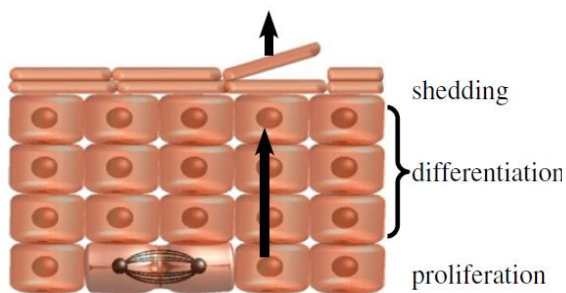


Figure 2: self-renewing of skin cell layers in epidermis. Proliferation and differentiation of keratinocytes, also called “keratinization”, proceed from basal layer up to superficial layer of skin, subsequently the shedding of corneocytes called “desquamation” takes place [13].

The stem cells in the basal layer provide the terminal differentiation, also known as keratinization [11]. They replace 80 billion keratinocytes during the renewal cycles of epidermis [1], and 70% of these cells (by dry weight) contain keratins [10]. The keratinocytes undergo a slow and programmed cell death by step-by-step movements through the various epidermis layers up to the surface of the skin. These densely growing stratified squamous epithelium cells, generate in stratum corneum water-impermeable cell layers which consists of flattened, anucleate, dead cells called corneocytes and they are surrounded by a protein shell called “cornified envelopes” [1,7]. Once the cells reach the top of the stratum corneum, then they start shedding – known as “desquamation” step –, thus the cell proliferation rate in the

basal layer is kept balanced. According to the desquamation, approximately 30,000 to 40,000 dead cells are scaling off from human skin, estimated to be about 1.5 g of scale cells daily [11,12]. A scaffold of patterned lipid lamellae located in the extracellular membrane between the corneocytes, create the barrier function of skin [11]. In figure 3, the major cells and lipids existing in the epidermis are illustrated. The Merkle cells, found just in stratum basale, exist in few numbers, relatively to their function in few numbers and are receptors for tactile sense. Scattered Melanocytes are responsible for brown to black pigmentation of skin due to melanin. And dendritic Langerhans cells as macrophages defend the body against toxins and microbes that penetrate the skin.

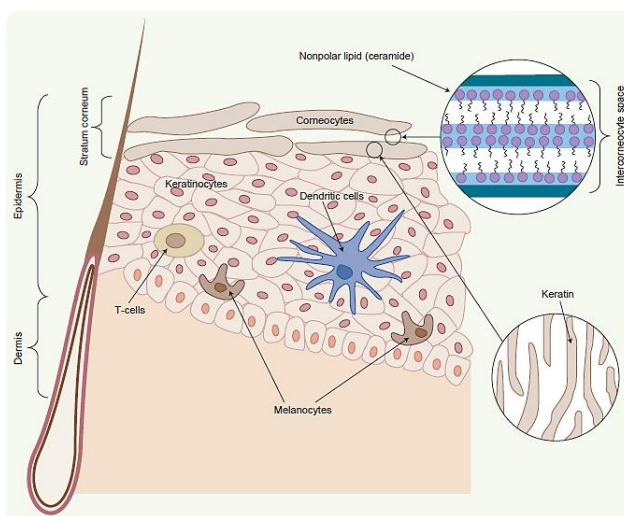


Figure 3: Structure of major cells and Lipids in epidermis layers [2]. Melanocytes and dendritic Langerhans cells dispersed in stratum spinosum and granulosum. Keratinocytes and corneocytes accrued from stem cells in stratum basale, and lipids e.g. nonpolar ceramides in intercorneocyte space.

The epidermis is arranged in four (five, just in thick skin domains) zones (figure 4). As mentioned above, the epidermis is separated from the dermis by the dermo-epidermal junction, the basal membrane. The cell division (mitosis) of stem cells in basal cell layer give rise to keratinocytes in upper layers of the epidermis. The stratum spinosum is the thickest living cell layer of epidermis in most skin area. It contains newly built keratinocytes but also cells, in the deepest part of this layer, which still undergo still mitosis.

The stratum granulosum consists of granular cells with distinct nucleus but dying membranes. They contain keratohyalin granules for binding together the intermediate keratin filaments. The stratum lucidum exists exclusively in thick skin areas – palms and soles – as a transition zone between stratum granulosum and stratum corneum. It builds up flattened dead cells (corneocytes) containing eleidin (an intermediate product of keratins). The “stratum corneum” as described above is the outermost barrier of skin containing nonpolar lipid-rich cornified envelopes and soluble proteins such as loricrin, involucrin, envoplakin and periplakin. The cornified envelopes build a protein shell around the corneocytes [4].

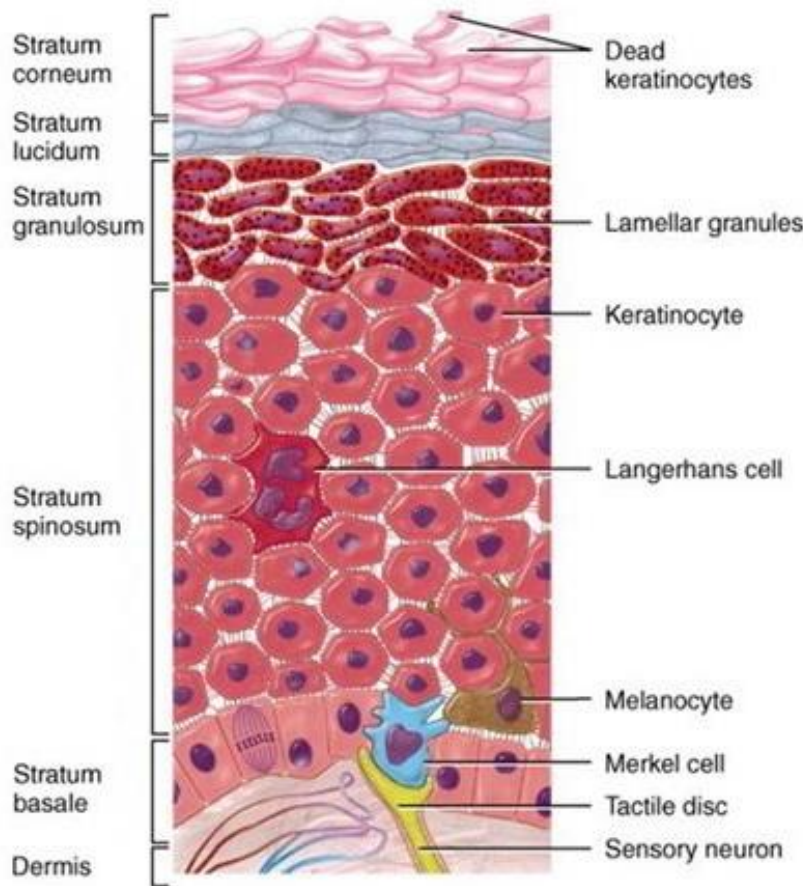


Figure 4: Strata of the epidermis. “*Stratum basale*“: mitotic process of stem cells give rise to keratinocytes in superficial strata – keratinization –, but also contains Merkel cells as receptor for touching sense; “*stratum spinosum*“: several layers of keratinocytes which produce keratin filaments; “*stratum granulosum*“: 3 to 5 layers of keratinocytes with dying membranes, contains keratohyalin granules and lamellar bodies which release lipids and proteins; “*stratum lucidum*“: dead cells containing dispersed keratohyalin, found just in thick skin: palms and soles; “*stratum corneum*“: around 30 layers of dead cells with hard protein envelopes called cornified envelopes, containing keratins and lipids which function as barrier

protection of skin; shedding or desquamation of dead corneocytes is the last step of epidermis differentiation [49].

Skin anatomy, protein structures, and their functions but also transcriptomics are established and explored in great part. Nonetheless, for better understanding how the skin and the skin barrier is affected by different diseases or/and by pharmaceutical ingredients or cosmetic agents, it's required to understand the complex composition of skin proteomes [3] in all five types of cell layers in epidermis and as well as in dermis.

1.2. Proteins as biomolecules and proteomics

1.2.1. Proteome and protein species

The proteome caught on since 1994 as the analogy to the term genome (emerged in 1920 by H. WINKLER [14]) developed by MARK R. WILLKINS [15]. A proteome is the entirety of all proteins thought to be synthesized by the complement genome of an organism at a specific time dependent on its localization. Aside from the fact that by the transcription of the genes and the alternative splicing a variety of mRNAs with diverse compositions can occur, during protein biosynthesis a whole range of chemical and/or enzymatic reactions can take place e.g. diverse derivatizations of proteins (phosphorylation, ubiquitination, glycosylation, etc.) and proteolytic cleavages of amino acid chains [16]. According to the literature, about 600 post-translational modifications (PTMs) are included in the UNIMODE database [17]. Each of these possible reactions, from the beginning of the transcription to the translation step, leads to the genesis of the smallest unit of the proteome the *protein species* [18] or *proteoforms* [19] as defined by JUNGBLUT et al. in 1996 [18]. The protein species differ in their chemical composition and also in their structure and function. The number of protein species is valued at ~1 billion that was calculated as 4,000 existing cell types multiplied by 25 protein species appraised for each one of ~10,000 genes counted in the human genome [19]. Consequently, the proteome exists as a multifold dimension of its underlying genome in consequence of all post-transcriptional and post-translational modifications [20]. Due to the dynamic range of the proteomes the complexity of the identification of proteomes increases accordingly. The analysis of post-translationally modified proteins is extremely complicated in comparison to their original form due to their low abundance in the cell or tissue or organism.

1.2.2. Proteomics

Proteins are greatly involved in biological pathways and protein-protein-interactions show their significance as ultimate triggers and/or effectors in cellular reactions. Therefore, the study of proteomes, called proteomics, gained an importance in the last decades. Proteomics enables the identification of biologically, prognostically and diagnostically relevant biomarkers. Furthermore, proteomics in combination with transcriptomic allows for analysis, and quantitative proteomic technologies clear assertions about disease mechanisms as well as discovery of therapeutically usable agents [31]. Mass spectrometry-based proteomics provides a simultaneous qualitative and quantitative investigation of proteomes based on their diverse

physicochemical attributes. This aids in detailed structure clarification, function and differentiation between biological features in healthy and disease states [20].

Mass spectrometry-based proteomic approaches enable high-throughput analysis of complex mixtures of proteomes in a single sample. This technology enables the investigation of thousands of peptides and their modifications by using Liquid chromatography coupled to tandem mass spectrometry (LC-MS/MS) [21].

The qualitative and quantitative analysis of complex proteomes requires either separation on protein or peptide level to decrease the complexity and the range of abundance by enrichment and/or fractionation. There are two main approach lines in proteomics: top-down [22] and bottom-up [23] (also called shot-gun termed by YATES et al. [23]). The top-down approach differs in two types of measurements: in which the intact proteoforms are separated, measured and characterized while maintaining their structure and property; and in which the proteins are firstly separated and subsequently proteolytic digested and measured [17, 24]. In this case, mostly two-dimensional gel electrophoresis (2DE) [25], but also reversed-phase liquid chromatography (RP-LC) [24, 26] and capillary isoelectric focusing (CIEF) [24, 27] techniques are applied to perform top-down based protein analysis. Bottom-up on the other hand is the most widely used approach for proteins sequence identification – as well as PTMs-determination. In this approach, an extremely complex protein mixture can be proteolytically digested into peptides prior to separation and measurement which allows a fast, simultaneous analysis of thousands of parent proteins [28]. Recently, about 10,000 proteins could be identified by sequentially filling of the quadrupole-Orbitrap mass analyzer with peptide ions of different mass ranges. This is termed as the BoxCar and has opened a new and improved side to the bottom-up approach [29]. However, due to the high dynamic range of proteoforms multidimensional protein identification technology (MudPIT) [30] with a two- or triphasic column system has turned out to be a solution to decrease the complexity of samples. This is possible by fractionation across different physico-chemical properties of peptides by the law of mass action – binding, retaining and eluting to and from different types of stationary phases.

1.3. Homogenization methods

1.3.1. Conventional/mechanical homogenization methods

Sample preparation for proteome analysis requires diverse equipment to achieve homogenous cell wall disruption. Currently, the most common homogenization techniques are based on the mechanical procedures to reduce the particle size of the samples by blending, mixing, shearing, beating, grinding, sonicating, etc. [32, 33]. The choice of proper homogenization technique depends on the type of analytes and also on the underlying biological objectives. The final goal of a homogenization step within the scope of sample preparation is to release the biomolecules into solution and achieve a homogenate with precise, high throughput and reproducible results.

One of the conventional mechanical homogenization techniques currently in use is the freezing of tissues (mostly shock freezing using liquid nitrogen) and subsequently grinding with a traditional mortar and pestle until the cell walls are sufficiently disrupted. Another common method is based on bead-disruption: applying stainless steel, tungsten carbide or glass beads [34] (different size and diameter available for various target-aimed applications) in a high-speed shaker to homogenize the tissue. Similar to the former, the use of liquid nitrogen has proven to be effective to increase the shearing force on samples, but also enzymatic lysis buffers raise the velocity of releasing biomolecules. One of the advantages of these methods is its availability in every laboratory. Furthermore, the handling and working with the equipment are uncomplicated. Disadvantages are the limited numbers, size and volumes of samples which can be prepared by this time-consuming procedure. Additionally, it continually runs the risk of cross-contamination which is not avoidable by a mechanical homogenization method.

1.3.2. Picosecond infrared laser (PIRL) homogenization method

An innovative laser system was developed by R. J. DWAYNE MILLER in 2009 [35], called the *picosecond infrared laser* (PIRL) [36]. This laser system contrasts strongly in its properties from the conventional laser systems such as CO₂ or Er:YAG. As known, conventional laser systems have increased the versatility and speed enormously in medical areas in the last decades since 1960 [37]. PIRL is distinguished by way of the laser energy desorption by water molecules at a certain wavelength and pulse duration. The physico-chemical properties of water molecules opened a novel aspect in laser physics which is also the key element of the design concept for this novel technology. PIRL uses a Neodymium-doped yttrium lithium fluoride (Nd:YLF, [35]) lasing medium. That, with a home-built laser optics construction, allows

a pulse duration in the picosecond range. The bundled laser emissions produces in Nd:YLF medium in the infrared range feature a wavelength of 2.95 μm which excites the water molecules. Figure 5 shows the corresponding vibrational excited states of water molecules achieved after the adsorption of infrared energy. After the vibrationally excited O-H stretching modes at 3400 cm^{-1} follows the relaxation to the ground states while the excess energy of O-H stretch is transferred to high frequency intermolecular librational motions of the hydrogen bond network [38].

This energy transfer occurs in 200 fs and a relaxation to the hot ground state by considering all librational and translational motions within 1 ps [35, 39]. Due to these short lifetimes of excited vibrational modes and fast relaxation processes in water molecules, using PIRL with picosecond pulses leads to an ultrafast irradiation of targeted samples within the adsorb laser energy cannot be exchanged into thermal energy in this short time period.

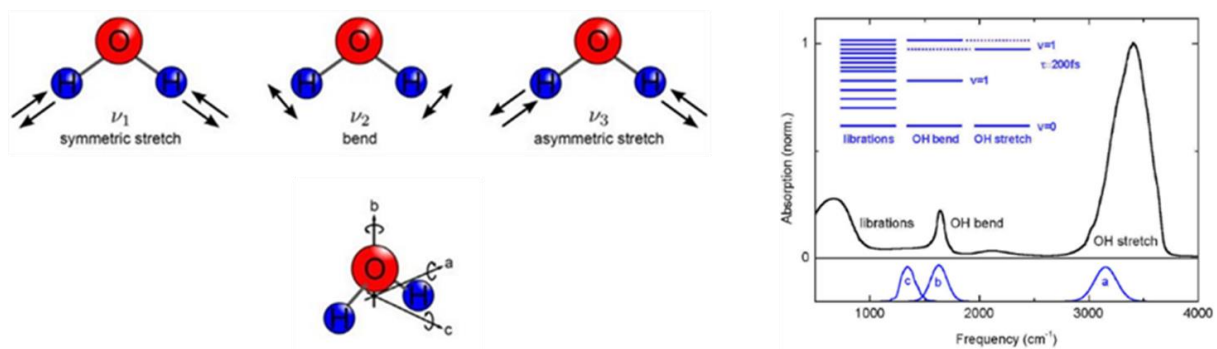


Figure 5: Left: Water molecules with degrees of freedoms (3N-6): three vibrational, rotational and translational motions (in x, y, z). The vibrational modes are characterized by Symmetric stretching mode: ν_1 3657 cm^{-1} , Bending mode: ν_2 1595 cm^{-1} , and Asymmetric stretching mode: ν_3 3756 cm^{-1} [50]. Right: a schematic Jablonski diagram of vibrational states and the infrared absorption spectrum of liquid water molecules: a) high-frequency librations, b) O-H bending c) O-H stretching vibrational modes including the decay times τ for excited states [51].

Consequently, the water molecules are excited and co-blast the targeted tissues in the gas phase without a temperature rising and thereby avoiding thermal damage. This is therefore referred to as a cold photomechanical ablation [40] or cold vaporization [41] (figure 6). The mechanism of PIRL with $\lambda = 2.95\ \mu\text{m}$ and 300 ps pulse duration to drive ablation of tissues containing water molecules is hence called “*desorption by impulsive vibrational excitation* (DIVE)” [42].

The idea of design and development of PIRL was in urgent need of a laser system for scar-free surgery. This is to better preserve the tissue structure in contrast to the conventionally

available laser systems [36, 40, 43, 44, 46] or even electro-surgical device or the common scalpel [45] in medical applications. PIRL with its cold vaporization can be applied as a gentle homogenization method for proteomic approaches by rapidly transferring the biomolecules from the (solid or fluid) state into the gas phase [47]. The homogenization of proteins with conventional methods consist of several critical, time-consuming steps with the risk of proteolytic processes occurring, accordingly changing the chemical composition of proteins and modifying or creating new protein species during each step. Introducing new protein species with artefacts during the sample preparation is not preventable and these are not distinguishable from inherent modifications which could lead to false positives. Therefore, the PIRL stands out as an ultrafast and soft homogenization method, with minimal to no additional protein modifications and this enables analysis in a near in-vivo state of the biopsies [41].

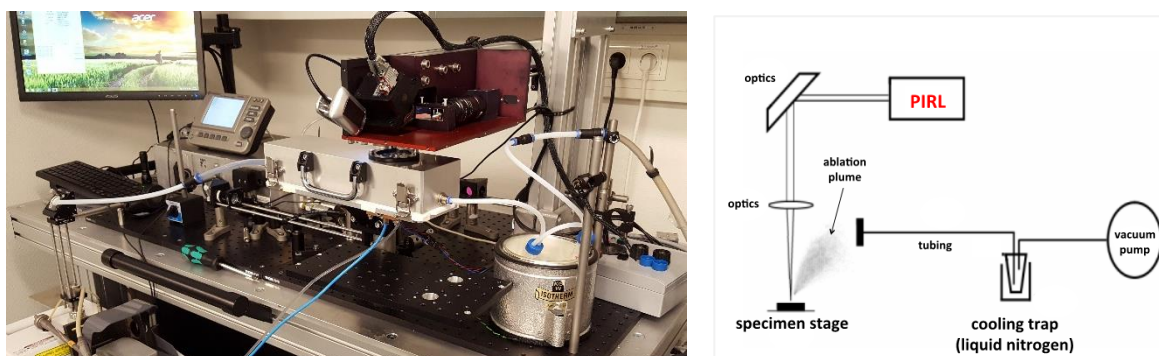


Figure 6: *Left:* experimental set up of picosecond infrared laser PIRL. *Right:* sketch of PIRL guided to a closed and cooled to -10 °C chamber equipped with a copper sample target. Induced aerosol during PIRL ablation, which includes all biomolecules, is sucked into a cooling trap using PTFE tubing system and vacuum pump. The aerosol starts to condensate in the Falcon® tube placed in liquid nitrogen immediately.

1.4. Background to dispase treatment

Dermatologists have been developing methods for destruction or ablation of diseased skin tissues for therapeutic purposes for over a century now. According to the technology timeline and the therapeutic issue, these methods can vary from a surgical scalpel, electro scalpel, cryosurgery, to diverse common laser ablation systems. These are able to ablate epidermal tissues but are however linked with danger to damage the deeper skin structure unavoidably, leaving significant scarring. Besides these, chemicals and proteolytic treatments are a further solution to ablate diseased tissue, chemicals such as trichloroacetic acid (TCA) with phenol and proteases such as trypsin and dispase are applied for topical protease therapy [52].

Dispase is a bacterial protease – isolated from *Bacillus polymyxa* – which cleaves epidermis from the dermis with the basal cell layer almost is maintained [53]. Once the bond between fibronectin in the basal membrane and the collagen IV in the dermal zone is broken, the epidermal sheet can be easily peeled from the papillary dermis using forceps [54]. The dispase digestion of skin tissue for 24 hours (shown in figure 7) results in dermo-epidermal separation while retaining epithelial rete ridges (also called rete pegs) pattern of skin [53, 97].

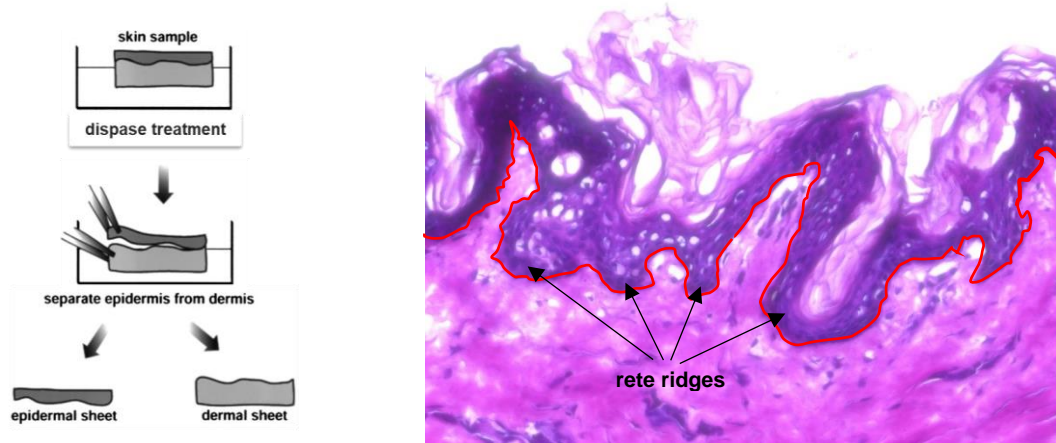


Figure 7: *Left:* a schematic illustration of dispase treatment with outcome dermo-epidermal separation resulted into the isolation of intact epidermal and dermal sheets [103]. *Right:* Histology of skin biopsy with hematoxylin and eosin (H&E) staining. Red line shows the area where the dispase protease attacks and cleaves the connection of fibronectin in an epidermal extracellular matrix in basal membrane and collagen IV in the dermis. The epithelial rete ridges maintain by the treatment and allow a dissociation with less epidermal damage and intact dermal stroma.

The dispase treatment or digestion is mostly used by isolation of fibroblasts or keratinocytes cell cultures. Therefore, it is the method of choice for separating the epidermis from the dermis, maintaining the intact protein structure in both layers with no damages. In this study, it enables the generation of a protein library for each separated sheet via mass spectrometry analysis.

2 Aim of the study

The aim of this thesis was to investigate and determine the proteome composition of human skin by a layer-by-layer technique using a bottom-up approach with liquid chromatography tandem mass spectrometry (LC-MS/MS) analysis and using picosecond infrared laser (PIRL) for the tissue ablation. With the innovative homogenization method, called PIRL-DIVE (desorption by impulsive vibrational excitation), the tissue ablation will be done. The picosecond infrared laser (PIRL) radiation blasts biomolecules out of tissues on a picosecond timescale in the gas phase, which allows an ablation of tissue with minimal to no thermal damage of tissue. The efficiency and reproducibility of this homogenization method will be compared to two existing classical, mechanical homogenization methods (mentioned in this study as TissueLyser and grinder & LN₂). For this, the results of mass spectrometry will be used and with the obtained protein compositions and protein yields the comparison between both classical homogenization methods and PIRL-DIVE method will be carried out.

Although the skin proteomes are of paramount importance for the body, but comparable to other human organs and body fluids, few proteomic studies and datasets for skin layers exist [4], therefore, a further proteomic approach will be performed to create a protein library for epidermis as well as for dermis, which will be separated by an enzymatical treatment.

The protein composition in the cell layers of the epidermis of skin will be determined by a layer-by-layer tissue ablation with PIRL-DIVE. For this investigation, the laser parameters will be optimized primarily to achieve the thinnest possible ablation layer. A further aim will be the optimization of the sample preparation protocol for extraction of proteins out of the borosilicate filter to increase the yields of extracted proteins compared to the existing extraction protocols, which will be compared in this study as well.

3 Methods and materials

3.1. Biopsy collection and sample preparation

3.1.1. Collecting of human skin biopsies

Fresh human skin biopsies were collected from plastic surgeries of female patients in breast and abdomen reduction surgeries. The samples were tested for HIV and hepatitis HBV and HCV viruses by the certified Tissue Solutions company (Glasgow, Scotland). The fresh biopsies were delivered at 4 – 8 °C to Beiersdorf (Hamburg, Germany). The tissues were washed with 1x DPBS and cut using a scalpel, forceps and a pair of scissors into portions for different experiments. All the prepared samples described in the following paragraph were stored at -80 °C until when needed. The naming of samples in this study reads as follows: e.g. 38w indicates a 38-year-old female donor.

3.1.2. Dispase separation of epidermal and dermal layers for protein library generation

Due to the need of a protein marker library for each main domains of human skin tissue: epidermis and dermis, both layers had to be separated by dispase treatment. For dispase digestion, biopsies were cut in very tiny long strips with 1 mm thickness. The small strips were washed firstly in 70% ethanol, two times in (1x) DPBS and finally two times in dispase buffer (dispase II dissolved in PBS, 2.4 U/mL). They were then incubated in dispase at 4 °C overnight. After digestion, the epidermis could be peeled off the dermis by mechanical stress using forceps. Some of the separated epidermis tissues was placed on the glass slides prepared for PIRL ablation. The rest of the separated pieces of epidermis and dermis were stored in 2 mL Eppendorf tubes.

3.1.3. Sample preparation of dispase-separated dermis and epidermis prior to PIRL-DIVE ablation or mechanical homogenization

For optimizing laser parameters: the skin biopsies were cut into approximately 5x4 cm portions. The subcutaneous fat layer was removed using scissors. One of the skin biopsies was prepared separately with dermatome (a surgical instrument) and a 4cmx4cmx200µm tissue portion was cut. The samples were fixed on the top of cork plates using pins and put inside Petri dishes.

Additionally, ca. 1.0x1.0 cm and 1.5x1.5 cm biopsies, placed in biopsy capsules (CellPath CellSafe+White biopsy capsules, Fischer Scientific), were also ablated. For layer-by-layer PIRL ablation of skin cell layers: the biopsies were cut again into ca. 1.5x1.5 cm pieces and were placed into biopsy capsules (see supplement: S.1).

3.2. Library generation for epidermis and dermis layers

For generating a protein marker library, skin tissues were separated in dermal and epidermal sheets using dispase treatment. The samples were homogenized either classically using a TissueLyser and grinder in combination with liquid nitrogen (LN₂), or with the new laser ablation method: PIRL-DIVE (described in chapter 1.3.2). The sheets of epidermis and dermis were treated separately as shown in figure 8.

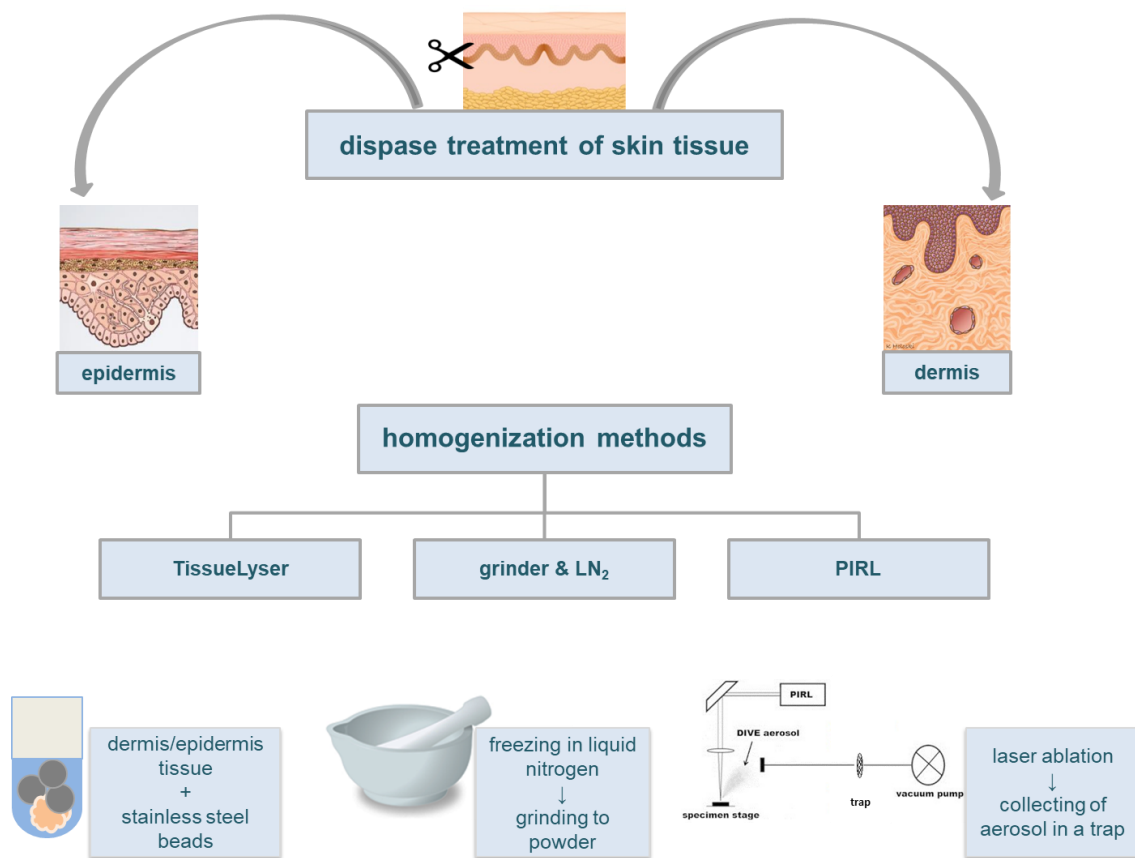


Figure 8: Schematic representation of homogenization methods after dispase treatment of skin biopsies in their main layers: epidermis and dermis. TissueLyser: the separated epidermis/dermis tissues were added to the stainless-steel beads and lysis buffer. The disruption and simultaneously homogenization of samples were achieved through high-speed shaking with beads, which grind tissues. Grinder & LN₂: the separated epidermis/dermis tissues were frozen with liquid nitrogen (LN₂) and then milled using a mortar and pestle using a circular motion with downward pressure. PIRL or Picosecond infra-red Laser: the separated epidermis/dermis tissues were ablated using PIRL via desorption by impulsive vibrational excitation (DIVE) method. Using the wavelength 3 μm and a pulse width of ~300 ps the water molecules and tissue were vaporized and sublimated immediately. The aerosol includes biomolecules (e.g. proteins, DNA, metabolite, lipids, etc.), which is collected in a trap by vacuuming.

Protein extraction for all methods was performed with two tissue lysis buffer (TLB) for a wider protein extraction range, which is described in chapter 3.4. After protein extraction, the tryptic digestion followed and then mass spectrometric analysis. From the mass spectrometry results, two lists were generated for epidermal and dermal proteins and validated in “THE HUMAN PROTEIN ATLAS” database [67]. In the next chapters, from homogenization methods to the mass spectrometry analysis are specified.

3.2.1. Classical homogenization methods: TissueLyser and grinder & liquid nitrogen

Frozen epidermis and dermis tissues separated by dispase digestion were homogenized by using two conventional homogenization methods. a bead mill (using TissueLyser) or a grinder with liquid nitrogen (grinder & LN₂ or G&LN₂).

3.2.1.1. TissueLyser

The tissues were put in a 2 mL tubes and 500 µL of TLB (chapter 3.4) was added. To the reaction tube with epidermis tissue, just one stainless-steel bead was added while two beads were used for dermis tissue. The bead mill (TissueLyser II, Qiagen) was processed at 30 Hz frequency for 3:30 minutes per one cycle. The dermis tissue was rubbery and difficult to homogenize in comparison to the soft epidermal tissues. Therefore, bead milling was repeated 5 to 7 times depending on the homogenization result. After homogenization the samples were ready for protein extraction and subsequent proteolytic digestion (more on that in chapter 3.4 and 3.5).

3.2.1.2. Grinder & Liquid nitrogen (grinder & LN₂)

For the second homogenization method the frozen tissues were put inside a porcelain mortar. While incrementally adding liquid nitrogen (LN₂), the sample was ground until a powder was achieved. Here too, the homogenization of dermis caused difficulties and grinding took a while to get almost a homogenized powder. The powder was transferred into a 2 mL tube. After homogenization, the samples were ready for protein extraction step and subsequently proteolytic digestion (more on that in chapter 3.4 and 3.5).

3.2.2. PIRL-DIVE ablation and homogenization of skin tissues

3.2.2.1. Construction of sample target, trapping system, and PIRL set-up

Frozen epidermis and dermis tissues separated by dispase digestion were homogenized by an innovative laser system developed by DWAYNE MILLER *et al.* supported by Max Planck Institute for Structure and Dynamics of Matter in Hamburg, Germany [35]. In this method as described in chapter 1.3.2, the cold vaporization is deployed for ablating tissues from their solid state directly into the gas phase, with no to minimum damage in biomolecule structures which is simultaneously an ultra-fastest method to homogenize tissues.

The samples were placed in a chamber. There was two generation of the chamber. The first generation (see supplement: S.2) was a semi-closed system, with an orifice on the top for the laser irradiation, and two further orifices; one for the junction to vacuum tubing system and another one for a better air permeable dynamic. The chamber was equipped with a copper target, that could be cooled using dry ice manually for a short period of time. However, this system was semi-closed; therefore, instead of a laminar airflow, turbulent airflow was generated. The aerosol could encounter the chamber surface and some of the biomolecules could be adsorbed to the walls of chamber.

The second chamber generation (figure 9) with an advantageous aerodynamics was designed and developed by MILLER *et al.* The key reason for the design of a new chamber was to provide a laminar air flow, so that the resulting aerosol upon ablation can be directed to the sample trap by pressure lower than atmospheric pressure without adhesion to the surface of chamber walls. The drop-shaped internal space of the chamber allows the airflow to pass through the tubing system without formation of turbulent streaming, which means a higher yield of aerosol (including the biomolecules of interest). This base cavity with an irregular airfoil shape is based on the BERNOULLI effect of the aerodynamic concept [96]. The air flow dynamic plays a great role in gain of ablated tissue; therefore, the new special chamber enables the PIRL ablation with less loss of homogenized tissue through its fluid dynamic. To reduce the air humidity, a molecular sieve was affixed to the chamber with the PTFE tubing system. Also, this chamber was equipped with a copper plate. Additionally, it owned a water-cooled condenser, which was set at -10 °C during all laser ablations.

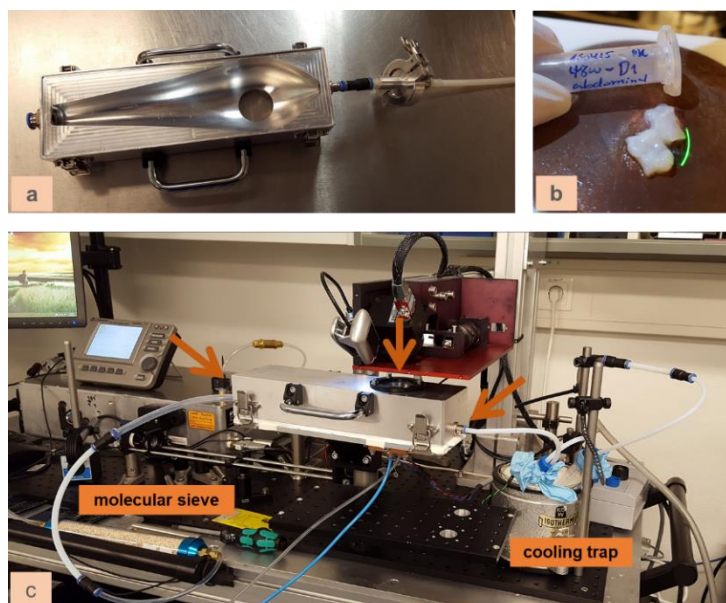


Figure 9: 2nd generation of the chamber with copper sample target. Second chamber generation: a closed system with a drop-shaped lid (with an irregular airfoil shape based on the aerodynamic concept) (a), an inlet with a special glass permeable for laser irradiation, an orifice connected to a molecular sieve (c) for controlled air permeable dynamic without air humidity, another orifice connected to the trap (c) from there to the vacuum pump. The sample target equipped with a copper plate (b) and the temperature were set to $-10\text{ }^{\circ}\text{C}$.

The chamber was connected with a tubing system through a sample collection trap system, to a vacuum pump. With a low vacuum, the aerosol was drawn to the trap. In the last four years of this study, an improvement of the trap system was implemented steadily. The first system was a cooling trap, where a 15 mL falcon was placed into a Dewar vessel filled with liquid nitrogen (LN₂). Two holes to serve as tube inlets were created on the top of the lid of falcon. The aerosol sucked in was condensed at the bottom of falcon and was frozen immediately (shown in figure 10, left). To reduce the risk of some molecules passing through tubes to the vacuum pump without condensation in the falcon, a second cooling trap with 15 mL falcon was connected in a row to increase the yield of condensed aerosol (shown in figure 10, right).

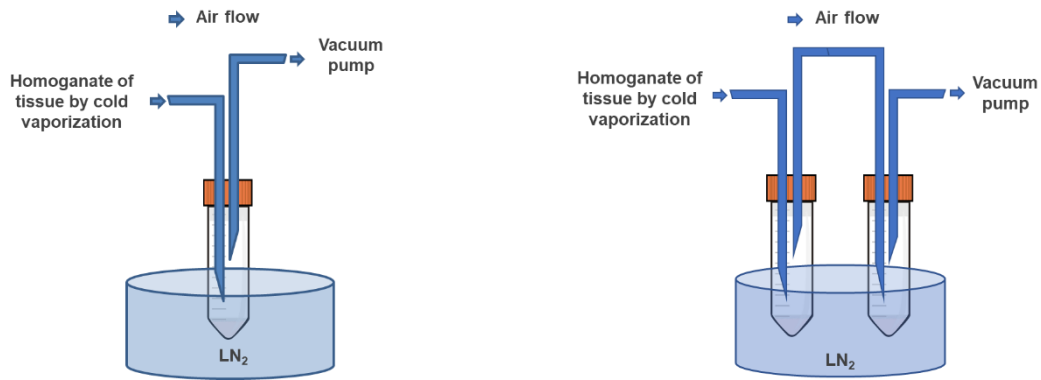


Figure 10: Optimization of traps for collecting the aerosol. *left:* the first generation of cooling trap: a 15 mL Falcon hanging in a Dewar filled with liquid nitrogen for aerosol condensation. *right:* the second generation of cooling trap: two 15 mL Falcon connected to each other with PTFE tubes for better control of aerosol collection with less loss through the vacuum pump.

This cooling trap setup led to a huge loss of homogenate hence a new design was necessary. To increase the yield as also create a straightforward handling and transport of the aerosol, a new trap was built. The structural design of the trap – designed and developed by SCHLÜTER *et al.* – is shown in figure 11. This trap was composed of a clamping ring and two rubber hose adapters with an outer diameter of 4.0 cm and an inner diameter of 2.4 cm. From one side of one of the rivets, a grate was mounted where a borosilicate filter paper was attached and therefore it was termed a filter holder. The diameter of the attached filter paper was 2.4 cm. From the backside of the grate, the filter holder apparatus was connected with the PTFE tube to the vacuum pump. Between the two rubber hose adapters, a rubber seal was fixed for achieving a better vacuum. From the front side of the filter paper, the tube connected the trap to the ablation chamber, the aerosol collected on the top of borosilicate filter paper and dried immediately.

The trap had quite a vast size in comparison to the small amount of ablation plume. Therefore, a miniaturized filter holder was designed and developed by SCHLÜTER *et al.* For the miniature filter holder, a screwing bolt system was utilized. Two hose barbs were screwed to a thread double hex nut. In the middle of the apparatus, a steel grate was mounted to the hex nut from one side. The filter paper was clutched between the top of the grate and the next hose barb. The diameter of the filter paper in the new trap was about 0.6 cm. The tubes were connected as well as described above for the first filter holder. Between the hex nut and hose barbs, a rubber seal was fixed.

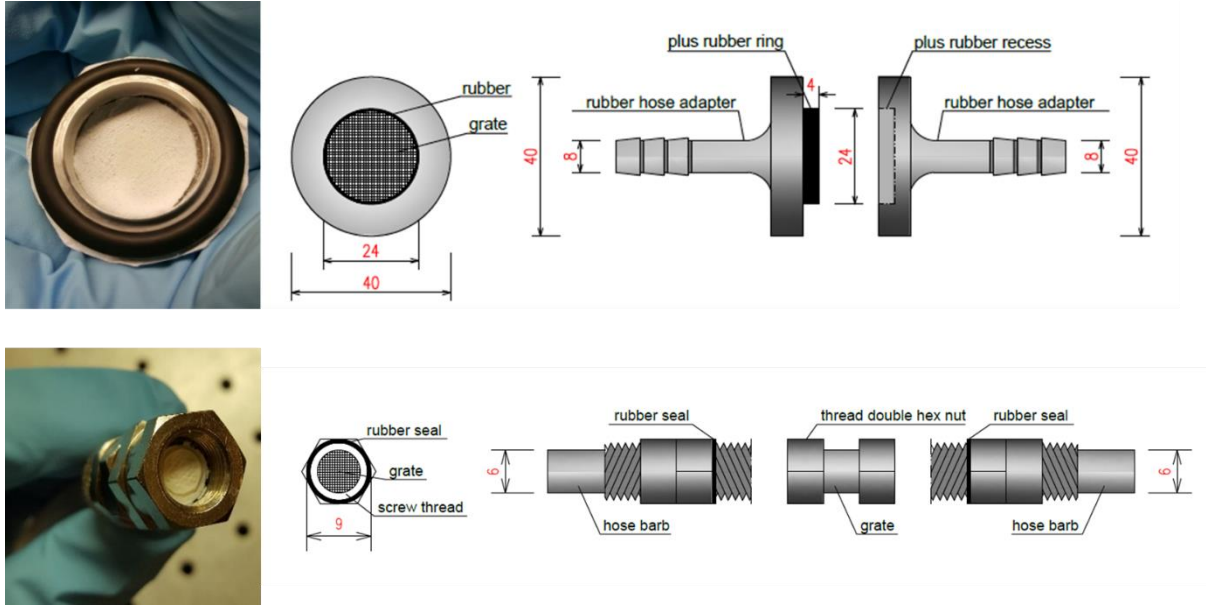


Figure 11: Both models of the filter holder, top the first filter holder with clamping ring and special rivets and below the miniature model with hex nut and fasteners. Left: photographs of both filter holders (first generation and the miniaturized one), the borosilicate filter papers are implanted in both holders (with collected homogenate); right: structural designs of interior space of both filter holders.

The picosecond infrared laser system used Nd:YLF medium with a pulse duration in picosecond range. The first generated wavelength was $1.00 \mu\text{m}$. The wavelength was increased to $3.00 \pm 0.05 \mu\text{m}$ using an optical parametric amplifier (OPA). At about 1.00 kHz pulse repetition rate and 300 ps pulse duration, the tissue ablation was operated. The autofocus of the laser beam was calibrated to the sample target for each measurement series. The laser beams consisted of spots. These spots had an elliptic shape. With the equation (1) the area of the ellipse was calculated while the a and b were the diameters of the elliptic spot. With the equation (2) the peak pulse fluence φ_p was calculated subsequently with the pulse energy E_p .

$$area_{ellip.} = \frac{a}{2} \frac{b}{2} \pi \quad (1)$$

$$\varphi_p = \frac{E_p}{area_{ellip.}} \quad (2)$$

3.2.2.2. PIRL-DIVE Homogenization of dispase-separated dermis and epidermis

The dermis and epidermis samples were homogenized with the PIRL system. The samples were placed into the chamber onto $-10\text{ }^{\circ}\text{C}$ cooled copper target using a tweezer and irradiated with the maximum laser energy. The dermis tissues were small bean-sized, with pieces while the epidermis tissues were transparent, thin layers. The aerosols collected into a falcon were shocked frozen immediately in liquid nitrogen during the condensation process. They were transported after ablation on dry ice to the $-80\text{ }^{\circ}\text{C}$ freezer until the further sample preparation was required. For those collected on borosilicate filter paper, the papers were inserted in 1.5 mL Eppendorf tubes and were transported at room temperature and were stored in $-20\text{ }^{\circ}\text{C}$ freezer.

3.2.3. PIRL-DIVE ablation and homogenization of skin biopsies layer-by-layer

For layer-by-layer ablation of skin tissues, the PIRL parameters had to be optimized. Therefore, the samples fixed on a cork plate were used here. In the following subchapters, the experiments for parameter optimization are discussed in detail.

3.2.3.1. Parameter optimization of PIRL

Experiment PIRL optimization I: Breast skin tissue with dimension $5\text{cm}\times 4\text{cm}$ fixed on a cork plate was used here. The PIRL was at its maximum laser power with 420 mW . As shown in figure 12, the laser beam was aligned from on top of the tissue and guided manually from top to bottom and bottom to top row by row. The scan duration was about 30 seconds. The aerosol was sucked by vacuum into the cooling trap and was condensed in a falcon in liquid nitrogen. This was repeated twice on the same ablated area and the plumes were collected each time in a new falcon. The collected plumes were digested and analyzed by mass spectrometry as described in chapter 3.5. The tissue was cut with cryocut in thin sections and the sections were stained using hematoxylin and eosin (H&E staining) (chapter 3.7) and subsequently the images were taken using a fluorescence microscope.

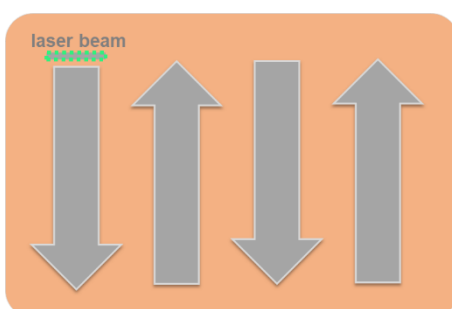


Figure 12: Experiment PIRL optimization I – layer-by-layer ablation of skin tissues. From top to bottom and from bottom to top of skin tissue the ablation was done row by row (3 times) with 420 mW laser power. The scan duration was about 30 seconds.

Experiment PIRL optimization II: Due to the results obtained from experiment PIRL optimization I, two further breast skin tissues from one patient were used with six different laser energy levels. One skin tissue, 5cmx4cm in size was fixed on a cork plate while the other was cut as 4cmx4cmx200 μ m. The same laser energy was applied to both tissues. The laser energy levels were adjusted from the maximum possible energy (~390 μ J per pulse) to the minimum (~140 μ J per pulse) to define the best laser energy with as thin ablation depth as possible (shown in figure 13). The aerosol was collected in a falcon. After ablation, the tissues were stored directly in biopsy capsules in 4% PFA and were sent for microscopy to DR. DENNIS EGGERT (in Heinrich-Pette-Institute (HPI), Hamburg, Germany). The depth of ablation was measured by confocal laser scanning microscope using collagen autofluorescence for the first tissue 5cmx4cm in size and using fluorescence dyeing for the second tissue (dermatome tissue) 4cmx4cmx200 μ m in size.

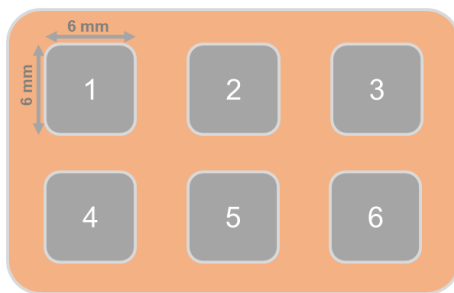


Figure 13: Experiment PIRL optimization II – six different laser pulse energies from maximum to the minimum. Both skin tissues were ablated (normal and 200 μ m dermatome tissues). Six ablation sections (6x6 mm area) were chosen for each laser energy. (1) 387 μ J; (2) 334 μ J; (3) 291 μ J; (4) 253 μ J; (5) 195 μ J; (6) 142 μ J.

Experiment PIRL optimization III: With respect to the results of experiment PIRL optimization II, the laser energy levels with the thinnest ablation depth were defined narrower here. For this purpose, a skin tissue in size 5x5 cm fixed on cork plate was ablated with three different pulse energy levels and each energy was repeated twice on the same tissue as shown in figure 14. The square scan area was about 7mmx7mm. The pulse energies were adjusted between ~190 μ J to ~140 μ J. The ablation aerosol was collected in a falcon. The samples were stored in biopsy capsules in 4% PFA immediately after ablation and sent for imaging with confocal laser scanning microscopy.



Figure 14: Experiment PIRL optimization III – three different laser pulse energies for defining optimized laser parameter for preferably thinnest ablation deepness. Adjusted pulse energies (1a&1b) 144 μ J; (2a&2b) 166 μ J; (3a&3b) 184 μ J.

Experiment PIRL optimization IV: Regarding the results of experiment PIRL III, the experiment was repeated with the same range of laser energy levels but with tissues from patients of different ages. An area of about 7.5x7.5 cm was ablated with the laser energy levels between ~180 μJ to ~140 μJ (figure 15). Each energy value was used for two tissues of different ages. The spot diameter was 200 μm and the grid spacing 10 μm . The ablation plume was collected in a falcon. The tissue was cut with cryocut in 6 μm sections and stained using hematoxylin and eosin (H&E staining) (chapter 3.7) for fluorescence microscope.

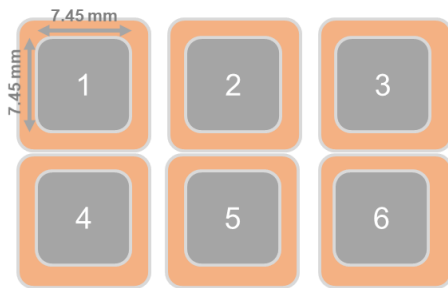


Figure 15: Experiment PIRL optimization IV – three different laser energies for ablation of six tissues from four different donors (23, 33, 56, 61 years old donors). Each energy was chosen for two tissues. Adjusted pulse energies (1&2) 180 μJ ; (3&4) 161 μJ ; (5&6) 142 μJ .

3.2.3.2. Layer-by-layer ablation of skin tissues with the optimized laser parameters

Experiment PIRL layer-by-layer I: The optimized laser parameters were implemented in the next experiments: the layer-by-layer ablation of cell layers in skin tissues. Two biological biopsies (1cmx1cm, from two female patients; two technical replicates of one sample and three technical replicates of the other) were ablated with the laser energy 140 μJ , a square scan area 7x7 mm, spots diameter 145 μm , grid spacing 10 μm and an ablation duration about 11 sec. After the first ablation was done and the plume was collected into a falcon (immersed in liquid nitrogen), the second ablation was done on the same area and the plume was collected again in a new falcon (figure 16). The plume was digested and analyzed subsequently via mass spectrometry as described in chapter 3.5.

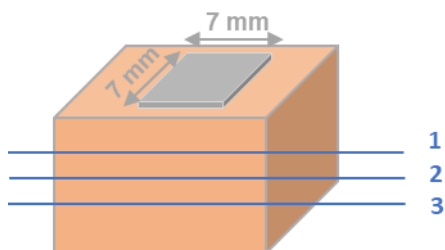


Figure 16: Experiment PIRL layer-by-layer I: Ablation of skin cell layers with optimized parameters. Two biological samples (in total 5 technical replicates) were ablated with 140 μJ laser energy per pulse. 3D-sketch visualizes the tissue block; gray cubic illustrates the ablation area (7x7 mm), two times (for some samples three times) the tissue is scanned on the same selected domains.

Experiment PIRL layer-by-layer II: Layer-by-layer ablation was repeated for six other biological samples. The ablation was done with an output energy of 135 μJ per pulse. The spot diameter was about 200 μm and grid spacing 10 μm . From the spot diameter, the peak pulse fluence was calculated with a value of 1.1 J/cm^2 regarding equation (2) in chapter 3.2.2.1. To achieve a high protein yield six domains of each skin tissue was scanned with the PIRL. The ablation area for each square domain was about 4.7x4.4 mm. The scan duration pro area was 7 sec. The laser beam was guided manually from one square to the next square. The plume was vacuumed to the filter holder (generation 1) and was dried on the borosilicate filter paper immediately. After the first ablation, the filter paper was removed and put in to a 1.5 mL tube. Then the second ablation followed above the same ablated area and the plume was collected on a new filter paper and put in a new 1.5 mL tube. The samples were stored in $-20\text{ }^\circ\text{C}$ until the sample preparation prior to mass spectrometry as described in chapter 3.5.

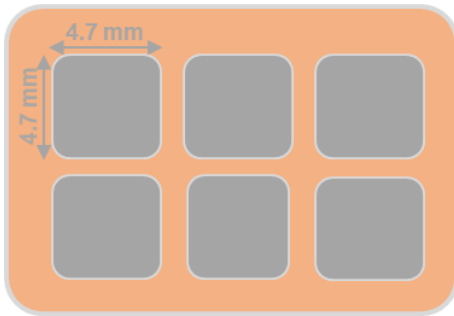


Figure 17: Experiment PIRL layer-by-layer II: ablation of skin cell layers of skin tissues different ages and different types. Six biological samples different ages (young to old) from breast and abdominal part of body skin were ablated twice.

3.3. Protein extraction using different extraction buffers

Selecting the suitable extraction buffer is a crucial step in sample preparation for high-throughput of proteins in LC-MS approaches. Detergents such as sodium dodecyl sulfate SDS are too harsh and incompatible for direct LC-MS analysis and therefore requires further purification steps. These detergent containing buffers as SDC and/or urea have been shown to possibly generate more precise and reproducible results although it is known that urea tends to induce unspecific modifications [55-58]. To achieve a wide range of protein classes, different tissue lysis buffers were used for protein extraction.

3.3.1. Urea-extraction protocol:

In most experiments in this study, 8 M urea buffer was used as TLB for denaturation of proteins. The tissue homogenate (in both conventional and in PIRL experiments) were resuspended in 500 μL 8 M urea and incubated for 1 h at $-4\text{ }^\circ\text{C}$. They were then sonicated at

25% power for 30 sec and centrifuged at 10.000 rcf. An aliquot of each sample was diluted to 2 M urea for colorimetric detection and relative quantitation of total protein using BCA protein assay as described in user guide [59]. With the absorption of dilution series of standard proteins, a linear regression calibration curve was generated which enabled the estimation of total protein range in each sample. Aliquots of lysates were transferred in a cut-off centrifuge filter (10 kDa) and were centrifuged at 14.000 rcf for 25 min. The denatured proteins were ready for the in-solution digestion with the FASP method for proteome analysis as described in chapter 3.5.1.

3.3.2. SDC-extraction protocol:

The second TLB used in this study was the SDC buffer. To the homogenate samples, 500 µL SDC buffer (1% w/v sodium deoxycholate in 100 mM triethylammonium bicarbonate (TEAB)) was added. Then the samples were sonicated at 25% power for 30 sec. The cells which were still intact were lysed, and proteins were denatured in the SDC buffer by incubating at 99 °C for 30 min. Afterward the samples were centrifuged at 10.000 rcf. An aliquot of each sample was taken for BCA protein assay. Although the SDC buffer was mentioned as compatible with the BCA assay in the user guide, the results of the test were negative and protein quantitation was not possible here. Aliquots of lysates were transferred in a cut-off centrifuge filter (10 kDa) and were centrifuged at 14.000 rcf for 25 min. Subsequently, the in-solution digestion was done as described in chapter 3.5.2.

3.3.3. SDC&Urea-extraction protocol:

Due to the results of SDC and urea extraction and digestion protocols in this study, for the skin samples collected on borosilicate filter paper a new protein denaturation protocol was established.

To the filter paper located in the tube, 500 µL SDC buffer was added. Then the samples were sonicated at 25% power for 30 sec and subsequently incubated at 99 °C for 30 min. They were centrifuged at 10.000 rcf and the supernatant was transferred into a cut-off filter (10 kDa). Then, 450 µL 8 M urea was added to the filter paper still in the tube and incubated for 20 min to increase the extraction efficiency. The protein solution was centrifuged again at 10.000 rcf. The supernatant containing urea-lysate was transferred into the same cut-off filter with the SDC-lysate. The protein mixture was concentrated to a 50 µL volume by centrifuging at 14.000 rcf for 25 min. Subsequently, the in-solution digestion was carried out as described in chapter 3.5.3.

3.4. In-solution tryptic digestion

The in-solution digestion in cut-off filter was based on the filter-aided sample preparation (FASP) method developed by WIŚNIEWSKI *et al.* which enabled a buffer exchange (in case of detergents like SDC, [60]) or buffer dilution (in case of 8 M urea) and got rid of biomolecules smaller than 10 kDa (e.g. nucleic acids).

3.4.1. Urea-digestion protocol:

The in-solution digestion of the lysate containing 8 M urea TLB was performed as follows. All steps were carried out in the cut-off filter. 6 M urea was added to the cut-off filter. The protein solution was concentrated to approx. 50 µL volume by centrifuging at 14.000 rcf for 25 min. This step was repeated twice. For protein reduction, 1.3 µL 100 mM DTT (dissolved in 100 mM AmbiCa, pH 8.3) was added to the lysate and the samples were incubated at 56 °C for 10 min. The cysteine residues were alkylated with 1.3 µL 300 mM IAA (dissolved in 100 mM AmbiCa, pH 8.3) by incubating at room temperature for 30 min in the dark. Proteins were digested with 0.5 µg trypsin for PIRL experiments and 2.5 µg for classical experiments in a ratio of 1:200 w/v (trypsin:protein ratio) in 100 mM AmbiCa at 37 °C for 16 h. After the digestion, the tryptic digested peptides were collected in a new tube by centrifuging at 14.000 rcf for 30 min. The samples were dried in a speed vacuum and stored at -20 °C until LC-MS/MS measurement.

3.4.2. SDC-digestion protocol:

The in-solution digestion of the lysate containing SDC TLB buffer was performed as follows. All steps were carried out in the cut-off filter. The lysate was centrifuged at 14.000 rcf for 25 min to a volume of approx. 50 µL. For protein reduction 1.0 µL 1 M DTT (dissolved in SDC buffer) was added to the lysate and the samples were incubated at 60 °C for 30 min. The cysteine residues were alkylated with 1.0 µL 1 M IAA (dissolved in SDC buffer) by incubation at room temperature for 30 min in the dark. Proteins were digested with 0.5 µg trypsin for PIRL experiments and 2.5 µg for classical experiments in a ratio of 1:200 w/v (trypsin:protein ratio) at 37 °C for 18 h. After the digestion, the tryptic peptides were collected in a new tube by centrifuging at 14.000 rcf for 30 min. To get rid of the SDC buffer, 1% FA was added and SDC precipitated. The samples were centrifuged at 10.000 rcf for 5 min. Afterward, the supernatant was collected in a new tube. The samples were dried in a speed vacuum. A desalting step was needed after using SDC buffer. Therefore, the tryptic-digested peptides were desalted on a hydrophobic stationary phase based on reversed-phase chromatography. The peptides were resuspended in 1 mL washing buffer (5% MeOH (v/v), 0.2% FA in HPLC-grade H₂O (v/v)).

They were loaded on a strongly hydrophobic Oasis HLB extraction cartridges with C18-material. Salts and hydrophilic molecules were washed out with 3 mL washing buffer. Then the elution of peptides from the columns followed with 1.5 mL elution buffer (50% MeOH). The buffer was removed using speed vacuum and the dried peptides were stored at -20 °C until LC-MS/MS measurement.

3.4.3. SDC&Urea-digestion protocol or WIŚNIEWSKI et al.:

The extraction described in 3.4.3 was followed by a buffer exchange [60]. For this, 450 µL 6 M urea was added to the cut-off filter and was centrifuged at 14.000 rcf for 25 min. This step was repeated four times more for absolute removal of the SDC buffer. Finally, the proteins were digested with the urea protocol as described above in chapter 3.4.1. A desalting step was no longer necessary as the SDC buffer was completely removed.

3.5. LC-MS/MS analysis

For mass spectrometric measurement, the PIRL samples were resuspended in 20 µL 0.1 % FA (in HPLC-grade H₂O) and the classical samples in 50 µL.

LC-MS/MS analysis was performed by electrospray-ionization (ESI) using a quadrupole (Q) orbitrap (OT) ion trap (IT) mass spectrometer (Orbitrap Fusion™ Tribrid™, Thermo Scientific, Germany) or a quadrupole orbitrap mass spectrometer (Orbitrap QExactive™, Thermo Scientific, Germany). The mass spectrometers were coupled online to an UltiMate 3000 Rapid Separation liquid chromatography (RSLC) system (Dionex, Thermo Scientific, Germany).

The samples were loaded with a flowrate of 3 µL/min on a trapping column (Acclaim PepMap µ-precolumn, C18, 300 µm × 5 mm, 5 µm, 100 Å, Thermo Scientific; in buffer A (0.1% FA in HPLC-H₂O) buffer B: 0.1% FA in ACN) with 2% buffer B. The trapping column was washed firstly for 5 min with 2% buffer B (5 µL/min) and subsequently the peptides were eluted (200 nL/min) onto the separation reversed phase C18 column (Acclaim PepMap 100, 75 µm × 250 mm, 2 µm, 100 Å; Thermo Scientific; at a flowrate 300 nL/µm with a binary buffer system of solvent A (0.1% FA in HPLC-H₂O) and solvent B (0.1% FA in ACN with 3% solvent B in short gradient (2% solvent B in long gradient)). The peptides were eluted with a gradient of 3 – 30% buffer B in 35 min in 70 min gradients, respectively 2 – 80% buffer B in 115 min in 170 min gradients.

A fused silica emitter (inner diameter: 10 μm , New Objective, USA) was used to generate the electrospray with a spray voltage of 1700 V. Mass spectrometry analysis was programmed to acquire in data-dependent mode (DDA) in positive ion mode.

Fusion (Q-OT-IT) MS-method: the full scan was acquired in the orbitrap (OT) mass analyzer with resolution of 120,000 FWHM (full width at half maximum) at 200 m/z on MS level over a m/z range from 400 to 1300, a maximum injection time of 50 ms and an AGC target value of 2×10^5 . The fragmentation was carried out with a HCD collision energy of 30% and an intensity threshold of 1×10^5 and an isolation width 2.0 m/z. Only precursors with charge states between +2 and +5 and the most intense precursors were selected for fragmentation. The fragment spectra were recorded in ion trap (IT) as detector with a rapid scan rate mode and resolution 120,000 and the ions were isolated to an AGC target value of 1×10^4 with a maximum injection time of 200 ms and isolation window 1.6 m/z. Every second a precursor spectrum was recorded.

QExactive (Q-OT) MS-method: The full scan was acquired in the orbitrap (OT) mass analyzer with resolution of 70,000 FWHM at 200 m/z on MS level over a m/z range from 375 to 1500 (maximum injection time: 60 ms and AGC target: 3×10^6). The fragmentation was carried out with a HCD collision energy of 27% and an intensity threshold of 3×10^4 and an isolation window 4.0 m/z. Only precursors with charge states +2 and higher and the most intense precursors were selected for fragmentation. The fragment spectra were detected in Top10 mode with a maximum injection time of 50 ms and a resolution of 17,500 FWHM at 100 m/z. The top intense ions were isolated to a target value of 1×10^5 . Every second a precursor spectrum was recorded.

3.6. Data analysis

The raw data were processed with Proteome Discoverer, v1.4.1.14 (Thermo Scientific) using the following parameters: FDR < 0.01 at the level of proteins, peptides and modifications; precursor mass tolerance 10 ppm and fragment mass tolerance 0.02 Da for QExactive data and 0.2 Da for Fusion data. Enzyme specificity was set to trypsin, and the search included as dynamic modifications: N-acetylation of protein, deamidation of asparagine, glutamine and oxidation of methionine and as a fixed modification: cysteine carbamidomethylation. Up to 2 missed cleavages were allowed for protease digestion. Searches were performed against the human database from UNIPROT FASTA database (June 2017). The lists of identified proteins were filtered within the proteins with equal or more than one unique peptide were considered.

3.7. Cryosections with cyrocut, H&E staining and microscopy

For a histological imaging of the samples after PIRL-DIVE ablation, H&E staining and subsequently microscopy steps were followed. Frozen tissue blocks (after PIRL-DIVE ablation) were placed into plastic embedding molds, surrounded by OCT embedding media and then were frozen for half an hour. Afterward, the samples were taken out of the molds and fixed on an adapter in the cryomicrotome. The tissues were cut in 6-8 μm slices. The tissue microsections were mounted on glass microscope slides.

For the H&E staining, the microsections on slides were washed under running distilled water. The sections were immersed in hematoxylin solution and incubated for 1 min. Then the sections were washed under running distilled water for 10 min until a blue-violet color appeared. Following, the sections were immersed in acidified eosin solution (with acetic acid) and incubated for 1 min. Thereafter they were washed again under running distilled water until a red-pink color appeared. For dehydration, the microsections were immersed in EtOH solution. Subsequently, the slides were covered with mounting media and fixed with coverslips.

Finally, the H&E-stained samples were ready for microscopy. A light microscope (BZ-9000 Fluorescence Microscope, BIOREVO) was used here.

For depth determination of PIRL-ablated tissues, the tissues were stored in biopsy capsules in 4% PFA and were sent for imaging with confocal laser scanning microscope. The ablation depths were determined by using either fluorescent dye (Hoechst 33342 staining – representing the nuclei of the cells) or collagen autofluorescence. The ablation depths were measured in the NIS Elements AR image precession software using the 'EDF-z-profile' function.

3.8. Materials

3.8.1. Chemicals and (bio-) materials

Table 1: List of chemicals and biomaterials.

chemicals and materials	supplier (location)
Acetonitrile (LiChrosolv®)	Merck® (Darmstadt, Germany)
Acidic acid	Roth (Karlsruhe, Germany)
Ammonium bicarbonate	Merck® (Darmstadt, Germany)
BCA test kit	Thermo Fisher Scientific (Pinneberg, Germany)
CV Ultra Mounting Media	Leica (Wetzlar, Germany)
Dulbecco's phosphate buffered saline without Ca & Mg, (DBPS, c = 0,095 M PO ₄)	Lonza (Verviers, Belgium)
Dispase II (neutral protease, grade II)	Sigma-Aldrich (Steinheim, Germany)
Dithiothreitol	Sigma-Aldrich (Steinheim, Germany)
Eosin	O. Kindler & ORSAtec (Bobingen, Germany)
Formic acid	Merck® (Darmstadt, Germany)
Hematoxylin	O. Kindler & ORSAtec (Bobingen, Germany)
Iodoacetamide	Sigma-Aldrich (Steinheim, Germany)
Methanol (LiChrosolv®)	Merck® (Darmstadt, Germany)
Polyethylene glycol	Sigma-Aldrich (Steinheim, Germany)
Sodium Deoxycholate	Sigma-Aldrich (Steinheim, Germany)
Sodium dodecyl sulfate	Fluka (Munich, Germany)
Tissue-Tek O.C.T Compound and Cryomolds	Sakura (Staufen, Germany)
Triethylammonium bicarbonate	Thermo Scientific
Trypsin	Promega (Mannheim, Germany)
Trypsin resuspension buffer	Promega (Mannheim, Germany)
Urea	Merck® (Darmstadt, Germany)

Water (LiChrosolv®)	Merck (Darmstadt, Germany)
---------------------	----------------------------

Table 2: List of materials.

materials	supplier (location)
1.5 mL or 2.0 mL Tubes	Eppendorf AG (Hamburg, Germany)
Borosilicate filter paper without binder, PF GF 50, 56 g/qm, 0.29 mm thickness	Hahnemühle Fineart (Dassel, Germany)
Amicon Ultra-0.5 mL Centrifugal Filters (10kDa)	Merck® (Darmstadt, Germany)
Microscope glass slide, SuperFrost® Ultra Plus	O. Kindler & ORSAtec (Bobingen, Germany)
New Objective SilicaTip™ Emitter	New Objective (Woburn, USA)
Oasis HLB Extraction cartridge	Waters, (Massachusetts, USA)
Pipette tips	Eppendorf AG (Hamburg, Germany)

Table 3: List of the chromatography column.

instrument	supplier (location)
Acclaim PepMap 100	Thermo Scientific (Bremen, Germany)
Acclaim PepMap μ -precolumn	Thermo Scientific (Bremen, Germany)

3.8.2. Equipment

Table 4: List of equipment.

instrument	supplier (location)
BZ-9000 Fluorescence Microscope, BIOREVO	KEYENCE (Neu-Isenburg, Germany)
Cryocut CM3050 S Cryostat	Leica (Wetzlar, Germany)
Dionex UltiMate 3000 RSLCnano	Thermo Scientific (Bremen, Germany)
Orbitrap Fusion™ Tribrid™ mass spectrometer	Thermo Fisher Scientific (Dreieich, Germany)

OPA (optical parametric amplifier), OPA-3000	Attodyne (Toronto, Canada)
Pico second-Infrared-Laser (PIRL-HP2-1064	Attodyne (Toronto, Canada)
Q Exactive™ Hybrid-Quadrupol-Orbitrap™ mass spectrometer	Thermo Fisher Scientific (Dreieich, Germany)
Sonicator HD2200	Bendelin (Berlin, Germany)
Spark 10M	Tecan (Crailsheim, Germany)
SpeedVac concentrator 5301	Eppendorf AG (Hamburg, Germany)
Table centrifuge 5424	Eppendorf AG (Hamburg, Germany)
Thermomixer 5320	Eppendorf AG (Hamburg, Germany)
TissueLyser II	QIAGEN (Hilden, Germany)
Tecan GENios	Tecan (Crailsheim, Germany)
Vacuum pump CVC 2000	Vacuubrand (Wertheim, Germany)
VARIO® chemistry diaphragm pump MZ 2C Vario	VACUUBRAND (Wertheim, Germany)

3.8.3. Softwares

Table 5: List of software.

software	supplier (location)
AutoCad	Autodesk GmbH (Munich, Germany)
Mircosoft® Office Word	Microsoft Corporation (Redmond, USA)
Mircosoft® Office Excel	Microsoft Corporation (Redmond, USA)
Mircosoft® Office Powerpoint	Microsoft Corporation (Redmond, USA)
Proteome Discoverer 2.0	Thermo Fisher Scientific (Bremen, Germany)
Thermo Xcalibur™ 4.0.27.13	Thermo Fisher Scientific (Bremen, Germany)

4 Results and discussion

4.1. Results of homogenized of dispase-separated skin tissues

The efficiency of the PIRL-DIVE homogenization method for skin proteomics was reviewed by comparing it to conventional mechanical homogenization methods. Therefore, in the first part of this study, dispase-separated skin tissues (dermis and epidermis) were homogenized using PIRL-DIVE and mechanical methods. The protein yields and distribution of different extracted protein classes, as well as their corresponding reproducibility in biological and technical replicates were consulted for an evaluation. Additionally, the choice of an appropriate TLB was ascertained based on protein yields and their reproducibility.

The quality check of all three homogenization methods was performed mostly for dermal tissues, due to availability in abundance and better handling. Nevertheless, epidermal tissues could be homogenized by TissueLyser (TL) and PIRL-DIVE, but not by grinder & LN₂. In the following sections, the results of protein identification for three homogenization methods as well as the comparison between the methods, using different TLBs are presented.

All samples in the following chapters were analyzed using the bottom-up mass spectrometry approach. The samples were proteolytically digested after homogenization and protein extraction/denaturation steps. The tryptic peptide mixtures were then analyzed via tandem mass spectrometry. The raw data were eventually processed with different proteomics and statistical tools.

Exemplary in figure 18, the mass spectrometry data and its analysis are visualized for an epidermal tissue ablated with PIRL. Figure 18 shows a base peak chromatogram, a spectrum on the MS level 1 with the isotope pattern for a peptide with 738 m/z, the extracted ion chromatogram of the same peptide and a fragment spectrum on the MS level 2. The selected peptide with the sequence FLEQQNQVLQTK belongs to the protein group keratin, type II cytoskeletal 1.

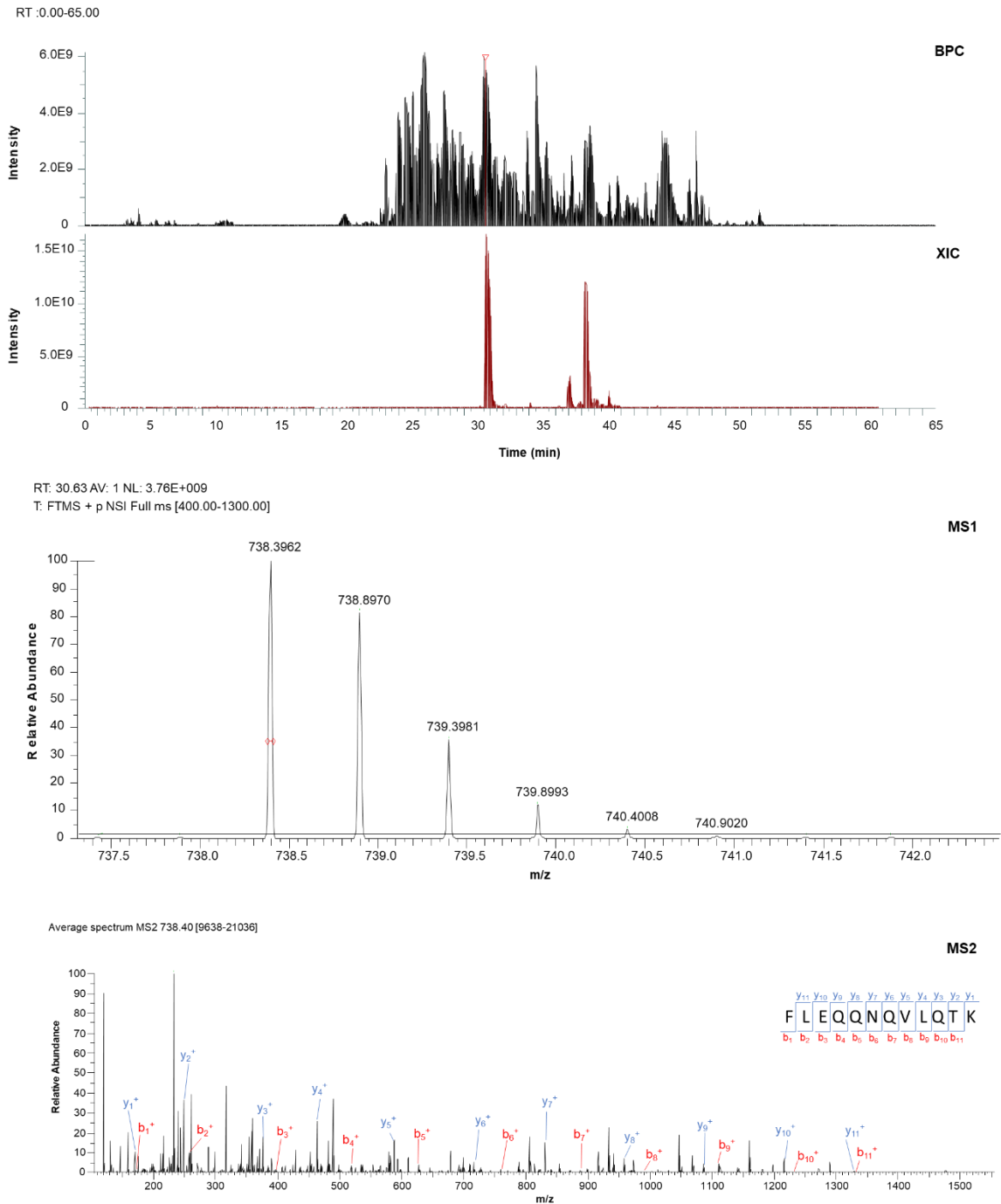


Figure 18: Explanation of mass spectrometric data by this example for a tryptic peptide of the protein group keratin, type II cytoskeletal 1, in an epidermal sample ablated with PIRL. BPC: base peak chromatogram, XIC: extracted ion chromatogram of the monoisotopic peak 738 m/z, MS1: MS-spectrum on the level 1 of the precursor ion with its isotope pattern, MS2: Fragment spectrum of the peptide sequence FLEQQNQVLQTK.

4.1.1. Results of homogenized dispase-separated skin tissues by TissueLyser

The dermis and epidermis tissues were homogenized by TL and extracted with two different TLBs: 8M urea and SDC buffer. The results of extracted proteins with SDC buffer are mentioned in chapter 4.1.4. In figure 19, the protein yields of five biological replicates for dermis and epidermis tissues are diagrammed. The samples came from donors of different age groups (breast and abdominal tissues from 38, 42, 48, 51 and 54 years old female donors).

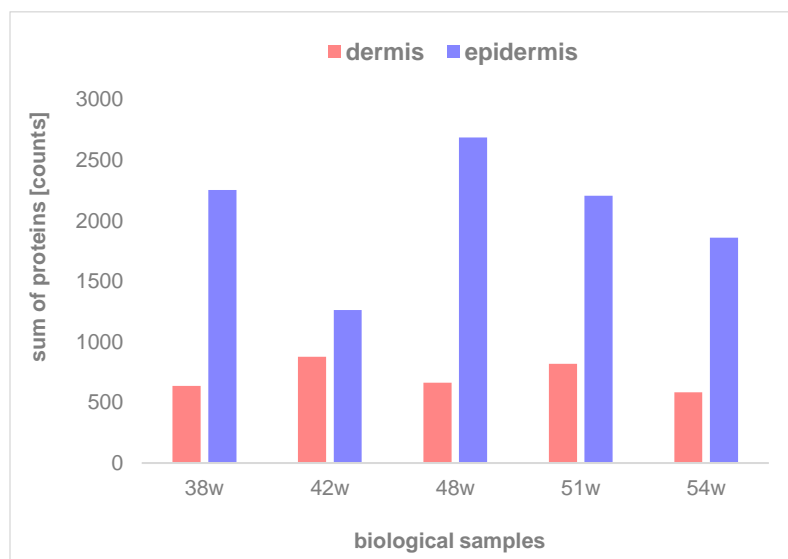


Figure 19: Comparison of protein yields of two different type of skin tissues (dermal and epidermal tissues) homogenized by TissueLyser (TL) with five biological replicates from abdominal and breast area of skin tissue of donors different ages. Sum of achieved protein numbers in biological samples: 38w, 42w, 48w, 51w and 54w).

The number of identified epidermis proteins ranged from 1000 to a maximum of 2690 proteins while the number of identified proteins in dermis tissues was between ca. 400 and 960 proteins (unique peptides ≥ 1). Thus, the numbers of identified epidermal proteins was roughly 2.5-fold of dermal proteins. It stands to reason that the dermis tissue is composed largely of extracellular matrix (ECM) components such as collagen, fibrin and elastin fibers. Due to the ECM structure and highly crosslinked fibers of dermal tissue, the homogenization of dermal tissue is more difficult, and the protein identification suffers accordingly. Furthermore, the low identification number of dermal proteins is because of high abundant proteins like ECM proteins as collagen alpha-1 and also proteins as AHNAK, serum albumin, and myosin. A high concentration of such high abundant proteins leads to signal suppression of lower abundant proteins during mass spectrometry measurements on MS-level 1 (MS1) which in turn results to less fragmentation on MS-level 2 (MS2). In general, the protein identification depends on several factors from the sample homogenization step to the mass spectrometry analysis.

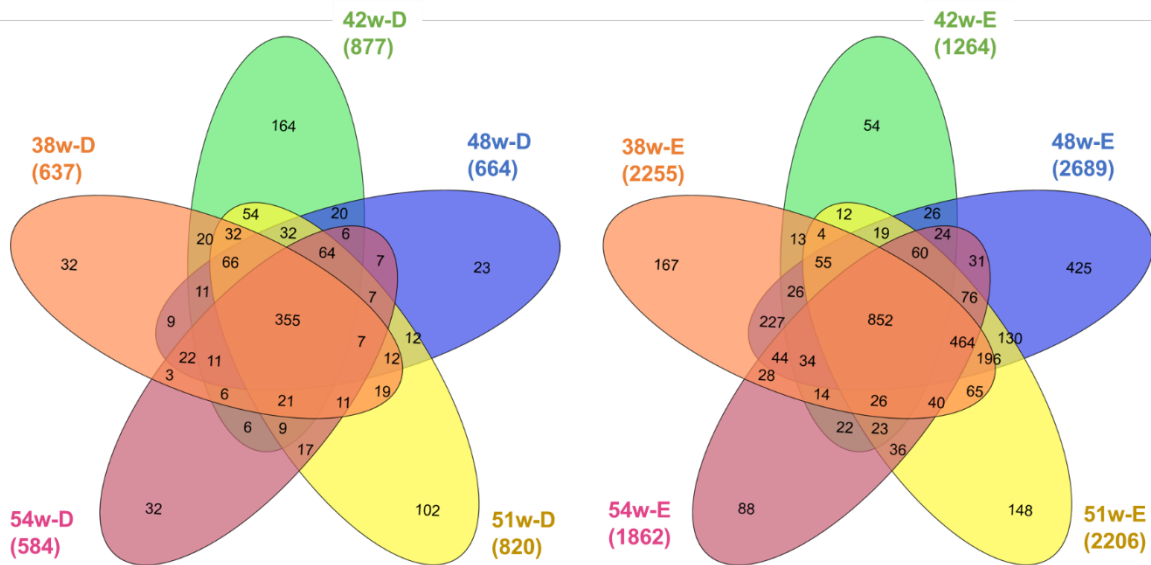


Figure 20: Venn diagram of five biological replicates homogenized by TissueLyser (TL) and extracted with 8 M urea. *Left:* the distribution of the identified protein in all replicates of dermal tissues (the reproducibility rate in all replicates $reprod_{rate} = 24.8\%$ and at least in four of five replicates $reprod_{rate} = 44.0\%$). *Right:* the distribution of the identified protein in all replicates of epidermal tissues (the reproducibility rate in all replicates $reprod_{rate} = 29.8\%$ and at least in four of five replicates $reprod_{rate} = 43.5\%$) [61].

The Venn diagrams of all five biological replicates with the total number of identified proteins for each sample are displayed for dermal and epidermal tissues in figure 20. In total, 1192 different proteins were identified across all dermis samples whereas the mean value of identified proteins in all five replicates was about 716 proteins. 355 of those 1192 proteins were identified in all replicates. This makes a reproducibility rate ($reprod_{rate}$) of 29.8%. This reproducibility rate varied to 44.0%, while 524 different identified proteins were regarded as present in at least in four of five replicates. Proteins, identified in all biological samples in epidermal tissues, were 852, while the sum of identified proteins across all epidermal replicates was 3429 (mean value = 2055 proteins), and thus the $reprod_{rate}$ was 24.8%. Considering proteins identified in four of five biological replicates, it resulted in a $reprod_{rate}$ of 43.5% (1491 proteins identified in at least 4 samples).

The number of outlier proteins, which were identified in just one sample, was proportional to the total number of identified proteins in the corresponding sample. For example, in the epidermis sample 48w-E, 2689 proteins were identified in total. Of these, 425 proteins occurred exclusively in this sample, and in sample 42w-E, there were a total of 1264 proteins with 48 proteins exclusively in this sample. Hence, the higher the total number of proteins the higher the number of proteins exclusively identified in the sample.

The protein recovery in both tissue types was low. This says about the efficiency of the TL technique as homogenization method. Further details are explained in chapter 4.1.3.

4.1.2. Results of homogenized dispase-separated skin tissues by grinder & LN₂

The dermal tissues were homogenized with a grinder & LN₂ and extracted with two different TLBs: 8M urea and SDC buffer. The results of extracted proteins with SDC buffer as described above are mentioned in chapter 4.1.4. Due to the difficulties in handling small sizes of epidermal tissues, their homogenization could not be carried out by G&LN₂. Three technical replicates of each biological sample were homogenized with G&LN₂ to powder, tryptic digested and measured by tandem mass spectrometry. In table 6, the outcomes of protein numbers are listed for all technical replicates of each biological dermal tissue. In sample 54w, 733 different proteins were identified (430 proteins on average in all technical replicates) whilst the *reprod_{rate}* is about 29.3% in all replicates and 46.3% in two of three. In sample 58w in total. 793 different proteins and averagely 468 proteins were identified with a *reprod_{rate}* of 25.9% in all replicates and 51.3% in two of three. In the last biological sample 66w, 877 proteins were identified with 528 proteins on average in all three technical replicates. The *reprod_{rate}* was about 32.2% in all and 48.6% in two of the three replicates. In figure 21 the mean value of identified protein numbers and the variation within the respective dermal tissue for its three technical replicates are shown. Altogether three biological samples (54w, 58w, 66w) and respective three technical samples were used (n=9).

Table 6: Comparison of reproducibility of dermis samples homogenized by grinder & LN₂ and extracted with urea. Achieved protein IDs for three biological samples (54w, 58w, 66w) and their protein number for three technical replicates per tissue; mean value of protein numbers in all three technical replicates. Reproducibility rate (*reprod_{rate}*) in all technical replicates or in two of three replicates in percentage.

biological replicates	54w			58w			66w		
technical replicates	1	2	3	1	2	3	1	2	3
protein IDs	291	354	645	377	488	540	396	450	739
mean	430			468			528		
reprod.-rate in all tech. replic.	29.3%			25.9%			32.2%		
reprod.-rate in 2 of 3 replic.	46.3%			51.3%			48.6%		

The number of identified tryptic peptides varied between the technical and biological samples enormously. This variation shows that the G&LN₂ method restricts its applicability. For dainty soft tissues like epidermal tissues, the method is ineligible but even so for though, rubbery tissues as dermal tissues proved unsuitable. Besides, it is also associated with great sample loss during milling when exercising force by moving the pestle in the mortar. Incidentally, the hazard of contamination from the environment is increased as the system stands open.

Among the biggest disadvantages of this technique is the handling of samples, placing and removing from the mill, uncontrolled loss of samples during milling and the higher contamination risk.

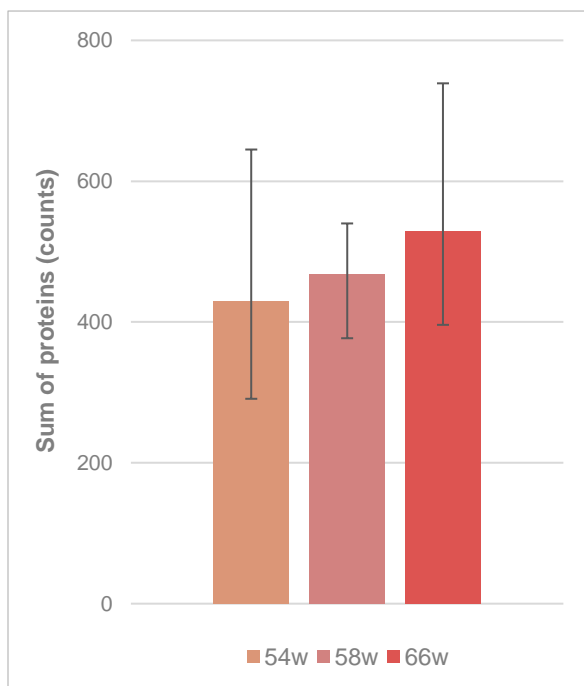


Figure 21: Statistical analysis of the LC-MS/MS data from three biological replicates of dermal tissues homogenized by grinder & LN₂ and extracted with urea. The mean and corresponded variation of achieved protein yields (unique peptides ≥ 1) within the respective biological sample is displayed. (biological samples: 54w, 58w and 66w; technical replicates $n=3$ per biological sample).

4.1.3. Comparison of both conventional, mechanical homogenization methods: TissueLyser (TL) and grinder & LN₂

These experiments were performed on dispase separated dermal tissue from the same biological donors which were divided in small pieces. In all, three biological samples were used, and three technical replicates were obtained for each. The dermis samples were homogenized as described above (chapter 3.2.1) and extracted with 8 M urea. The assessment of both homogenization method is depicted in figure 22. The comparison is executed based on the average value of protein numbers identified in technical replicates for each biological sample (figure 22A). Additionally, the number of protein groups (figure 22B) and the total number of PSMs (the number of peptide-spectrum matches, figure 22C) were compared. The standard

deviation within the technical replicates are also displayed additively. Here too, proteins with unique peptides greater than or equal to one were consulted for interpretation of data.

Samples that which were homogenized with TL and extracted with urea, averaged 530 identified proteins in all three biological samples (for 54w, 58w and 66w). For each biological sample three technical replicates were prepared and analyzed whereby 521, 512 and 556 proteins per biological origin (54w, 58w and 66w) were counted (listed in table 7). In the case of homogenization via G&LN₂ and urea extraction, the same biological samples resulted in 430, 468 and 528 protein numbers (explained in table 6, in chapter 4.1.2).

Table. 7: Comparison of reproducibility of dermis samples homogenized by TissueLyser extracted with urea. Achieved protein IDs for three biological samples (54w, 58w, 66w) and their protein number for three technical replicates per tissue; mean value of protein numbers in all three technical replicates. Reproducibility rate ($reprod_{rate}$) in all technical replicates or in two of three replicates in percentage.

biological replicates	54w			58w			66w		
technical replicates	1	2	3	1	2	3	1	2	3
protein IDs	303	677	584	457	438	640	647	454	568
mean	521			512			556		
reprod.-rate in all tech. replic.	24.9%			38.4%			46.0%		
reprod.-rate in 2 of 3 replic.	50.9%			57.5%			64.8%		

The results (shown in figure 22) indicate that the number of identified proteins in both mechanical homogenization techniques was in the same range and thus the standard deviation showed same analogy on protein as well as protein group levels. The only difference was observed at PSM level for one sample (58w) but it did not affect the protein yields as much as expected. The number of peptide spectra matched for the identified proteins (PSM) includes those that have been identified repeatedly, thus it can be higher than the number of peptides identified for proteins. This value depends on the protein size and the protein abundance. This implies the PSM scoring ensures a semiquantitative measurement of protein abundance but not the quality of identification on protein level. Furthermore, the low number of identified proteins in dermal tissues for both classical techniques were expected as described above (in

chapter 4.1.1). Higher abundant proteins suppress the signals of the low abundant proteins thus altering the quality of proteome analysis. Nevertheless, the protein yields in TL (urea) were tangentially higher than in G&LN₂ (urea).

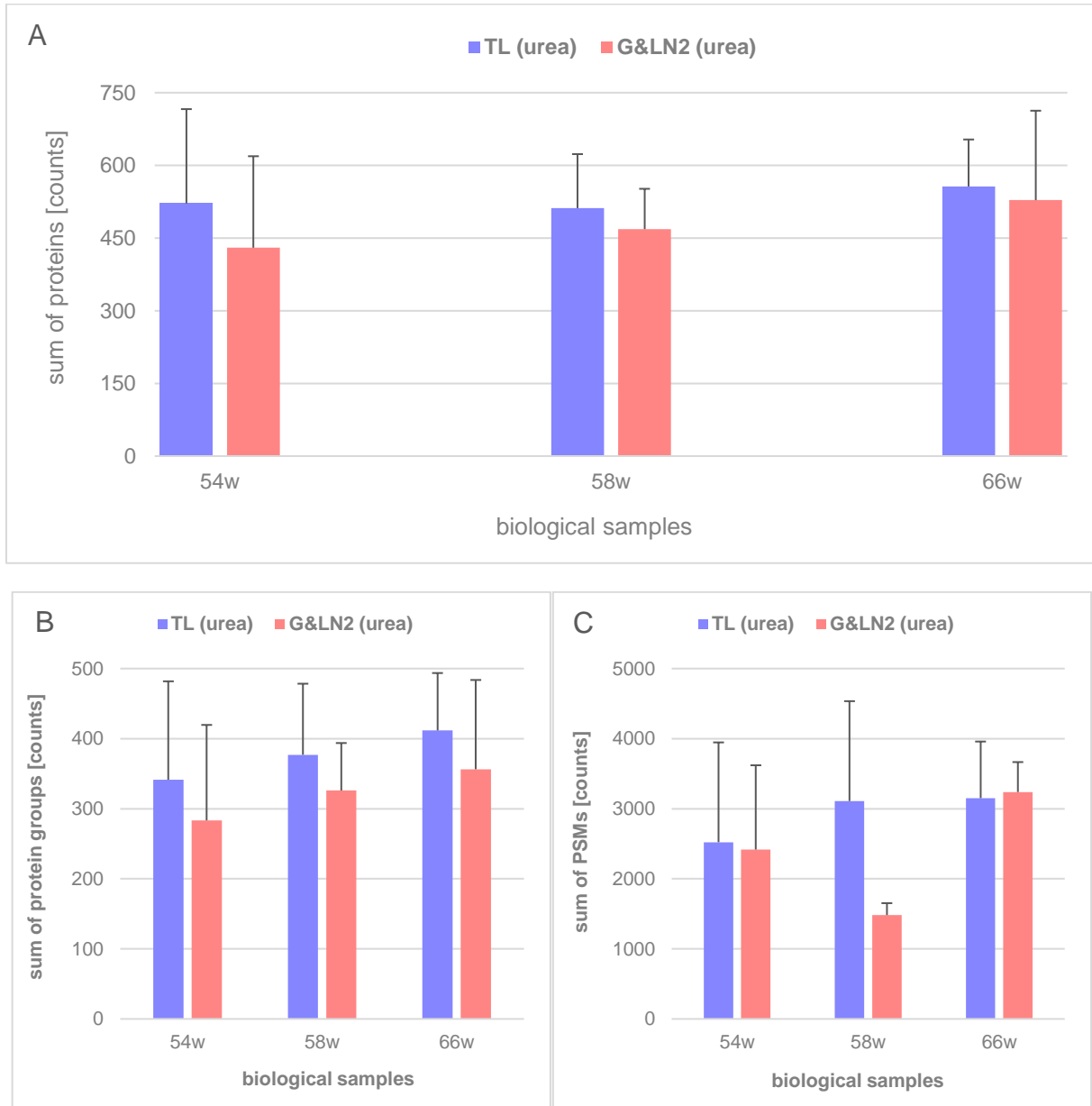


Figure 22: Statistical analysis of the LC-MS/MS data from tryptic digested peptides of dermis tissues homogenized with two different classical methods: TissueLyser (TL) and grinder & LN₂ (G&LN₂) using urea buffer. The mean and corresponded standard deviation of achieved protein (bar chart A), protein group (bar chart B) and PSM (bar chart C) yields are shown for three biological samples (n=3: 54w, 58w and 66w) with three technical replicates pro each biological sample.

Taking into the account the reproducibility of results for respective biological samples of both techniques, TL (urea) performs better than G&LN₂ (urea) in terms of proteins recovery. In figure 23, the Venn diagram of identified proteins in all biological replicates of TL (urea) demonstrates an overlap of 494 proteins and a $\text{reprod}_{\text{rate}}$ of 40.0% in all replicates (sum of all proteins identified in total = 1235). This list of overlapped proteins was uploaded to the PANTHER database [63] to classify the proteins based on their cellular component (CC). This cellular component analysis was performed over algorithms to describe the protein location at subcellular level. The distribution of the sub-cellular classification is illustrated in figure 23 with the percentage of hits to each of gene ontology (GO) annotation term. About 36% of the proteins belonged to cell parts (GO:0044464) and 26% to the organelle part (GO:0043226). The rest are organized in descending order: macromolecular complex (15%, GO:0032991), membrane (12%, GO:0016020), extracellular region (7%, GO:0005576), extracellular matrix (2%, GO:0031012), cell junction (1%, GO:0030054), synapse, (1%, GO:0045202).

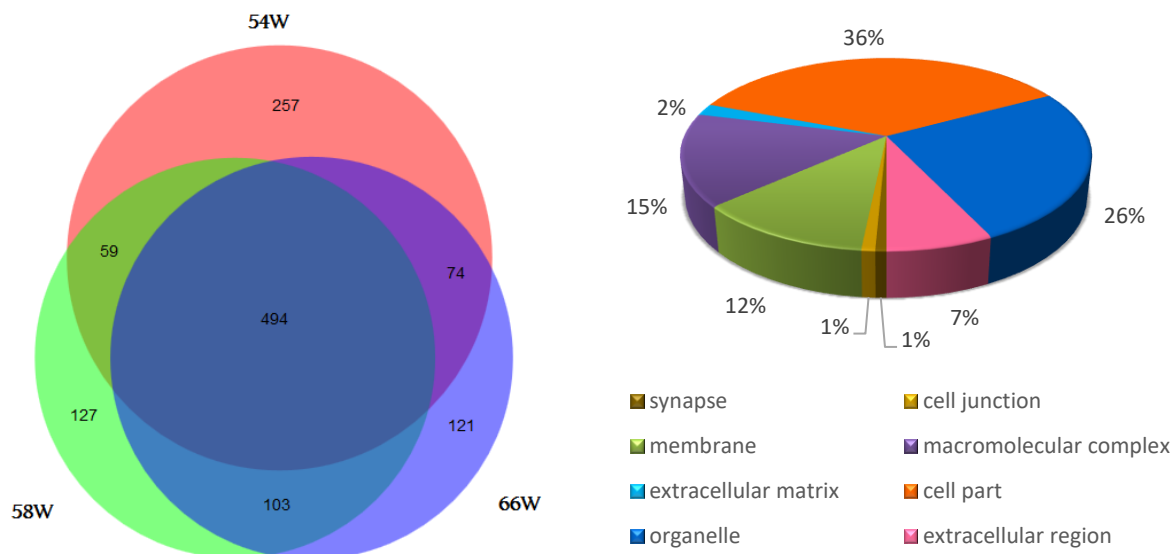


Figure 23: Statistical analysis of the LC-MS/MS data from tryptic digested peptides of dermis tissues homogenized by TissueLyser (TL) using urea buffer as TLB. Left: Venn diagram of biological replicates (54w, 58w, 66w) [62]. **Right:** pie chart diagram of GO (Gene Ontology) Cellular Component (CC)-classification of proteins identified in all biological and technical replicates [63].

The same analysis was performed for samples homogenized with G&LN₂ (urea). In figure 24, the Venn diagram the proteins identified in all biological replicates demonstrates an overlap of 421 proteins and a $\text{reprod}_{\text{rate}}$ of 33.1% in all replicates (sum of all proteins identified in total = 1273). As described above, the list of overlapped proteins was uploaded to the PANTHER database and the distribution of protein classification due to their cellular component ontology

was investigated. The distribution of extracted proteins by G&LN₂ (urea) hardly differs from the TL (urea) method. About 34% of the proteins were extracted from cell parts (GO:0044464) and 23% from the organelle part (GO:0043226). The rest belonged to the categories in descending order: macromolecular complex (17%, GO:0032991), membrane (13%, GO:0016020), extracellular region (9%, GO:0005576), extracellular matrix (2%, GO:0031012), cell junction (1%, GO:0030054), synapse, (1%, GO:0045202).

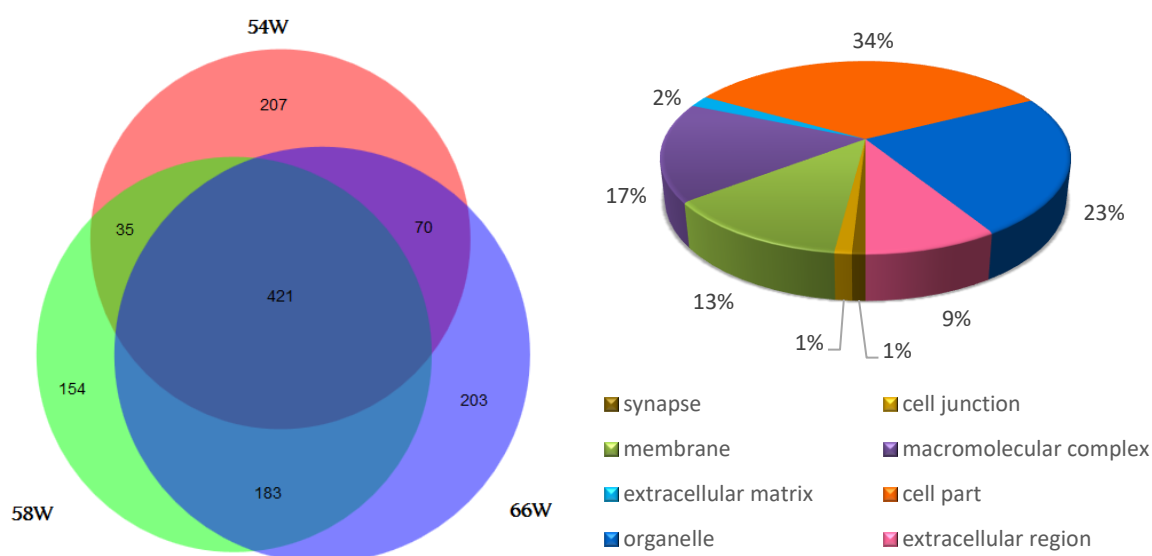


Figure 24: Statistical analysis of the LC-MS/MS data from tryptic digested peptides of dermis tissues homogenized by grinder & LN₂ (G&LN₂) using urea buffer as TLB. *Left:* Venn diagram of three biological replicates (54w, 58w, 66w) [62]. *Right:* pie chart diagram of GO (Gene Ontology) CC-classification of proteins identified in all biological and technical replicates [63].

4.1.4. Comparison between different extraction buffers for both mechanical homogenization methods

Another crucial point in sample preparation of tissues for LC-MS approaches is the choice of suitable extraction buffer to achieve a high-throughput of proteins. Inferring literature, detergent-containing buffers can provide more accurate and reproducible results, but a further step to remove detergents must be incorporated due to their incompatibility with mass spectrometry. It has also been known that urea tends to induce unspecific modifications on some proteins [55-58]. Therefore, the efficiency of a detergent buffer was tested as TLB and the results were compared with those generated from 8 M urea, which were already explained

in this study. Next, the SDC as TLB was assessed for both mechanical homogenization methods: TissueLyser and grinder & LN₂.

The mean values of identified proteins for five technical replicates of dermal tissues are diagrammed for both homogenization methods TL (SDC) and G&LN₂ (SDC) in figure 25. The identified protein number for TL (SDC) resulted in an average value of 146 proteins and of 75 protein groups. For G&LN₂ (SDC) the average value with 156 proteins and 77 protein groups were slightly higher than the TL (SDC). In the figure, the error bars demonstrate the reducibility quality for all five technical replicates. The deviation is quite high in terms of low yields.

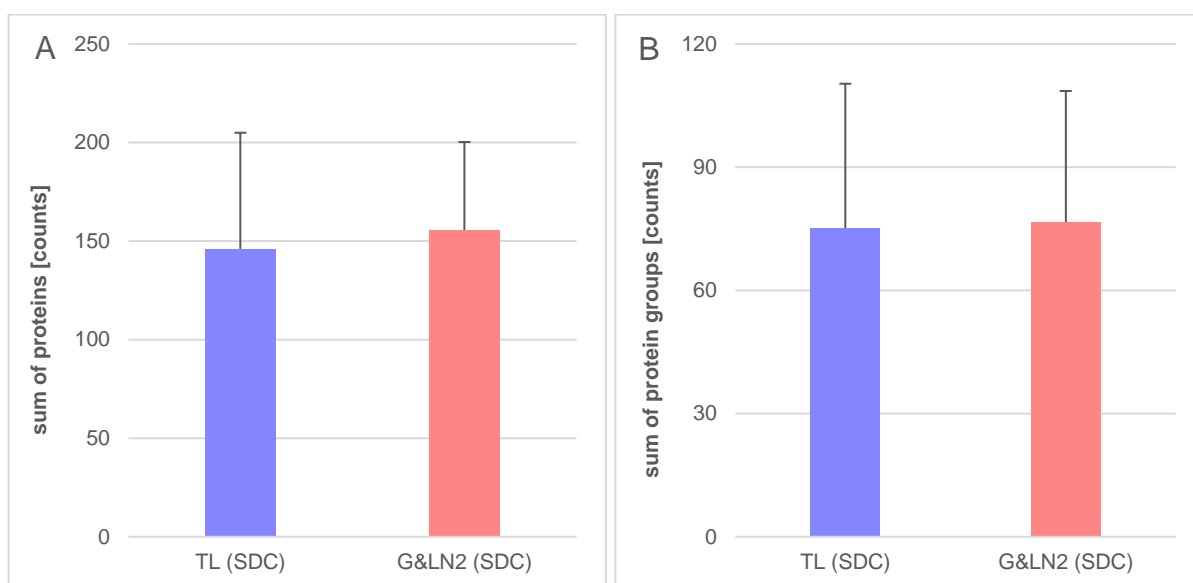


Figure 25: Statistical analysis of the LC-MS/MS data from tryptic digested peptides of dermis tissues homogenized with two different conventional, mechanical methods: TissueLyser (TL) and grinder & LN₂ (G&LN₂) SDC buffer as TLB. The mean and corresponded standard deviation of achieved protein (A) and protein groups (B) yields are shown for one biological sample (five technical replicates).

Comparing SDC and urea as TLBs, the highest number of identified proteins was observed using the urea protocol for both TL and G&LN₂ homogenization methods. Also, the reproducibility rate was cut off better than the SDC protocol. Both extraction buffers for both mechanical homogenization methods were compared based on their protein yields. In figure 26, a bar diagram shows the total number of identified proteins without the repeated proteins in all replicates for each experiment: TL (urea), TL (SDC), G&LN₂ (urea) and G&LN₂ (SDC). The two homogenization experiments with urea show comparable numbers of proteins (1235 proteins for TL (urea) and 1273 proteins for G&LN₂ (urea)). This comparable protein ratio was

observed also for SDC experiments but in the low range. In experiment TL (SDC) 321 proteins were identified in total and in G&LN₂ (SDC) 328 proteins.

The Venn diagram in figure 26 shows the protein distribution for all four experiments. There was an overlap of 216 protein IDs found in all four experiments. The overlapping number of proteins identified in both homogenization methods (TL (urea) and G&LN₂ (urea)) was 565 proteins which were enriched by using the “Database for Annotation, Visualization and Integrated Discovery” (DAVID): a functional annotation bioinformatics microarray analysis tool [65]. For the enrichment analysis, the list of all proteins identified across all four methods was uploaded to DAVID and this served as a background library. The list of overlapping proteins, identified in both TL (urea) and G&LN₂(urea) were uploaded to DAVID [65] and the enrichment analysis was performed with the following enrichment preconditions: classification stringency: high, enrichment score greater than two (the higher the more enriched) and p-value less than 5.0×10^{-4} (the smaller, the more enriched). The enrichment analysis for 565 proteins clustered them in one significant functional annotation group:

- Subunit of G proteins (enrichment score: 4.1; p-value: 4.0×10^{-5}) including 11 proteins

The G proteins alpha subunits are membrane-associated, heterotrimeric proteins that contain the guanine nucleotide binding site. The G proteins and their receptors, which catalyze the GDP/GTP exchange and activate the G proteins, are the key factor in regulating and signaling systems in mammalian cells [91]. Further, 335 proteins were outstanding due to their CC GO-term: extracellular exosomes.

In contrast to the high overlap value in samples extracted with urea, SDC TLB exhibits just one protein (ERC2, a plasma protein as regulators of neurotransmitter release) identified in both homogenization methods TL and G&LN₂. As it turned out the SDC buffer declared unsuitable for extraction of dermal proteins.

However, 5 proteins overlapped in G&LN₂ methods both urea and SDC, mainly c-like heterogeneous nuclear ribonucleoproteins and binding proteins. Furthermore, 5 other proteins could be extracted both with urea and SDC using the TL. These proteins typically belong to protein classes: cytoskeletal protein, chaperone, hydrolase, and nucleic acid binding.

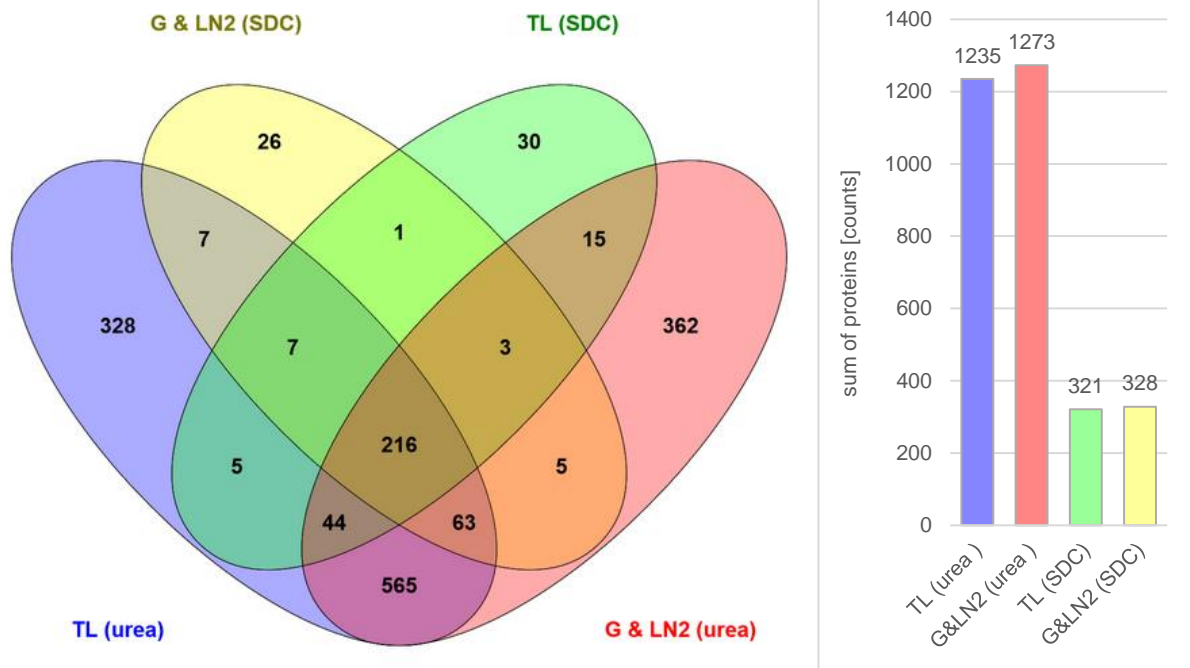


Figure 26: Statistical analysis of the LC-MS/MS data from tryptic digested peptides of dermis tissues homogenized with two different conventional, mechanical methods and two different TLBs. *Left:* Venn diagram of two classical methods and two different TLBs pro each method: TL (urea), TL (SDC), G&LN₂ (urea), G&LN₂ (SDC) [64]. *Right:* bar graph of a total number of identified proteins (minus repeated proteins) in approaches: TL (urea), TL (SDC), G&LN₂ (urea), G&LN₂ (SDC).

Of peculiar interest were the numbers identified exclusively in one experiment. 328 proteins were exclusively identified in TL (urea), 362 in G&LN₂ (urea), 30 in TL (SDC) and 26 proteins in G&LN₂ (SDC). The Proteins exclusively identified in one homogenization method with a particular TLB were enriched by using DAVID [65] as described above. The lists of these proteins were uploaded to DAVID [65] and were enriched against the background library with the enrichment precondition as described above. The clustering results of enrichment analysis of those data are shown in figures 27 to 30. These results show how different methods can yield different issues due to the molecular diversity and physicochemical properties of proteins.

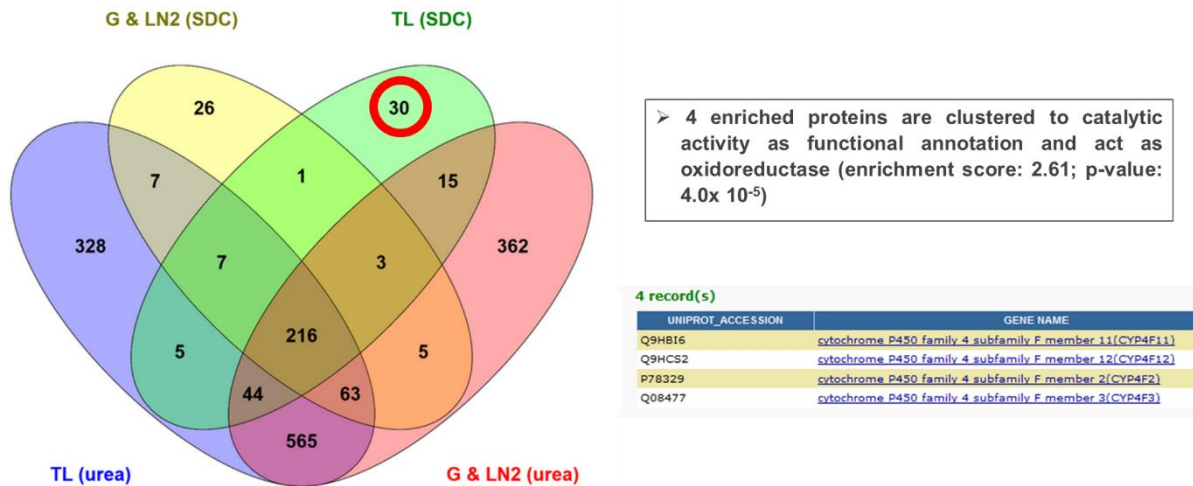


Figure 27: Left: Venn diagram of two classical methods and two different TLBs pro each method. 30 proteins are included exclusively in TL (SDC). right: 4 enriched proteins are clustered catalytic activity as functional annotation by the DAVID enrichment analysis.

The 30 proteins (highlighted in figure 27) homogenized and extracted exclusively with TL (SDC) yielded in 4 enriched proteins by the DAVID enrichment analysis according to their function as catalytic activity enzymes with an enrichment score of 2.61 and p-value: 4.0×10^{-6} . These proteins may act as the oxidoreductase.

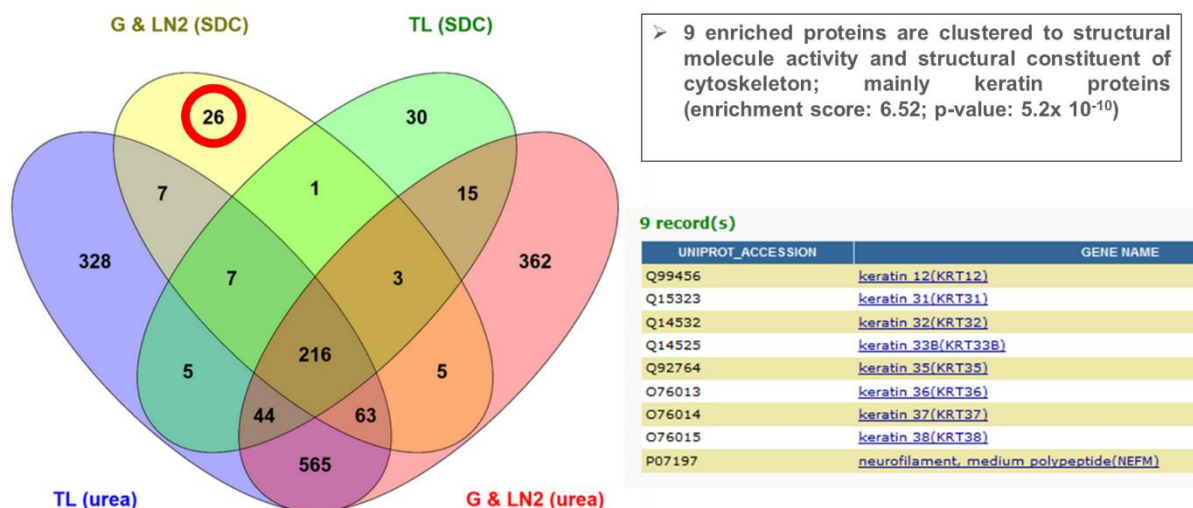


Figure 28: Left: Venn diagram of two classical methods and two different TLBs pro each method. 26 proteins are included exclusively in G&LN₂ (SDC). Right: 9 enriched proteins, mainly keratin proteins type I, are clustered to a structural constituent of cytoskeleton as functional annotation by the DAVID enrichment analysis.

The 26 proteins homogenized and extracted exclusively with G&LN₂ (SDC) yielded in 9 proteins by the DAVID enrichment analysis with an enrichment score of 6.52 and p-value: 5.2×10^{-10} (figure 28). The enriched proteins belong mainly to keratin, type I protein group (KRT12, KRT31, KRT32, KRT33B, KRT35, KRT36, KRT37, and KRT38). Generally speaking, the keratins are classified as a cytoskeletal system consisting intermediate filaments (IF) group with 54 varied functional genes in the human and is the key function of the mechanical stability and integrity of epithelial cells and tissues. Further, a part of keratins features intracellular signaling functions e.g. apoptosis, wound healing and protection from stress, which explains the self-renewing process of skin beginning with proliferation, differentiation and ending with desquamation or shedding. The keratins are separated into two groups due to their molecular diversity. The keratin type I group consists of the acidic proteins and the type II of basic to neutral proteins. In contrast to the other IF proteins, keratin filaments can be formed only as a hetero-polymeric pair of type I and type II in a ratio of 1:1 [92]. The identification of the acidic keratin proteins, type I: KRT12, KRT31, KRT32, KRT33B, KRT35, KRT36, KRT37, and KRT38, which are mainly keratins of the hair fiber (except KRT12, an epithelial keratin), were occurred in the case of using the G&LN₂-method and the SDC-buffer.

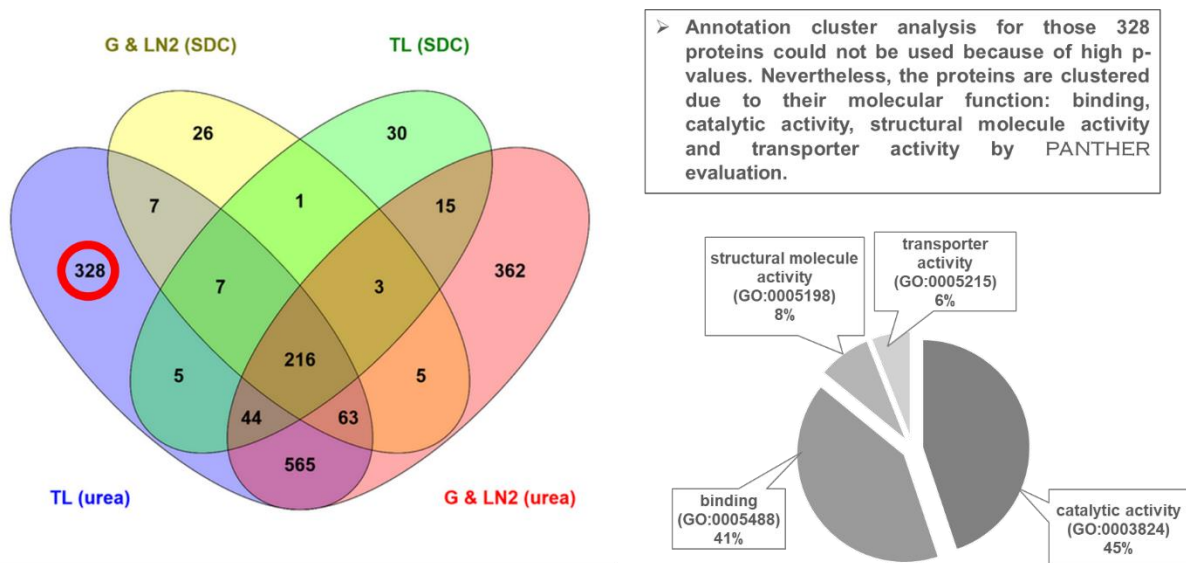


Figure 29: Left. Venn diagram of two classical methods and two different TLBs pro each method. 328 proteins are included exclusively in TL (urea). There was no clustering impossible because of high p-values. Right. pie chart shows the results of the molecular function of all 328 proteins evaluated by PANTHER.

The enrichment and clustering analysis by DAVID were conducted for the 328 proteins exclusively identified proteins in samples homogenized and extracted with TL (urea) as explained before. But the analysis resulted in a high p-value which exceeds the cut-off filter p-

value less than 5.0×10^{-4} , suggesting no enriched proteins. Nevertheless, the PANTHER evaluation shows 112 of these proteins are intracellular, and 55 membrane proteins which are consistent with the results of DAVID out of the cut off filter partly. In figure 29, the molecular function of the 328 proteins is demonstrated in a pie chart additionally.

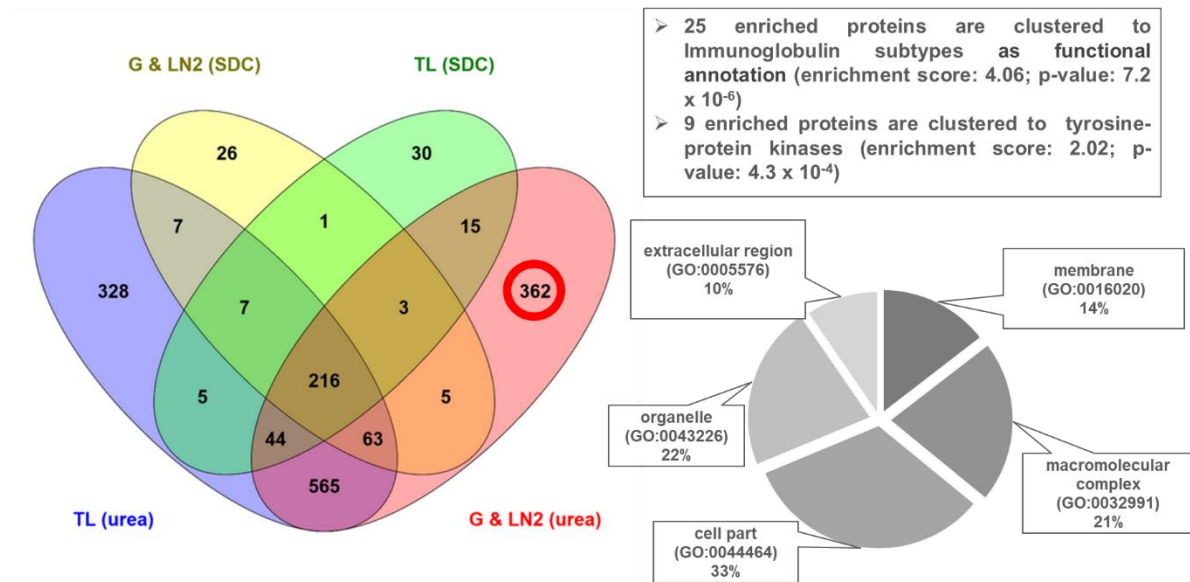


Figure 30: Left: Venn diagram of two classical methods and two different TLBs pro each method. 362 proteins are included exclusively in G&LN₂ (urea). 25 enriched proteins are clustered to immunoglobulin subtypes, and 9 further enriched proteins are clustered to tyrosine protein kinases as functional annotation by the DAVID enrichment analysis.

The 362 proteins (highlighted in figure 30) homogenized and extracted exclusively with G&LN₂ (urea) yielded in 25 enriched proteins by the DAVID enrichment analysis according to their function as immunoglobulin subtypes with an enrichment score of 4.06 and p-value: 7.2×10^{-6} . The 9 further enriched proteins are clustered to tyrosine protein kinases with an enrichment score of 2.02 and p-value: 4.3×10^{-4} . The PANTHER evaluation in pie chart diagram illustrates the cellular component GO classification. The most identified proteins obtained exclusively with G&LN₂ (urea) were intracellular proteins (0.33), followed by organelle (22%), macromolecular complex (21%), membrane (14%) and extracellular region (10%).

4.1.5. Results of homogenized dispase-separated skin tissues by PIRL ablation

In the next paragraphs, the protein identification of dispase-separated skin tissues homogenized via PIRL-ablation is described for dermis and epidermis samples. Furthermore, the two different TLB – urea and SDC– extraction protocols were used here too; thus, the comparison of results is made as performed for the classical homogenization techniques. Finally, the results of borosilicate filter paper as trapping is demonstrated for dermal and epidermal tissues depending on the ablation time.

Some of the epidermal tissues were submitted for PIRL-ablation in one piece and the others spread out on glass slides. Surprisingly, the results of protein identification of ablated epidermal tissues spread out on glass slides indicate a higher protein yield than those in one piece. The results are shown in figure 31, where the mean values of all proteins counted in both cases are diagrammed in a bar chart with the corresponding error bar. Epidermal tissues spread-out on glass slides feature a mean of 1633 proteins in contrast to samples ablated in one piece with a mean of 658, a 2.5-fold lower. In both cases, the protein recovery within the biological replicates in regard to the protein yields was very high. The Venn diagram represents the protein distribution of both experiment sets. All proteins, identified in all biological replicates of each set (minus the repeated proteins), were used for this Venn diagram. The intersection of the two sets is about 881 proteins. Exclusively 1275 proteins were identified with the set “on glass slide” and 162 with the set “in one piece”. In comparison to classical homogenization methods, the epidermal samples homogenized with PIRL presented a remarkable high reproducibility.

To explain the large difference between both sets, the parameters: ablation time and cooling trap shall be described in detail. The ablation time for epidermal tissues in one piece took 20 – 30 seconds. The scan time across those spread-out on glass slides was 60 seconds. During this scan time, the condensation of the ablation plume gradually occurred in the cooling trap. It is presumed that the PIRL-ablation happens quite fast for small soft tissues as epidermis, so an efficient collecting of ablation plume cannot be ensured simultaneously. A large volume of the plume can get lost before the plume condensation can take place in the cooling trap, and the aerosol is sucked to the vacuum pump. Whilst on the spread-out epidermal tissue, the laser beam is guided manually from one corner to the next hence the scan time takes longer, and the aerosol condenses step by step in the cooling trap.

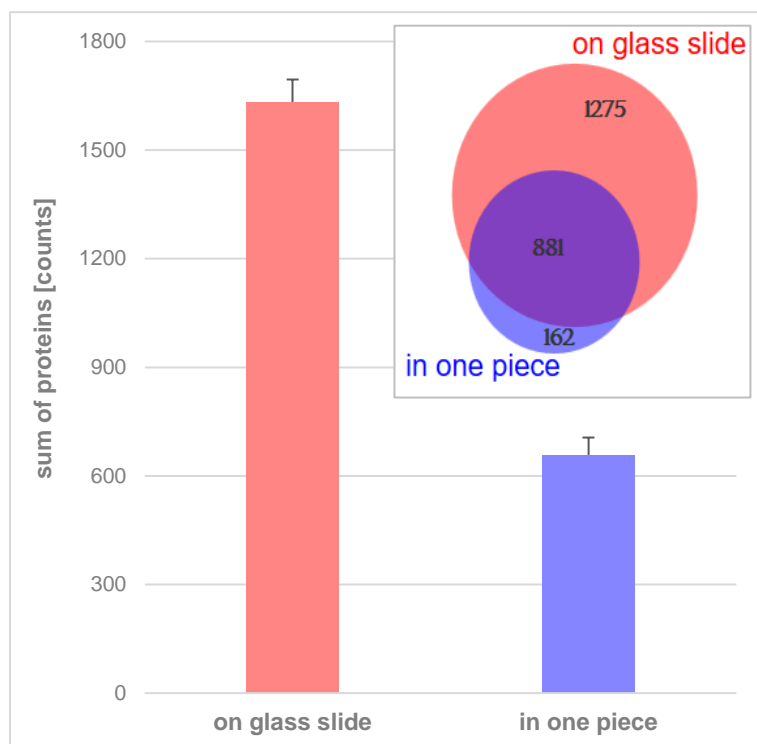


Figure 31: Statistical analysis of the LC-MS/MS data from tryptic digested peptides of epidermis samples homogenized with PIRL. The bar chart shows the mean and corresponded error bar of achieved proteins for epidermal tissues ablated in one piece or spread-out on a glass slide (biological replicates $n=3$). The Venn diagram illustrates the distribution of the numbers of proteins identified in all biological replicates represented by two experiment sets: in one piece or spread-out on a glass slide.

Another set-up was to ablate dispase-separated skin tissues – dermal and epidermal tissues– using PIRL, collect the aerosol into the 2nd generation of cooling trap (two-connected falcons' system) and extract them with two different TLBs: SDC and urea, as performed for classical homogenization techniques.

Additionally, an experiment with the dermis samples was performed to test the borosilicate filter paper as a replacement for the condensation method in the cooling trap. For this purpose, the protein yields of the respective experimental set-ups for all biological replicates were used. The mean value and the corresponding error factor were calculated for each set-up and they all were demonstrated in a bar chart in figure 32. As expected, the highest value was ascertained for epidermal tissues with urea protocol with about 800 proteins averagely. With SDC protocol the achieved mean value of epidermal proteins was almost 4-fold less, with an average of 220. The same experimental set-up for dermal tissues led to results beyond expectations. The urea protocol yielded an average of 231 proteins, barely half of the results obtained by classical homogenization. SDC protocol resulted in an astonishingly higher number of identified proteins than the urea protocol with an average of about 250 proteins. By comparing the SDC protocol results ablated with PIRL with the results of classical homogenization methods proved more compatible for extraction of PIRL homogenate than the classical one. (supplement S. 4 and S. 5 shows the comparison of chromatograms of SDC extracted samples against the urea samples).

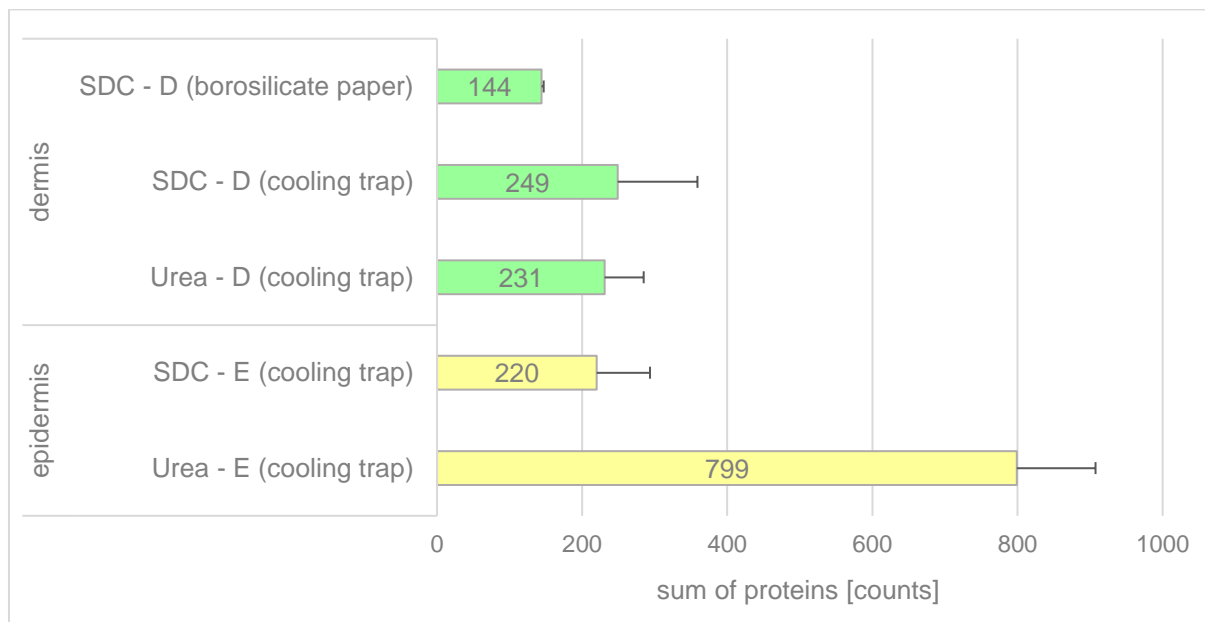


Figure 32: Statistical analysis of the LC-MS/MS data from tryptic digested peptides of dermis and epidermis samples homogenized with PIRL using two different TLBs: SDC and urea as well as the cooling trap and borosilicate filter paper. The bar chart shows the mean and corresponded error bar of achieved proteins for dermal as well as epidermal tissues (biological samples: n=4). The ablation aerosols were collected into the 2nd generation of the cooling trap. The dermal and epidermal proteins are extracted with SDC or urea. Further, the result for dermal tissues trapped into the borosilicate filter paper (1st generation of filter holder) is presented here too (biological samples: n=2).

The condensation of ablation aerosol in the cooling trap was incessantly encountering an issue: freezing of aerosol in the tubing system before reaching the trap. The system was therefore constantly interrupted, ensuring that the frozen content in the tubes to melt. Accordingly, a new trap system was built so that the condensation of aerosol was replaced by drying through deposition from the gas phase directly into the solid phase. This procedure can be explained as spray drying too, which undergoes three steps: atomization, dehydration, and powder collection [66]. The genesis of aerosol during PIRL ablation can be imagined as the atomization step, while the vacuuming represented the dehydration step whereby here the particles are caught on the borosilicate filter paper that is placed into a filter holder and powdered immediately after hitting on the paper surface (visualized in figure 11, in chapter 3.2.2.1).

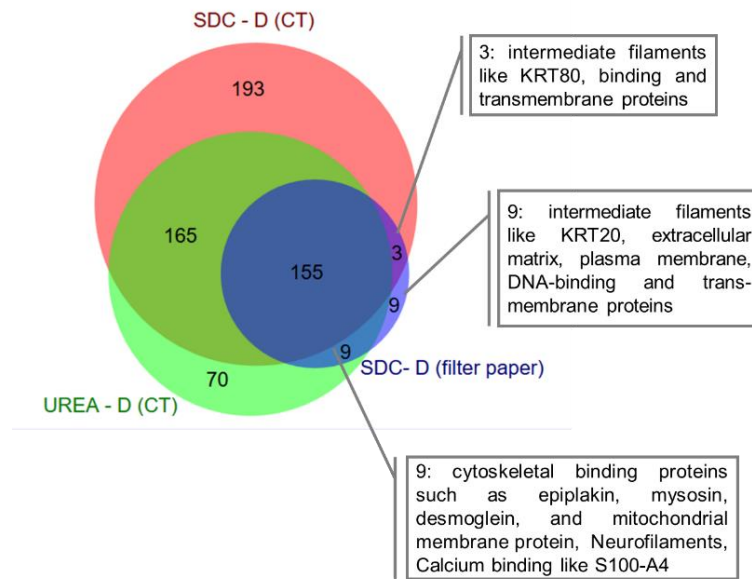


Figure 33: Statistical analysis of the LC-MS/MS data from tryptic digested peptides of dermis samples homogenized with PIRL using two different TLBs: SDC and urea as well as the cooling trap and borosilicate filter paper. The Venn diagram shows the distribution of the numbers of proteins identified in all dermal samples represented by three experiment set-ups: dermal samples collected on cooling trap (CT) and extracted with urea protocol (UREA-D (CT)); dermal samples collected on cooling trap and extracted with SDC protocol (SDC-D (CT)); dermal samples collected on borosilicate filter paper and extracted with SDC (SDC-D (filter paper)). The significant molecular functions of proteins from the respective intersections of SDC experiments.

The extraction of proteins from the borosilicate paper was established with the SDC protocol in the laboratory of a working group of PROF. DR. SCHLÜTER. Therefore, in this study, this TLB was tested for extraction of dermal proteins homogenized with PIRL. The number of identified proteins was very low with 144 proteins averagely which were relatively similar to the results achieved by classical homogenization. To understand the importance of TLBs for extraction of PIRL-ablated samples, a Venn diagram (figure 33) was generated for all experiment set-ups for dermal tissues ablated with PIRL, their results were already demonstrated in figure 32. Considering the distribution of all proteins, identified in all biological replicates of each set (minus the repeated proteins), resulted in an intersection of 3 proteins, which were represented only in SDC extracted samples, both cooling trap and filter paper. These are intermediate filaments associated proteins: basic keratin type II cytoskeletal 80 (gene name: KRT80), glial fibrillary acidic protein (type III, gene name: GFAP) and also a developmental protein called transmembrane protein 198 (gene name: TMEM198). Of major interest were an overlapping value between the SDC-D (filter paper) and UREA-D (CT) with 9 proteins and an exclusively value (9 proteins found only in SDC-D (filter paper)). In the intersection of SDC (filter paper) and UREA (CT), cytoskeletal binding proteins such as epiplakin (gene name: EPPK1), myosin-13 (gene name: MYH13), desmoglein-1 (gene name:

DSG1) and S100-A4 were found. Additionally, mitochondrial membrane protein and neurofilaments polypeptide proteins were also identified. Exclusively in SDC-D (filter paper) intermediate filament proteins like keratin, type I cytoskeletal 20 (gene name: KRT20) which exhibits structural constituent of cytoskeleton as molecular function and plays a main role in keratinization, an apoptotic process like cornification. Besides, extracellular matrix, plasma membrane, DNA-binding and transmembrane proteins were identified only in this set-up.

The SDC buffer was found to be inefficient compared to urea buffer when the obtained protein numbers were considered more accurate. Nevertheless, with SDC buffer a broad range of protein classes were identified in addition to the protein classes identified only with urea. This knowledge points to combine the SDC protocol as well as urea protocol to increase the protein yield and high-throughput identification of protein groups. This protocol was established in this study for protein mixtures collected on borosilicate filter paper. Firstly, the proteins were extracted by SDC buffer and then 8 M urea was added to the same borosilicate filter paper to extract the remaining proteins. The protein mixtures extracted with both TLBs were pooled together on a cut-off filter. Then, buffer exchange followed to get rid of the SDC buffer. Finally, the samples were tryptically digested with the urea protocol.

To ensure high protein yields, a new experiment was carried out using the PIRL homogenization technique for dispase-separated dermal and epidermal tissues. For this experimental set-up, epidermal tissues were ablated with PIRL and the ablation plume was collected onto a borosilicate filter paper fixed into the miniaturized filter holder (2nd generation). For extraction, the new established and optimized extraction protocol with a combination of SDC and urea buffer was used. In this experiment, the ablation efficiency and its effect on protein recovery was tested as a function of ablation time. The epidermal tissues were ablated once for almost 2 min and another time for 3 min (each of experiment was performed for six technical replicates). When viewing the LC-MS/MS results of the tryptic digested peptides from epidermal tissues homogenized with PIRL, the highest protein yields and a higher and more reproducible protein recovery was observed with SDC&urea extraction protocol for borosilicate filter paper. Surprisingly, a higher number of proteins were identified after 2 min of ablation compared to 3 min ablation time. The results are shown in figure 34 with distribution scope between the replicates. After 2 min ablation, between 1660 and almost 2115 proteins were identified on the borosilicate filter paper with a mean value of 1929 proteins and a standard deviation of 157.4 between replicates. However, 3 min ablation time amounted to 1928 maximum number of identified proteins and 1316 minimum, at an average 1619 proteins and a standard deviation of 190.

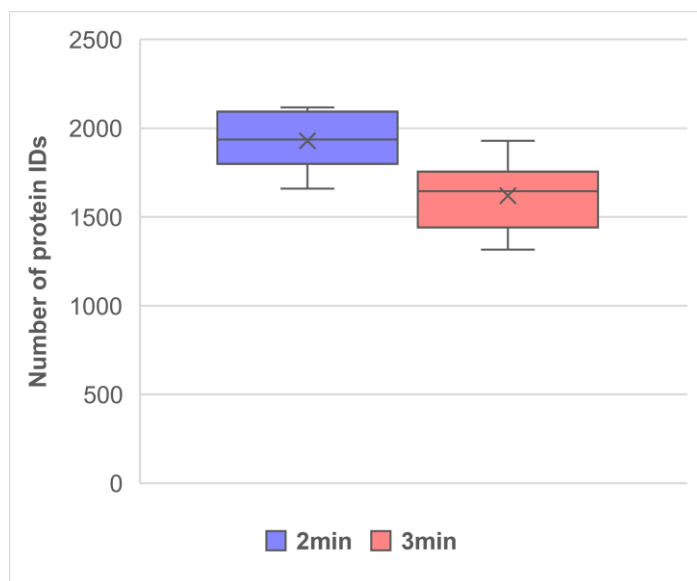


Figure 34: Statistical analysis of the LC-MS/MS data from tryptic digested peptides of epidermis samples homogenized with PIRL using SDC&urea protocol and collection of ablation plume of borosilicate filter paper – fixed into the 2nd generation of the filter holder. In the Box-graphic, mean values of identified epidermal proteins within ablation times: 2 min (mean value of identified proteins $x = 1929$) and 3 min (mean value of identified proteins $x = 1619$) are demonstrated (technical replicates $n=6$).

This experimental set-up was repeated for dermal tissues. In consequence of homogenization severity of dermal tissues, which was confirmed in the approaches before, the ablation time was chosen between 1 to 10 min. The on-filter paper collected aerosol was extracted with SDC&urea protocol and digested. As shown in figure 35, the mass spectrometric results were unsuspectedly high for 1 min ablation time. Between 710 and 1040 proteins were identified in six replicates, averagely 858 protein IDs were calculated with a standard deviation of 95.8 between the replicates. After 2- and 3-min ablation time the number of identified proteins decreased almost linearly. In the samples ablated for 2 min, 460 to 650 proteins were identified in all four replicates (mean value 533 and standard deviation 74.8) and in those ablated for 3 min between 330 and 470 proteins were counted in all four replicates (mean value 391 and standard deviation 53.4). By increasing the ablation time an increment of a number of identified proteins was observed. After 5 min ablation 615 to 670 proteins could be identified in all four replicates (mean value 652 and standard deviation 22.4). The number of proteins identified in samples ablated for 7 min was quite similar with a slightly higher quantity. In six replicates, about 640 to 750 proteins were identified (mean value 690 and standard deviation 39.6). An increase in the protein numbers was observed for 10 min ablation time. Nonetheless this was lower than the protein numbers of samples ablated for 1 min. In five replicates 560 to 820 proteins were identified (mean value 690 and standard deviation 97.0).

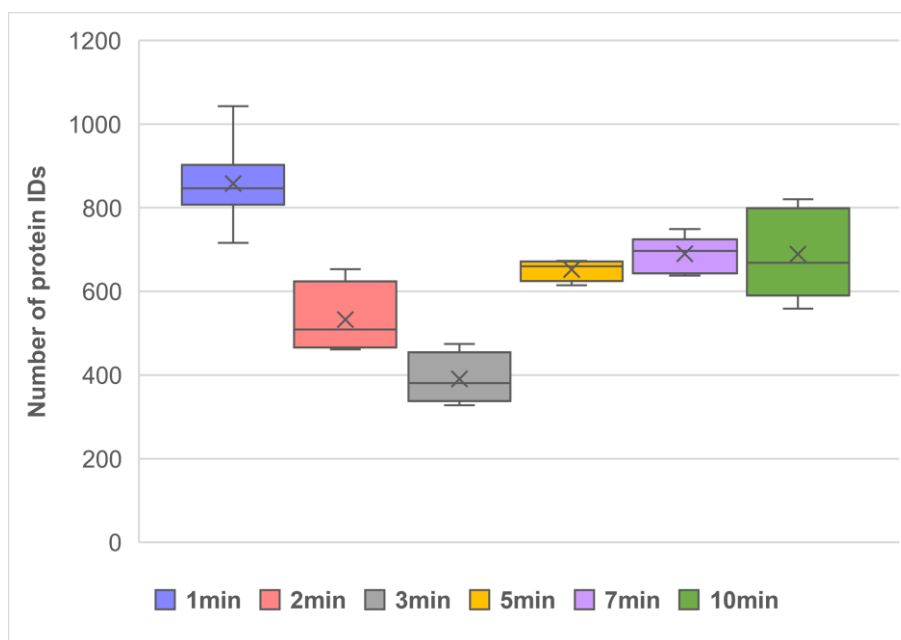


Figure 35: Statistical analysis of the LC-MS/MS data from tryptic digested peptides of dermis samples homogenized with PIRL using SDC&urea protocol and collection of ablation plume of borosilicate filter paper – fixed into the 2nd generation of the filter holder. In the Box-graphic, mean values of identified dermal proteins within ablation times: 1 min (mean value of identified proteins $x = 858$); 2 min (mean value of identified proteins $x = 1929$); 3 min (mean value of identified proteins $x = 1619$); 5 min (mean value of identified proteins $x = 1619$); 7 min (mean value of identified proteins $x = 1619$) and 10 min (mean value of identified proteins $x = 1619$) are demonstrated (biological and technical replicates).

In due consideration of standard deviation, the lowest error factor between the replicates was discovered for samples homogenized with 5 min ablation time, but the number of identified proteins suffered. The error factor between all samples ablated for 1 min was quite high but referencing the high identified numbers of proteins, this could be disregarded. Thus, the highest protein yield and protein recovery were ascertained for short time of ablation for epidermal as well as for dermal tissues. This can be explained by a fluid dynamic reaction inside the chamber. It is presumed that the pores of borosilicate filter paper are getting blocked by collected biomolecules, which was noticed by a decrease in the pressure of the vacuum pump during longer ablation time. The filter paper got blocked after 2 min which explains the low number of proteins for 2- and 3-min ablated samples. On increasing the ablation time, so it was observed that aerosol was still being vacuumed to the trap however, in a limited amount. It indicates that the laminar streaming was interrupted by irregular vacuuming through the blocked filter paper. While the laminar streams are changed to the turbulent air flow, it is anticipated that the aerosol contacts the chamber walls hence the biomolecules are adsorbed to the chamber walls. Therefore, a few biomolecules in the ablation plume were able to reach

the trap gradually as observed the slow-increasing protein numbers for 5 to 10 min ablated samples.

When comparing the mass spectrometric protein identification results of different types of trapping the ablation plume, the highest protein yield was determined by using borosilicate filter paper fixed into the trap with the screwing system (filter holder 2nd generation). The cooling trap system struggled with the undesirable freezing of tube system and blocking the flow. Incidentally, the long tube system and the large size of the trap reduced the protein yield by adsorption to its walls. Beyond that, the air humidity plus the water content in the samples were included in the aerosol and caused another disadvantageous factor known as the dilution factor. The higher the water content in the condensed aerosol, the lower the number of identified proteins affected by dilution. Looking at the borosilicate filter paper results, an enormous improvement was observed in terms of protein identification. Dehydration of protein mixtures and powdering them at the same time on the filter paper enhances not only the transportation at room temperature but also the extraction of proteins from samples homogenized using the PIRL-DIVE technique. Another point is the miniaturization of the trap, which is associated with less loss during the collection of biomolecules and less moisture dilution factor, but also in the case of filter paper, less volume of TLB is required to extract the proteins. Furthermore, the increased tightness of the filter holder with screwing system induces a constant air flow during vacuuming. As described before, the aerodynamics plays a major role in aerosol streaming to the trap under a laminar flow. Interrupting the air flow to the pump generates turbulent air flow automatically in the chamber which leads to a loss of biomolecules by adsorption on the chamber walls and consequently less captured biomolecules in the trap. Due to these factors, the protein yields as well as the reproducibility of protein recovery, require a closed flow system. Also, the contamination risk may be reduced by the optimized equipment.

4.1.6. Comparison between mechanical and PIRL-DIVE homogenization methods

Finally, the results of conventional, mechanical homogenization methods were compared with those of PIRL-DIVE homogenization method. The direct comparison of identified proteins of dispase-separated skin tissues homogenized by PIRL-DIVE and the classical homogenization methods points to the slight difference not only in the protein yields but also in the protein compositions as explained in chapters before individually for each experiment set-up.

For comparison of PIRL-DIVE homogenization technique and classical techniques as milling with beads (in TL) or powdering using mortar and pestle with freezing in liquid nitrogen (grinder & LN₂), all technical replicates for each one of biological sample homogenized with one of these techniques were pooled together and an aliquot was measured by tandem mass spectrometry. The samples were categorized based on their tissue type (dermal tissue or epidermal tissue) and set-up (classical or PIRL homogenization method) and finally the extraction buffer (urea or SDC). All proteins identified in biological samples homogenized with one method were summed together (minus repeated protein IDs), to find out how many different proteins were identified in total and which method offers the highest protein yield with a broad range of protein classes. Further, the protein coverage could be observed within the set-ups. The highest number of dermal proteins was summed for the classical method with urea as extraction buffer, whereby the PIRL methods with SDC as well as urea buffers plus the classical method with SDC buffer provided more or less in the same range (Figure 36, bar chart). Consequently, by considering the Venn diagram in figure 36 it stands out that the distribution of proteins within the intersection cannot be congruent with this low number of proteins in PIRL-UREA, PIRL-SDC, and CL-SDC. Only 254 proteins were identified in all methods. Of great importance is to know which proteins classes are exclusively identified in just one set-up. This expands the knowledge of how to cover all protein classes and to extend the through-put capacity. In this study, the main factor was to achieve a high throughput screening of proteins and protein groups to configure a protein composition data set of both main layers: dermis and epidermis. The highest number of epidermal proteins was summed for the classical method with urea as well where the other methods yielded lower number of achieved proteins. The Venn diagram (Figure 36) demonstrates the overlaps of all methods with only 563 identified proteins.

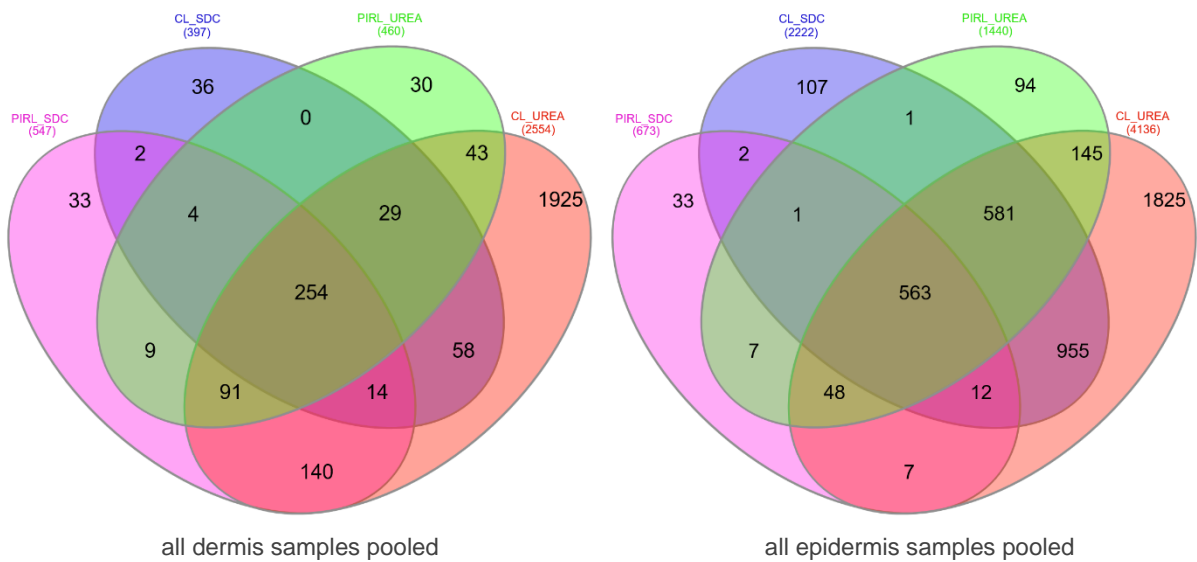
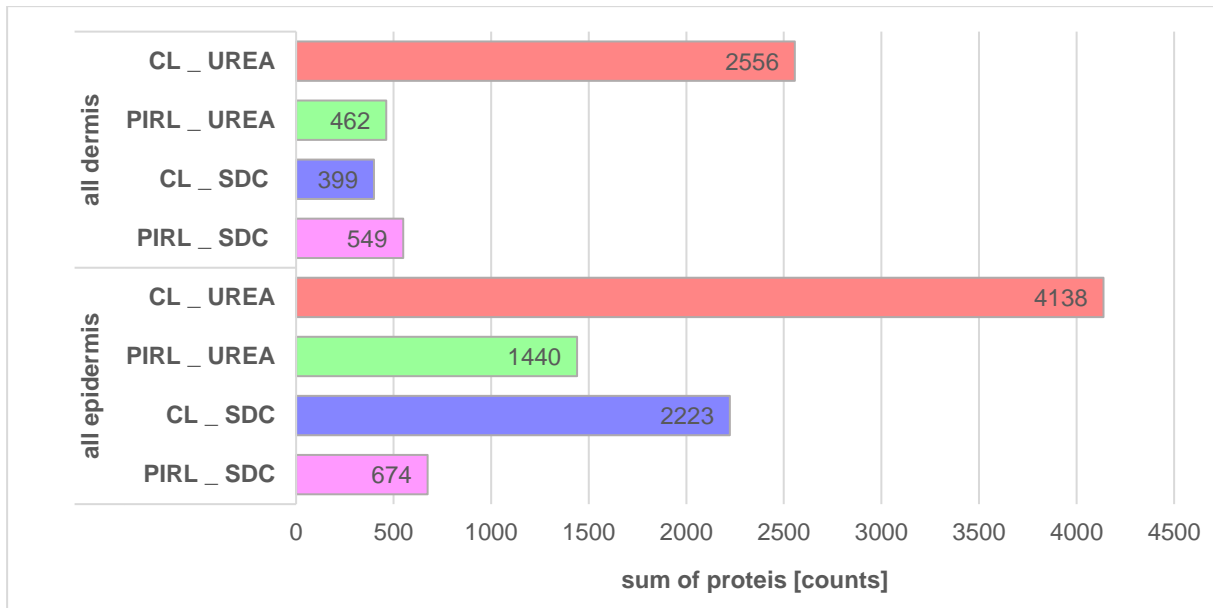


Figure 36: Comparison of PIRL-DIVE homogenization technique with classical, mechanical homogenization techniques (CL: TL or G&LN₂) for epidermis and dermis samples. Bar chart diagram shows the total number of identified proteins in all biological and technical replicates for samples homogenized classical (CL) or with PIRL and using TLBs SDC or urea for epidermal and dermal tissues. Venn diagrams show the distribution of identified proteins and their overlap for samples homogenized and extracted as described above: CL-UREA, PIRL-UREA, CL-SDC and PIRL-SDC for dermal (left) as well as epidermal (right) tissues.

4.2. Generation of the library for protein markers of dermis & epidermis

The protein composition in human skin is almost determined by transcriptomic, proteomic and antibody-based imaging approaches. In reference to the transcriptomic literature [67], 70% of all human protein-coding genes are responsible for protein biosynthesis in the skin, and 477 of these genes are elevated in protein synthesis in the skin. Particularly in epidermal cell layers, they synthesize proteins from keratinization step, from the lowest basal layer, up to the formation of the outermost cornified cell layer. In the dermis, proteins defined as elevated are accountable for the development and preservation of hair and connective tissue. The gene expression of these 477 elevated genes in skin tissue were compared to the other tissue types, as mentioned in the platform "THE HUMAN PROTEIN ATLAS" [67] and 97 genes from these elevated genes have five-fold higher mRNA levels in skin than in other tissues (term: enriched genes). The GO analysis of these 97 enriched genes was subdivided again into protein biosynthesis categories associated with keratinization, epidermal and epithelial development, differentiation, preservation of skin barrier and regulation of water loss. In depth knowledge on the structure and function of the over-presented proteins in skin cell layers is easily accessible in scientific literature. The aim of this study was to determine the protein composition of epidermal tissues. To approach this goal, an overview of the protein composition of dermal and epidermal tissues was required to facilitate distinguishing between both main layers primarily. The transcriptome analysis of skin tissues was predominantly investigated already; however, it is lacking in the proteomic approaches a complete overview of proteins occurred in dermal and epidermal tissues. Therefore, in this study, it was proceeding with the creation of a general protein marker library for all proteins occurring exclusively in the epidermis and a library for all proteins exclusively in the dermis. Due to this fact, dispase-digested skin tissues – into the two main layers: dermis and epidermis – enabled a protein collage of each layer via mass spectrometric analysis. Based on the results obtained in this study so far, it was decided to combine the results of all three homogenization methods to increase the number of identified proteins, thus to enhance the specific protein database. As the results shown before, each homogenization method showed a particular number of protein classes, which could be identified exclusively by using one of these three techniques, PIRL or TL or G&LN₂. A combination of all three methods led to a wide range of protein classes and therefore all three were selected. The same applies to the use of different tissue lysis buffers for protein extraction. SDC TLB was unsuitable for protein extraction of skin tissues but it was able to extract protein classes which were missed by extraction with urea TLB.

The protein library was generated from the mass spectrometric data from all available biopsies from breast and abdominal tissue areas. Firstly, these tissues were dissociated enzymatically with dispase II as explained in chapter 3.1.2 into dermal and epidermal tissues, which were

homogenized with PIRL or TL or G&LN₂ techniques and the proteins were extracted and solubilized by using SDC or urea or SDC&urea. The LC-MS/MS data were combined to one list for epidermis samples and one for dermis samples. Proteins identified in at least 10 samples and with unique peptides ≥ 1 was used for the protein marker library. In total 2066 protein IDs were counted in epidermis samples and 1629 proteins in dermis samples. The intersection of epidermal and dermal proteins is illustrated in a Venn diagram in figure 37. 1355 proteins were identified in both samples thus they cannot be used as marker proteins for each of both main layers. Therefore, 274 proteins as dermal marker proteins and 1311 as epidermal marker proteins were identified.

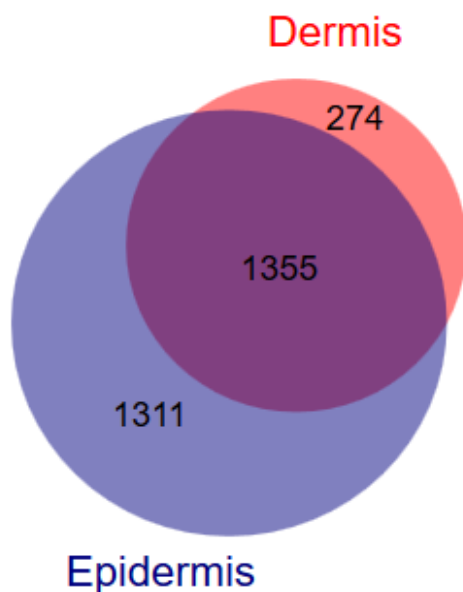
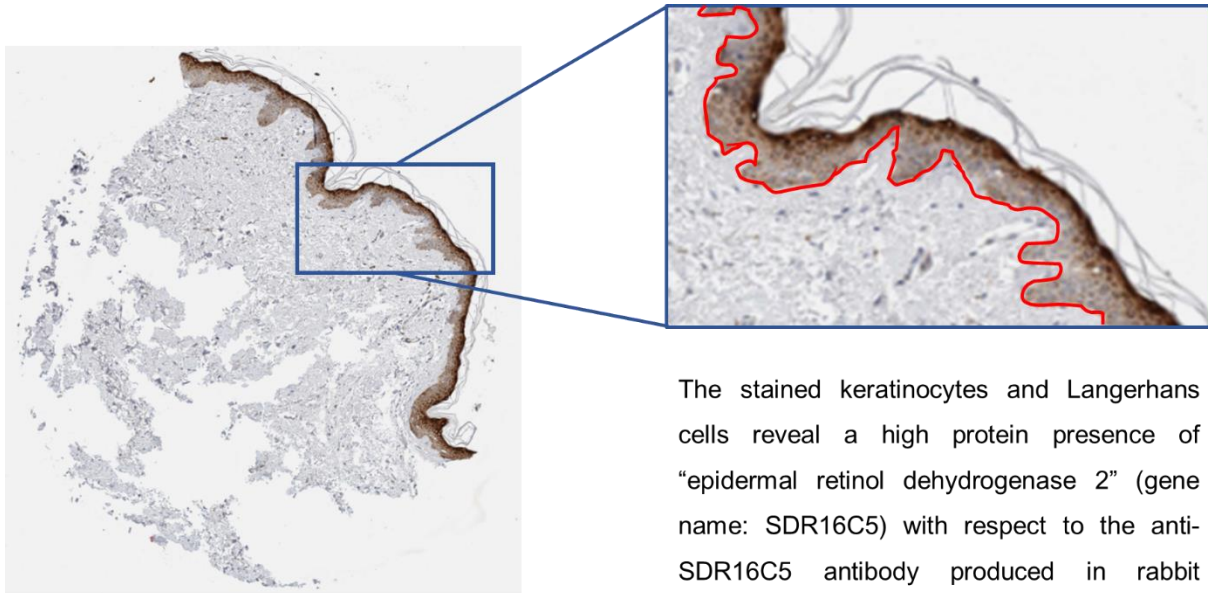


Figure 37: Protein marker library generation of dermis and epidermis. Venn diagram illustrates the distribution of a number of identified proteins in the dermis (274 exclusively) as well as in epidermis (1311 exclusively) samples and the overlap of proteins identified in both samples (1355).

Finally, the protein marker list was validated by considering the immunohistochemistry (IHC) image database using the platform “THE HUMAN PROTEIN ATLAS” [67]. Accordingly, the protein marker lists were compared by reference to the location of immunohistochemical staining cell domains in the human skin tissues. This can be illustrating by an example: epidermal retinol dehydrogenase 2 (gene name: SDR16C5, UNIPROT accession number Q8N3Y7).



The stained keratinocytes and Langerhans cells reveal a high protein presence of “epidermal retinol dehydrogenase 2” (gene name: SDR16C5) with respect to the anti-SDR16C5 antibody produced in rabbit (HPA025224)

Figure 38: the Immunohistochemical image of stained human skin tissue section represented the epidermal retinol dehydrogenase 2 (gene name: SDR16C5) with respect to the anti-SDR16C5 antibody [68]. Zoom-in image shows brown stained keratinocytes and Langerhans cells in the epidermal area of skin tissue. The red line visualizes the border between epidermal and dermal area.

In figure 38, the validation is explained due to an IHC image of a protein. The tissue section was stained by immunohistochemical reaction of anti-SDR16C5 antibody (antibody HPA025224 produced in rabbit). The IHC product occasions the brown stained cells which show the presence of epidermal retinol dehydrogenase 2 in keratinocytes and Langerhans cells. The red dividing-line visualizes the border between epidermis and dermis. As stated by the database of “THE HUMAN PROTEIN ATLAS” [67], no IHC reaction is observed in melanocytes (stratum basale and stratum spinosum) and in fibroblast cells (dermis).

The data interpretation of IHC images in the database of “THE HUMAN PROTEIN ATLAS” [67] was utilized to validate the protein markers from the entire epidermal and dermal lists protein by protein. The library is made up of the level of protein present in the following cell types –

- fibroblasts (dermis),
- keratinocytes (stratum basale up to stratum corneum),
- Langerhans cells (stratum basale and stratum spinosum),
- Melanocytes (stratum basale and stratum spinosum) –

with the terms low, medium, high and not detected (in some cases the information was missed, therefore it was mentioned as “empty box” or “unavailable”). Moreover, the protein markers were categorized on the basis of their IHC results due to their presence rates in the above-mentioned cell types. For epidermal protein marker library, those proteins which covered at least one high level (as IHC result) in at least one of cell types in epidermal layers (keratinocytes, Langerhans cells or Melanocytes) but not detected in fibroblasts, represent the highest protein marker category “I”. Those epidermal proteins with at least one medium presence level in at least one of those cell types represent the medium protein marker category “II”. Eventually, those proteins with at least one low presence level in at least one of those cell types represent the low protein marker category “III”. These categorized groups enable the usage of the protein markers with certainty due to their present rate in the cell types. For epidermis protein marker list 319 protein markers were qualified. The same procedure was performed for the dermal protein marker library with an important distinction: the proteins need to be detected in fibroblasts but not in other cell types (no presence in cell types of the epidermis). In total, 51 proteins were listed as protein markers for dermis. The IHC results for those proteins indicate categories “II” (medium presence level in fibroblasts) and “III” (low presence level in fibroblasts). The category “I” (high presence level in fibroblasts) is not existing regarding the present levels of proteins in fibroblasts (only medium and low detected).

The original libraries are available in the databank of PROF. DR. SCHLÜTER working group that contains more information; e.g. the proteins lists were compared to the 97 enriched gene lists (97 genes with a 5-fold higher presence rate in skin tissue than other tissues). Besides, the protein lists were compared to the platform for protein marker discovery “OLINK PROTEOMICS” [69]. The protein libraries for both layers includes UNIPROT accession numbers [71], gene names, protein description, molecular weight, amino acids lengths, isoelectric point, IHC results (accession number is linked to the corresponded site of the database platform “THE HUMAN PROTEIN ATLAS” [67]) as well as to the protein marker discovery assays (linked to the corresponded site of the database platform “OLINK PROTEOMICS” [69]).

The relevant data of the top 50 most abundant protein markers of the epidermis and the entire dermis library (validated by “THE HUMAN PROTEIN ATLAS” [67]) are summarized in the tables 8 and 9. Moreover, the entire validated protein marker lists plus the general libraries of epidermis and dermis are attached in the supplement S.6.

Results and discussion

Table 8: The top 50 most abundant Protein markers of epidermis library (validated by “The Human Protein Atlas” [67]). The following information is listed: categories I (high) and II (medium), protein description, gene names, accession (UNIPROT accession numbers) and molecular weight (MW in kDa). The proteins in each category are listed descending order due to their numbers of detected unique peptides.

category	protein description	gene name	accession (UNIPROT)	MW [kDa]
I	Alpha-2-macroglobulin-like protein 1	A2ML1	A8K2U0	181.7
I	Sciellin	SCEL	O95171	35.9
I	Zinc finger protein 185	ZNF185	O15231	138.3
I	Dermokine	DMKN	Q6E0U4	81.8
I	T-complex protein 1 subunit eta	CCT7	Q99832	73.3
I	Serine protease inhibitor Kazal-type 5	SPINK5	Q9NQ38	11.6
I	Prostaglandin G/H synthase 1	PTGS1	P23219	88.8
I	Serpin B4	SERPINB4	P48594	23.8
I	FACT complex subunit SSRP1	SSRP1	Q08945	23.7
I	Epidermal retinol dehydrogenase 2	SDR16C5	Q8N3Y7	11.7
I	Keratinocyte differentiation-associated protein	KRTDAP	P60985	24.7
I	60S ribosomal protein L35	RPL35	P42766	46.4
I	Phosphatidylinositol transfer protein beta isoform	PITPNB	P48739	21.4
I	Ankyrin repeat domain-containing protein 35	ANKRD35	Q8N283	29.2
I	Eukaryotic translation initiation factor subunit K	EIF3K	Q9UBQ5	28.9
I	Poly(U)-specific endoribonuclease	ENDOUB	P21128	16.4
I	40S ribosomal protein S4. Y isoform 1	RPS4Y1	P22090	26.2
I	Serine/threonine-protein phosphatase 2A 55 kDa regulatory subunit B alpha isoform	PPP2R2A	P63151	89.4
I	Serine/arginine-rich splicing factor 9	SRSF9	Q13242	51.8

Results and discussion

category	protein description	gene name	accession (UNIPROT)	MW [kDa]
I	Protein S100-A7A	S100A7A	Q86SG5	39.6
I	Nucleolar RNA helicase 2	DDX21	Q9NR30	32.0
I	Nucleolar protein 3	NOL3	O60936	110.4
I	Glucosylceramidase	GBA	P04062	20.0
I	Desmocollin-2	DSC2	Q02487	83.7
I	Eukaryotic translation initiation factor 3 subunit G	EIF3G	O75821	61.7
I	Phosphatidylinositol transfer protein alpha isoform	PITPNA	Q00169	119.3
I	Protein FAM83B	FAM83B	Q5T0W9	48.9
I	Tumor susceptibility gene 101 protein	TSG101	Q99816	17.7
I	Specifically androgen-regulated gene protein	SARG	Q9BW04	22.4
I	Protein FAM49B	FAM49B	Q9NUQ9	142.1
I	Melanocyte protein PMEL	PMEL	P40967	68.2
I	NADH dehydrogenase [ubiquinone] iron-sulfur protein 4. mitochondrial	NDUFS4	O43181	80.5
I	Lymphocyte antigen 6D	LY6D	Q14210	47.3
I	p53 apoptosis effector related to PMP-22	PERP	Q96FX8	46.5
I	Leucine-rich repeat-containing protein 1	LRRC1	Q9BTT6	39.3
I	AP-1 complex subunit mu-1	AP1M1	Q9BXS5	59.2
I	Calcium-activated chloride channel regulator 2	CLCA2	Q9UQC9	61.2
I	Exocyst complex component 5	EXOC5	O00471	107.5
I	Cytochrome b-c1 complex subunit 8	UQCRQ	O14949	309.2
I	Kallikrein-8	KLK8	O60259	23.5
I	Isocitrate dehydrogenase [NAD] subunit gamma. mitochondrial	IDH3G	P51553	59.9
I	Ribosome biogenesis regulatory protein homolog	RRS1	Q15050	43.4

Results and discussion

category	protein description	gene name	accession (UNIPROT)	MW [kDa]
I	Splicing factor 3B subunit 5	SF3B5	Q9BWJ5	36.7
I	Protein dpy-30 homolog	DPY30	Q9C005	57.7
I	Claudin-1	CLDN1	O95832	58.4
II	Suprabasin	SBSN	Q6UWP8	22.4
II	Protein POF1B	POF1B	Q8WVV4	19.5
II	Involucrin	IVL	P07476	45.1
II	Keratinocyte proline-rich protein	KPRP	Q5T749	38.5
II	Arachidonate 12-lipoxygenase. 12R-type	ALOX12B	O75342	38.4

Table 9: Protein marker library of the dermis. The following information is listed: category II (medium) and III (low), protein description, gene names, accession (UNIPROT accession numbers [71]) and molecular weight (MW in kDa). The proteins in each category are listed descending order due to their numbers of detected unique peptides.

category	protein description	gene name	accession (UNIPROT)	MW [kDa]
II	Macrophage mannose receptor 1	MRC1	P22897	165.9
II	Coagulation factor XIII A chain	F13A1	P00488	83.2
II	Kininogen-1	KNG1	P01042	71.9
II	Complement C1r subcomponent	C1R	P00736	80.1
II	Complement C1s subcomponent	C1S	P09871	76.6
II	3-ketoacyl-CoA thiolase. mitochondrial	ACAA2	P42765	41.9
II	IgG receptor FcRn large subunit p51	FCGRT	P55899	39.7
II	WNT1-inducible-signaling pathway protein 2	WISP2	O76076	26.8

Results and discussion

category	protein description	gene name	accession (UNIPROT)	MW [kDa]
II	Nesprin-3	SYNE3	Q6ZMZ3	112.1
II	Cartilage intermediate layer protein 1	CILP	O75339	132.5
II	Vasorin	VASN	Q6EMK4	71.7
III	Synemin	SYNM	O15061	172.7
III	Alpha-1B-glycoprotein	A1BG	P04217	54.2
III	Phosphoglucomutase-like protein 5	PGM5	Q15124	62.2
III	Inter-alpha-trypsin inhibitor heavy chain H2	ITIH2	P19823	106.4
III	Calponin-1	CNN1	P51911	33.2
III	PDZ and LIM domain protein 7	PDLIM7	Q9NR12	49.8
III	Dihydropyrimidinase-related protein 3	DPYSL3	Q14195	61.9
III	Integrin-linked protein kinase	ILK	Q13418	51.4
III	Dipeptidyl peptidase 4	DPP4	P27487	88.2
III	Band 3 anion transport protein	SLC4A1	P02730	101.7
III	Laminin subunit alpha-2	LAMA2	P24043	343.7
III	Cathepsin G	CTSG	P08311	28.8
III	Complement factor H-related protein 5	CFHR5	Q9BXR6	64.4
III	Target of Nesh-SH3	ABI3BP	Q7Z7G0	118.6
III	Myelin protein P0	MPZ	P25189	27.5
III	Serine protease HTRA1	HTRA1	Q92743	51.3
III	Serine/threonine-protein phosphatase CPPED1	CPPED1	Q9BRF8	35.5
III	Twinfilin-2	TWF2	Q6IBS0	39.5
III	Spondin-1	SPON1	Q9HCB6	90.9
III	Kallistatin	SERPINA4	P29622	48.5

Results and discussion

category	protein description	gene name	accession (UNIPROT)	MW [kDa]
III	Bone marrow proteoglycan	PRG2	P13727	25.2
III	PDZ and LIM domain protein 3	PDLIM3	Q53GG5	39.2
III	Myelin basic protein	MBP	P02686	33.1
III	BTB/POZ domain-containing protein KCTD8	KCTD8	Q6ZWB6	52.4
III	Aldose 1-epimerase	GALM	Q96C23	37.7
III	Coactosin-like protein	COTL1	Q14019	15.9
III	BAG family molecular chaperone regulator 2	BAG2	O95816	23.8
III	Adipogenesis regulatory factor	ADIRF	Q15847	7.9
III	Spectrin beta chain. erythrocytic	SPTB	P11277	246.3
III	Antileukoproteinase	SLPI	P03973	14.3
III	Sex comb on midleg-like protein 2	SCML2	Q9UQR0	77.2
III	Eosinophil cationic protein	RNASE3	P12724	18.4
III	Protocadherin beta-2	PCDHB2	Q9Y5E7	87.2
III	Microfibrillar-associated protein 5	MFAP5	Q13361	19.6
III	Collagen alpha-1(IX) chain	COL9A1	P20849	91.8
III	Complement factor H-related protein 2	CFHR2	P36980	30.6
III	Coiled-coil domain-containing protein 80	CCDC80	Q76M96	108.1
III	Adenylyl cyclase-associated protein 2	CAP2	P40123	52.8
III	UPF0587 protein C1orf123	C1orf123	Q9NWX4	18.0
III	Adenosine deaminase	ADA	P00813	40.7

4.3. The distinction between breast and abdominal skin biopsies

In this study, two different regions of skin tissues were used for all experiments, in particular, breast and abdominal skin tissues from reduction surgeries. Of peculiar interest is the knowledge about the difference of protein composition from diverse skin regions from the human body. The distinct thickness of different types of skin tissues is known. The upper medial eyelid is deemed to be the thinnest skin in the human body with 800 μm of thickness on average and the soles of feet with 6 mm is the thickest. The varying thickness of epidermis and dermis is one of the differences depending on the localization of skin in the body but also the proteome composition from various regions of skin can be differed as stated in literature [2]. Therefore, the mass spectrometric results of the dispase-separated epidermis and dermis samples which were homogenized with PIRL-DIVE and classical methods were divided into their origin region, namely breast and abdominal. The results provided as expected a diversity in the protein composition. By considering the dermis proteins, the overlapped proteins which were included as well in epidermis protein lists were removed firstly. All dermis samples resulted in 2472 exclusive dermal proteins detected in both breast and abdominal biopsies. 707 proteins were identified only in breast tissues and 100 dermal proteins in abdominal tissues and 1665 proteins in both tissue regions (figure 39).

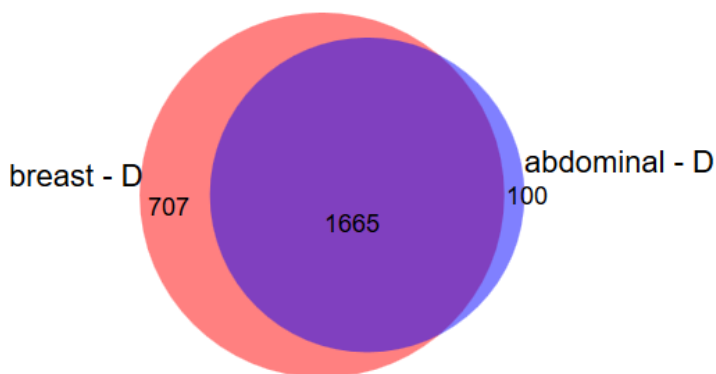


Figure 39: Venn diagram of all dermis (D) proteins identified in both breast and abdominal skin tissues. The 1665 proteins in intersection belong to both tissue regions. 707 proteins were identified exclusively in breast and 100 exclusively in abdominal regions.

In total 36 dermal protein markers were discovered exclusively in breast tissues (from those 707 proteins). These 36 protein markers are listed in table 10 which shows their protein classes. Mostly they are plasma and membrane proteins from extra- or intracellular compartments when searched against "THE HUMAN PROTEIN ATLAS" database [67]. Some of these proteins are included in the pathogenesis of cancer, neurodegenerative and various other diseases. No protein marker was discovered in those 100 proteins identified exclusively in abdominal tissues.

Table 10: 36 dermal protein markers discovered exclusively in breast tissues. There are listed: accession (UNIPROT accession numbers [71]), protein description, gene names and protein classes (* protein not available in “THE HUMAN PROTEIN ATLAS” database [67]; information obtained on UNIPROT platform). The first four proteins belong to the categorized dermal protein markers (category II and category III).

accession (UNIPROT)	protein description	gene names	protein classes
Q6EMK4 (II)	Vasorin	VASN	– Plasma proteins – Predicted membrane proteins
O95816 (III)	BAG family molecular chaperone regulator 2	BAG2	– Plasma proteins – Predicted intracellular proteins
Q9UQR0 (III)	Sex comb on midleg-like protein 2	SCML2	– Plasma proteins – Predicted intracellular proteins
P12724 (III)	Eosinophil cationic protein	RNASE3	– Predicted secreted proteins
Q13683	Integrin alpha-7	ITGA7	– Disease related genes – Predicted intracellular proteins – Predicted membrane proteins
P06727	Apolipoprotein A-IV	APOA4	– Candidate cardiovascular disease genes – Plasma proteins – Predicted secreted proteins
P48681	Nestin	NES	– Plasma proteins – Predicted intracellular proteins
P11678	Eosinophil peroxidase	EPX	– Disease related genes – Enzymes – Potential drug targets – Predicted secreted proteins
Q6PCB0	von Willebrand factor A domain-containing protein 1	VWA1	– Predicted intracellular proteins – Predicted secreted proteins
P35625	Metalloproteinase inhibitor 3	TIMP3	– Cancer-related genes – Disease related genes – Predicted secreted proteins
Q13976	cGMP-dependent protein kinase 1	PRKG1	– Disease related genes – Enzymes – Plasma proteins – Potential drug targets – Predicted intracellular proteins
O95967	EGF-containing fibulin-like extracellular matrix protein 2 (Fibulin-4)	EFEMP2	– Disease related genes – Plasma proteins – Predicted intracellular proteins – Predicted secreted proteins
Q06278	Aldehyde oxidase	AOX1	– Enzymes – Plasma proteins – Predicted intracellular proteins
Q9UMS6	Synaptopodin-2	SYNPO2	– Predicted intracellular proteins

accession (UNIPROT)	protein description	gene names	protein classes
P18428	Lipopolysaccharide-binding protein	LBP	<ul style="list-style-type: none"> – Plasma proteins – Predicted secreted proteins – Transporters
P05362	Intercellular adhesion molecule 1	ICAM1	<ul style="list-style-type: none"> – Cancer-related genes – Candidate cardiovascular disease genes – CD markers – FDA approved drug targets – Plasma proteins – Predicted membrane proteins – Predicted secreted proteins
O14558	Heat shock protein beta-6	HSPB6	<ul style="list-style-type: none"> – Predicted intracellular proteins
P07358	Complement component C8 beta chain	C8B	<ul style="list-style-type: none"> – Disease related genes – Plasma proteins – Predicted intracellular proteins – Predicted secreted proteins
Q6P0A1*	Protein FAM180B	FAM180B	<ul style="list-style-type: none"> – membrane proteins
Q9Y680	Peptidyl-prolyl cis-trans isomerase FKBP7	FKBP7	<ul style="list-style-type: none"> – Enzymes – Predicted secreted proteins
Q5JUR7	Testis-expressed protein 30	TEX30	<ul style="list-style-type: none"> – Predicted intracellular proteins
P28906	Hematopoietic progenitor cell antigen CD34	CD34	<ul style="list-style-type: none"> – CD markers – Predicted membrane proteins
P31995*	Low-affinity immunoglobulin gamma Fc region receptor II-c	FCGR2C	<ul style="list-style-type: none"> – Plasma proteins – membrane proteins
Q6UXI7	Vitrin	VIT	<ul style="list-style-type: none"> – Predicted intracellular proteins – Predicted secreted proteins
P53420	Collagen alpha-4(IV) chain	COL4A4	<ul style="list-style-type: none"> – Cancer-related genes – Disease related genes – Plasma proteins – Predicted secreted proteins
Q14588	Zinc finger protein 234	ZNF234	<ul style="list-style-type: none"> – Predicted intracellular proteins – Transcription factors
Q6ZMJ2	Scavenger receptor class A member 5	SCARA5	<ul style="list-style-type: none"> – Predicted intracellular proteins – Predicted membrane proteins
P27169	Serum paraoxonase/arylesterase 1	PON1	<ul style="list-style-type: none"> – Cancer-related genes – Candidate cardiovascular disease genes – Disease related genes – Enzymes – Plasma proteins – Potential drug targets – Predicted secreted proteins – Transporters

Results and discussion

accession (UNIPROT)	protein description	gene names	protein classes
Q969T7	7-methylguanosine phosphate-specific 5'-nucleotidase	NT5C3B	<ul style="list-style-type: none"> – Enzymes – Predicted intracellular proteins
P06213	Insulin receptor	INSR	<ul style="list-style-type: none"> – CD markers – Disease related genes – Enzymes – FDA approved drug targets – Plasma proteins – Predicted intracellular proteins – Predicted membrane proteins – RAS pathway related proteins
Q96RW7	Hemicentin-1 (Fibulin-6)	HMCN1	<ul style="list-style-type: none"> – Disease related genes – Predicted intracellular proteins – Predicted secreted proteins
P59768	Guanine nucleotide-binding protein G(I)/G(S)/G(O) subunit gamma-2	GNG2	<ul style="list-style-type: none"> – Predicted intracellular proteins – RAS pathway related proteins
Q5SYB0	FERM and PDZ domain-containing protein 1	FRMPD1	<ul style="list-style-type: none"> – Predicted intracellular proteins
P31994	Low-affinity immunoglobulin gamma Fc region receptor II-b	FCGR2B	<ul style="list-style-type: none"> – Cancer-related genes – CD markers – Disease related genes – FDA approved drug targets – Predicted membrane proteins
Q8IUD2	ELKS/Rab6-interacting/CAST family member 1	ERC1	<ul style="list-style-type: none"> – Cancer-related genes – Disease related genes – Predicted intracellular proteins
Q2M2W7	UPF0450 protein C17orf58	C17orf58	<ul style="list-style-type: none"> – Predicted intracellular proteins – Predicted secreted proteins

By considering the epidermis proteins, the overlapped proteins which were included as well in dermis protein lists were removed. All epidermis samples resulted in 5332 exclusive epidermal proteins detected in both breast and abdominal biopsies. 1074 proteins were identified only in breast tissues and 566 epidermal proteins in abdominal tissues and 3692 proteins in both tissue regions (figure 40).

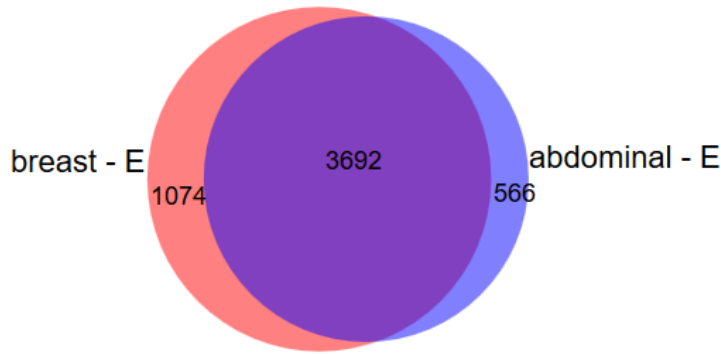


Figure 40: Venn diagram of all epidermis (E) proteins identified in both breast and abdominal skin tissues. The 3692 proteins in intersection belong to both tissue regions. 1074 proteins were identified exclusively in breast and 566 exclusively in abdominal regions.

Only 6 epidermal protein markers could be discovered in breast tissues within those 1074 proteins exclusively identified in breast tissues (table 11). These 6 protein markers are categorized mostly as intracellular proteins.

Table 11: 6 epidermal protein markers discovered exclusively in breast tissues. There are listed: accession (UNIPROT accession numbers [71]), protein description, gene names, protein classes, and diseases. The first protein belongs to the categorized epidermal protein markers (category II).

accession (UNIPROT)	protein description	gene names	protein classes
Q9UBG3 (II)	Cornulin	CRNN	– Predicted intracellular proteins
P09455	Retinol-binding protein 1	RBP1	– Predicted intracellular proteins
Q96P15	Serpin B11	SERPINB11	– Plasma proteins – Predicted intracellular proteins
Q9UNK0	Syntaxin-8	STX8	– Predicted intracellular proteins – Predicted membrane proteins
O15118	NPC intracellular cholesterol transporter 1	NPC1	– Disease related genes – Potential drug targets – Predicted membrane proteins – Transporters
Q15291	Retinoblastoma-binding protein 5	RBBP5	– Predicted intracellular proteins

4.4. PIRL ablation and homogenization of skin biopsies layer-by-layer

4.4.1. Parameter optimization of PIRL

For layer-by-layer ablation of skin tissues using the PIRL-DIVE method, the PIRL parameters needed to be optimized to achieve the ablation of the thinnest cell layer as possible. Therefore, several experiments were set up to define the optimal laser energy per pulse. All experiments for optimizing of laser parameters were performed in the first chamber generation and the homogenates were collected and condensed into the first generation of cooling trap placed into liquid nitrogen as shown in chapter 3.2.2.1 in figure 10.

4.4.1.1. Experiment PIRL optimization I:

A breast skin tissue was ablated by PIRL at its maximum laser power with 420 mW. The laser beam was aligned from top of the tissue and was guided manually from top to bottom and from bottom to the top row by row as described in chapter 3.2.3.1. The scan duration was about 30 seconds. The aerosol was collected in the cooling trap. This process was repeated twice on the same ablated area and the plumes were collected each time in a new trap. The collected plumes were digested and analyzed by tandem mass spectrometry. Approximately 1600 proteins were identified averagely in the ablated layers. The H&E staining visualizes the ablation depth in figure 41. The layer-by-layer ablation was failed. With the maximum laser energy, the skin tissue was ablated through the basement membrane and papillary dermis into the reticular dermis with an ablation depth of 300 μm . Aside from that, a ridge pattern was observed on the surface of ablated skin tissue because of the operating parameters of laser spots. The spot diameter and the grid spacing were selected arbitrarily here. The results of microscopy imaging showed that the spot diameter and the grid spacing parameters ought to be selected as small as possible to achieve an arrangement of spots with a view to avoiding the formation of ridge pattern. Further, the laser power was adjusted at its maximum, which is for a total ablation of tissue eminently suitable but too high for cell layer ablation by a layer-by-layer approach.

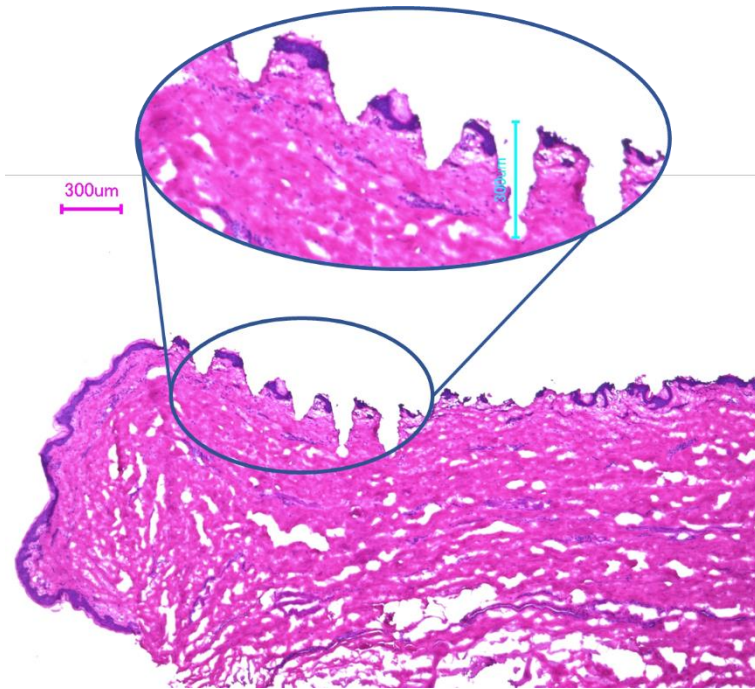


Figure 41: Image of an H&E-stained section of ablated skin tissue using PIRL-DIVE with the maximum laser power with 420 mW. While the layer-by-layer ablation (three times) the laser beam went through the papillary dermis and attained occasionally the reticular dermis, whereby the goal was to ablate the epidermal domain. The zoom-in image shows that the laser beam remained a ridge structure.

4.4.1.2. Experiment PIRL optimization II:

Due to the results from *experiment PIRL optimization I*, a second optimization attempt was implemented with 6 different laser pulse energies from the maximum possible energy down to the minimum energy using two tissues. The experimental set-up with six different laser energies was performed firstly for a normal thick skin tissue and secondly for a 200 µm dermatome skin tissue. The laser energies were adjusted from the ~390 µJ per pulse to ~140 µJ per pulse to estimate the optimal laser energy to achieve an ablation depth as thin as possible. The ablation aerosols were collected in the cooling trap. The condensates were digested and analyzed by tandem mass spectrometry. The depth of ablated tissues was measured by confocal laser scanning microscope using either the fluorescent dyeing method – representing the nuclei of the cells – or collagen autofluorescence. The mass spectrometric results for both tissues are shown in figure 42 in a bar chart diagram. The laser energy was adjusted from maximum to minimum: (1) 387 µJ/pulse; (2) 334 µJ/pulse; (3) 291 µJ/pulse; (4) 253 µJ/pulse; (5) 195 µJ/pulse; (6) 142 µJ/pulse. The ratio of the number of identified proteins in both biopsies was largely similar except for one outlier at 253 µJ/pulse on the 200 µm dermatome skin tissue.

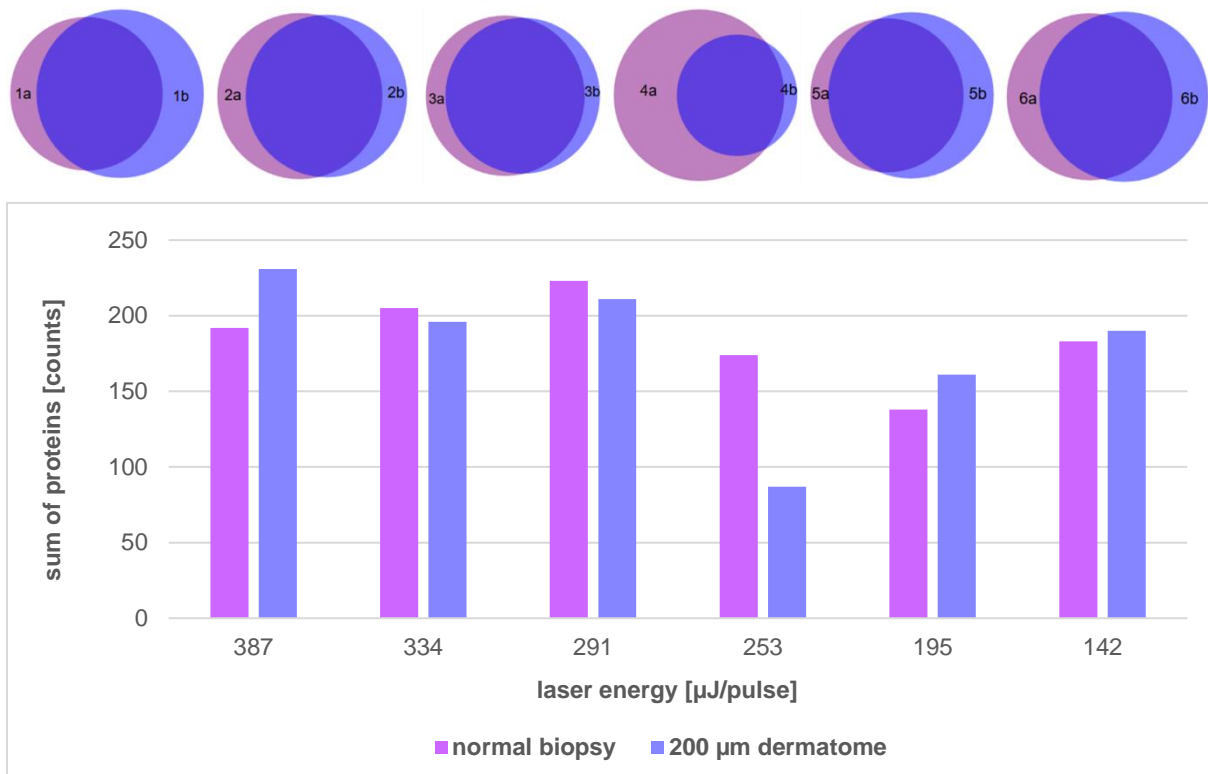


Figure 42: Statistical analysis of the LC-MS/MS data from tryptic digested peptides from the normal biopsy and the 200 µm dermatome biopsy ablated using the PIRL-DIVE technique with 6 different laser energies. *Top:* The six Venn diagrams visualize the overlap of all identified proteins (unique peptides ≥ 1) in the normal biopsy (a) as well as in 200 µm dermatome biopsy (b). The six adjusted laser energies amounted to (1) 387 µJ/pulse; (2) 334 µJ/pulse; (3) 291 µJ/pulse; (4) 253 µJ/pulse; (5) 195 µJ/pulse; (6) 142 µJ/pulse. *Bottom:* The bar chart diagram shows the total number of identified proteins in normal (purple) and 200 µm dermatome (blue) biopsies.

The ablation depth of the normal skin biopsy was determined by confocal laser scanning microscope using collagen autofluorescence, for each adjusted laser pulse energy. The confocal laser scanning microscopy using fluorescence excitation and emission applied, in this case, the architecture of collagen fibers. The autofluorescence excitation and emission spectra of collagen fibers lead to 3D imaging of collagen-rich ECM in skin tissues. During PIRL ablation, the ECM of dermis could be reached when the tissue was ablated long enough or when the laser energy was set high enough. The deeper the PIRL ablation is, the more colorful the fluorescence image of collagen is. The comparison of the ablated area and non-ablated area allowed for the determination of depth. The laser setting parameter from the highest to the lowest energy yielded the desired effect. From the maximum to the minimum adjusted laser pulse energy levels, a decreasing slope of determined ablation depths was observed. In Figure 43, all six confocal autofluorescence microscopy images for the six different adjusted laser setting parameters are displayed from the highest laser energy (387 µJ/pulse) to the lowest (142 µJ/pulse).

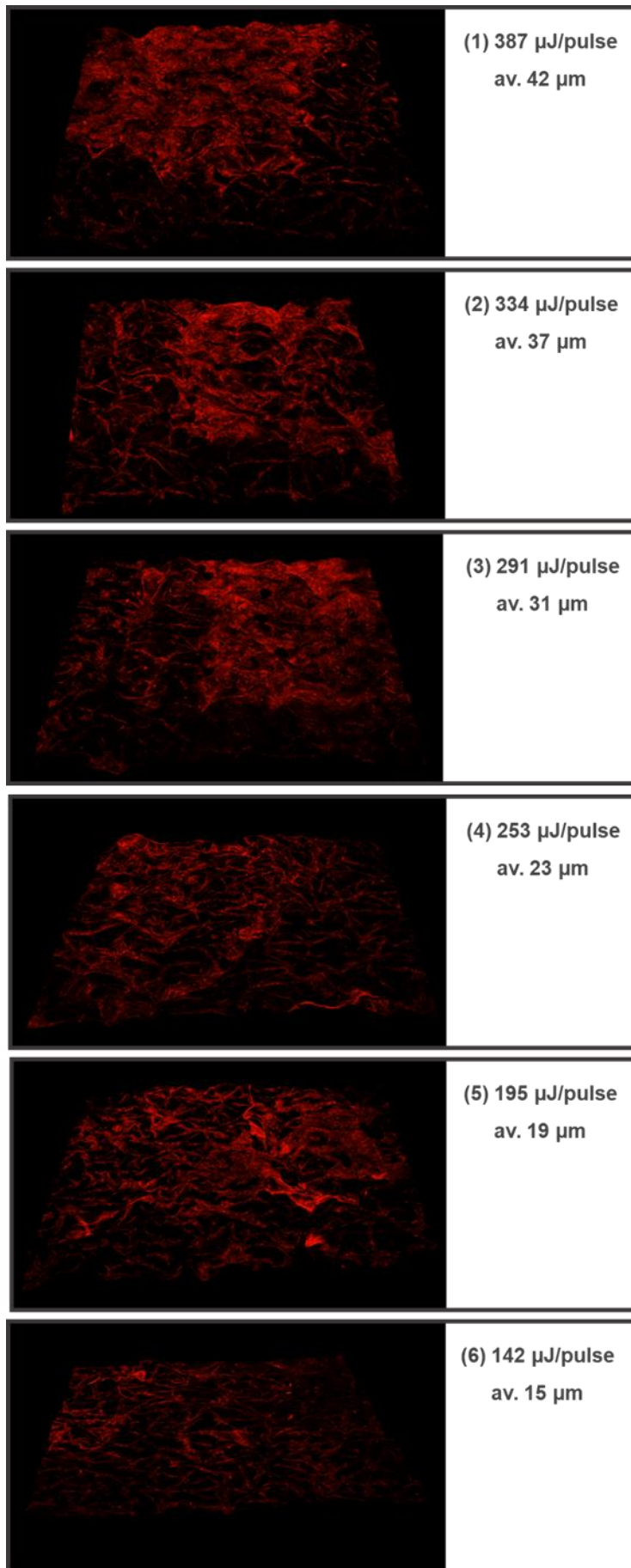


Figure 43: Confocal laser scanning microscopy images using collagen autofluorescence of ablated normal skin biopsy to optimize the PIRL setting parameters. The six microscopy images represent the remained structure on skin after PIRL ablation using six different laser energy levels: (1) 387 $\mu\text{J}/\text{pulse}$; (2) 334 $\mu\text{J}/\text{pulse}$; (3) 291 $\mu\text{J}/\text{pulse}$; (4) 253 $\mu\text{J}/\text{pulse}$; (5) 195 $\mu\text{J}/\text{pulse}$; (6) 142 $\mu\text{J}/\text{pulse}$. The 3D images of collagen-rich skin tissues enable the determination of the ablation depth in reference to the non-ablated areas. With the maximum laser energy (387 $\mu\text{J}/\text{pulse}$, the maximum ablation depth was obtained (at average 42 μm) and with the minimum (142 $\mu\text{J}/\text{pulse}$) the minimum ablation depth (at average 15 μm).

The six microscopy images represent the skin surface structure on skin after PIRL ablation using six different laser energy levels: (1) 387 $\mu\text{J}/\text{pulse}$; (2) 334 $\mu\text{J}/\text{pulse}$; (3) 291 $\mu\text{J}/\text{pulse}$; (4) 253 $\mu\text{J}/\text{pulse}$; (5) 195 $\mu\text{J}/\text{pulse}$; (6) 142 $\mu\text{J}/\text{pulse}$. The 3D images of collagen-rich skin tissues enable the determination of the ablation depth in reference to the non-ablated areas. The intense red color of collagen fibers in the first sample illustrates reaching of the dermis area by strong ablating using high laser energy. From the first sample ablated with the highest laser energy up to the last sample ablated with the lowest laser energy, the observable red color of fibers becomes weaker. Therefore, the lower the laser energy the thinner the ablated cell layers. With the maximum laser energy (387 $\mu\text{J}/\text{pulse}$, the maximum ablation depth was obtained (at average 42 μm) and with the minimum (142 $\mu\text{J}/\text{pulse}$) the minimum ablation depth (at average 15 μm). In figure 44 the linear correlation between the decreasing laser energy and the declining PIRL ablation depth is illustrated in a bar chart diagram.

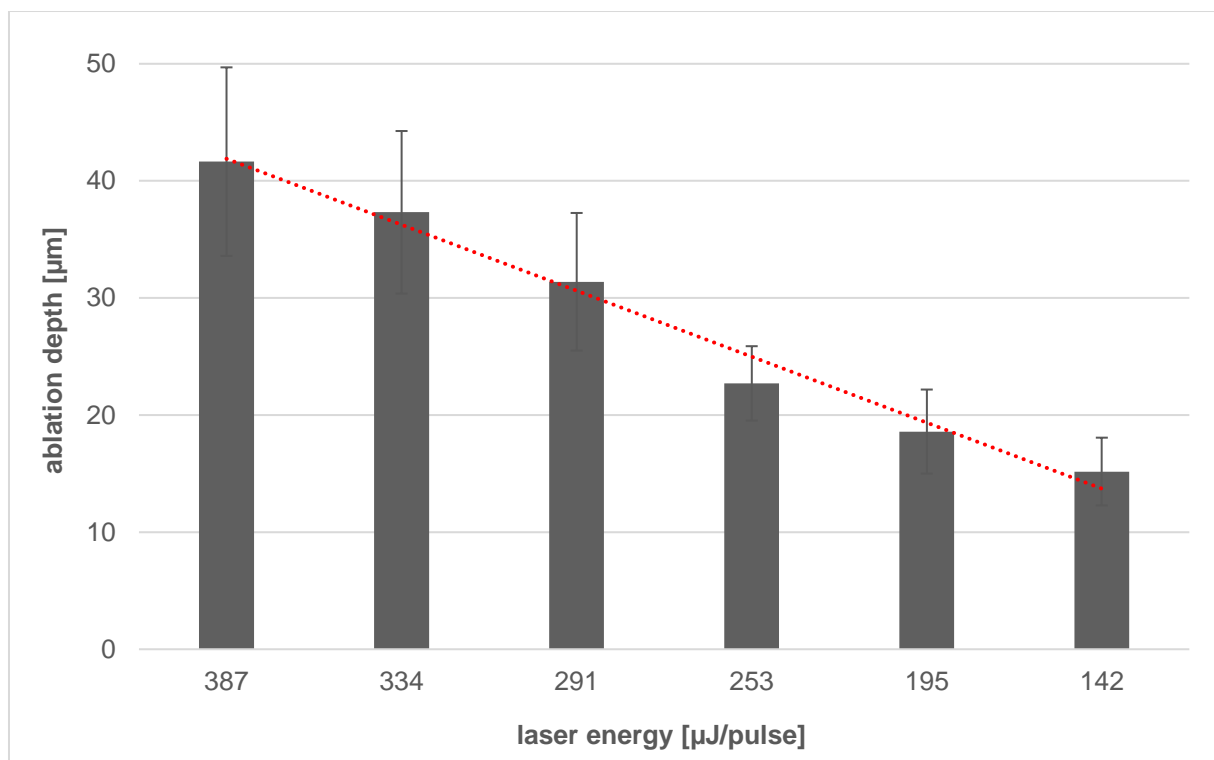


Figure 44: Linear correlation of laser energy setting parameter and the determined PIRL ablation depth with the aid of confocal laser scanning microscopy using collagen autofluorescence measurement. The six adjusted laser energies amounted to (1) 387 $\mu\text{J}/\text{pulse}$; (2) 334 $\mu\text{J}/\text{pulse}$; (3) 291 $\mu\text{J}/\text{pulse}$; (4) 253 $\mu\text{J}/\text{pulse}$; (5) 195 $\mu\text{J}/\text{pulse}$; (6) 142 $\mu\text{J}/\text{pulse}$. The bar chart shows the ablation depth in μm for each ablated area of normal skin biopsy with a certain laser pulse energy, additionally the corresponded standard deviation within the five measured spots of each sample and the dot line is the trendline of decreasing ablation depths due to the decreasing laser energy levels.

The ablation depth for the 200 μm dermatome skin biopsy was measured by confocal laser scanning microscopy using fluorescent dyeing of cell nuclei. The microscopy images are shown in the supplement (S.8). The determined depths deviate from those determined in the normal biopsy. For the 253 $\mu\text{J}/\text{pulse}$ laser energy, the edge of the ablated area could not be identified. Due to that, a precise depth measurement was not possible. This could be traced back to a failed ablation. From the mass spectrometry result, the number of identified proteins in this samples (87 proteins counted) was much less than in the normal biopsy (174 proteins counted) for the same laser energy setting. Besides the failed ablation, the measurement of ablation depth in other ablated areas was just as complicated. These difficulties were probably because of the morpho-differentiation between the ablated area and the non-ablated area. The exterior morphology of the dermatome biopsy was potentially changed by mechanical forces and this led to imprecise depth measurement. The linear correlation of the laser energy setting parameters and the determined PIRL ablation depths with the aid of confocal laser scanning microscopy using fluorescent dyeing for the 200 μm dermatome biopsy is displayed in a bar chart in the supplement (S.7) as well.

4.4.1.3. Experiment PIRL optimization III:

Relating to the results of *experiment PIRL optimization II* and showed that the last two adjusted laser energies yielded the thinnest ablation depths. Therefrom, a new experiment was set by defining three laser energies closed to both values. The three pulse energies were adjusted between $\sim 190 \mu\text{J}$ to $\sim 140 \mu\text{J}$ and the skin (61w, a 61 years old skin biopsy) were ablated twice with each selected laser energy level. The ablation aerosol was collected in the cooling trap. The condensates were digested and analyzed by tandem mass spectrometry. The depth of ablated tissues was measured by confocal laser scanning microscope using the fluorescent dyeing method as described above.

The data analysis of mass spectrometry resulted in an irregular number of identified proteins as seen in table 12. In the sample 1a (ablated with a laser energy of 144 $\mu\text{J}/\text{pulse}$) 360 proteins (unique peptides ≥ 1) could be identified whereby 53 of these proteins are protein markers of the epidermis and only 4 dermal protein markers were identified. The achieved ablation depth was 19 μm on average. In the sample 1b (ablated with a laser energy of 144 $\mu\text{J}/\text{pulse}$) only 57 proteins could be identified. Based on the low protein number, it is assumed that during the collection of the ablation plume, an error occurred. It is suspected to that the tube connecting the chamber to the cooling trap was frozen, which is easily noticeable by an abrupt decrease in pressure. But in virtue of an ultrafast ablation time within 10 sec for a small ablation area of 7x7 mm it was not possible to observe the pressure change during the experiment. This could

be observed only after the mass spectrometry results has been analyzed. In the samples 2a and 2b (ablated with a laser energy of 166 $\mu\text{J}/\text{pulse}$), 183 and 227 proteins were identified whereby respectively 22 and 41 protein markers of epidermis were founded and only 1 and 2 protein markers of the dermis. An accurate determination of ablation depth was prevented for the sample 2b due to many outliers. For the 2a the ablation resulted in 17 μm deep at average. That implies that the linear correlation to the lowest laser energy was interrupted here. In the samples 3a and 3b (ablated with a laser energy level of 184 $\mu\text{J}/\text{pulse}$), 795 and 477 proteins were identified in total. 194 and 111 were the number of identified epidermis protein markers in both samples respectively. Furthermore, only 2 and 3 proteins belonged to dermis protein markers. The determined ablation depth for sample 3a was about 25 μm and for sample 3b a depth of 23 μm was achieved averagely.

Table 12: Experiment PIRL parameter optimization III: three different laser energies were selected (1) 144 $\mu\text{J}/\text{pulse}$; (2) 166 $\mu\text{J}/\text{pulse}$; (3) 184 $\mu\text{J}/\text{pulse}$ and the ablation was performed twice for each pulse energy. The number of identified proteins (unique peptides ≥ 1), an average of ablation depth in μm and the corresponded standard deviation (five measured spots) for each sample are listed.

#	laser energy [$\mu\text{J}/\text{pulse}$]	protein IDs	average of ablation depth [μm]	standard deviation of ablation depth
1a	144	360	19.1	7.8
1b	144	57	15.8	3.7
2a	166	183	17.1	4.9
2b	166	227	many outliers	---
3a	184	795	25.3	7.2
3b	184	477	23.0	6.6

The inaccurate determination could be due to two issues. Firstly, it is suspected that the fluorescent protein staining ended up in depth determination with a great error factor between the selected spots. By comparison of the confocal microscopy results in *experiment PIRL parameter optimization II*, it is apparent that the collagen autofluorescence measuring in figure 44 showed a linear correlation as expected while for the same laser setting parameters the confocal laser scanning microscopy images using fluorescent dyeing for the 200 μm dermatome biopsy showed great error rates and a non-linear correlation between the laser energy levels and the determined ablation depths (see figure in supplement S.8). The same

irregularity of the ablation depth determining was observed for the *experiment PIRL parameter optimization III* as well. Arising thereby that the choice of suitable microscopy method affects the 3D visualization of tissues (figure 45). The blue color in the images for skin parts 1a and 1b ablated with 144 $\mu\text{J}/\text{pulse}$ shows an almost even area. The depth measurement within the five selected spots was 19 μm averagely. Distinguishing between the ablated and non-ablated areas for this adjusted energy was more complicated than the previous experiment. The depth measurement of 2a part of the skin biopsy ablated with 166 $\mu\text{J}/\text{pulse}$ laser energy yielded in 17 μm whereby the 2b part was not measurable at all. For the 184 μJ laser pulse energy in the 3a and 3b parts of skin, a ridge structure was formed which caused by the selected gap between laser spots. By virtue of this knowledge, a new parameter had to be adjusted for the layer-by-layer ablation to mind a gap between the spots and induce an even ablation.

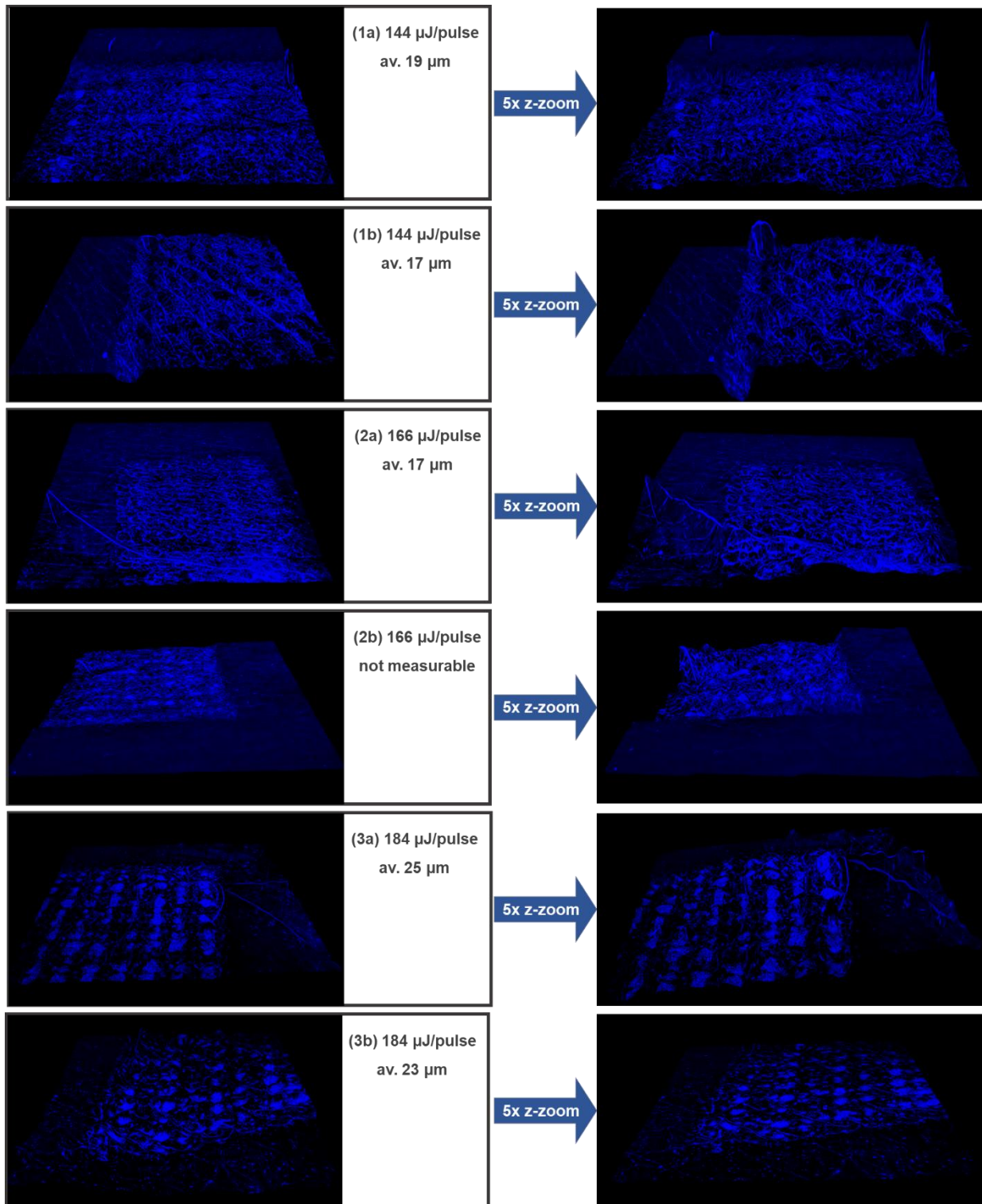


Figure 45: Confocal laser scanning microscopy images using Hoechst 33342 fluorescence - representing the nuclei of the cells - of ablated skin tissue to optimize the PIRL setting parameters. The six microscopy images represent the remained structure on the skin after PIRL ablation using three different laser energies: (1) 144 $\mu\text{J/pulse}$; (2) 166 $\mu\text{J/pulse}$; (3) 184 $\mu\text{J/pulse}$. Each energy set-up was repeated twice (1a & 1b; 2a & 2b; 3a & 3b). *Left:* microscopy images of ablated areas; *right:* microscopy images of ablated areas with the five-fold zoom in the Z-axial for realizing the 3D representation.

Apart from the fact that the depth determination with the aid of confocal laser scanning microscopy using fluorescence dye featured as questionable for skin samples compared to collagen autofluorescence, the age of the tissue could be the reason for imprecise determination of depth too. The older the tissue is, the thinner the epidermal layer [1]. Furthermore, the collagen fibers break during the aging process, thus wrinkles appear. These aging phenomena impeded the layer-by-layer tissue ablation using the PIRL-DIVE technique, which is already complicated by the naturally-occurring rete ridges structure of skin tissue.

4.4.1.4. Experiment PIRL optimization IV:

It follows from the foregoing *experiment PIRL optimization III*. The experiment ought to be repeated with the same range of laser energies but the different age of the tissues. Therefore, from old to young tissues were chosen randomly. Laser energies between ~180 to ~140 $\mu\text{J}/\text{pulse}$ were adjusted for ablation of two tissues of different donors (different ages: 23w, 33w, 56w and 61w). The ablation aerosol was collected in the cooling trap. The homogenate was digested and analyzed by tandem mass spectrometry. The efficiency of tissue ablation using PIRL-DIVE technique was verified by microscopy of H&E-stained tissue sections.

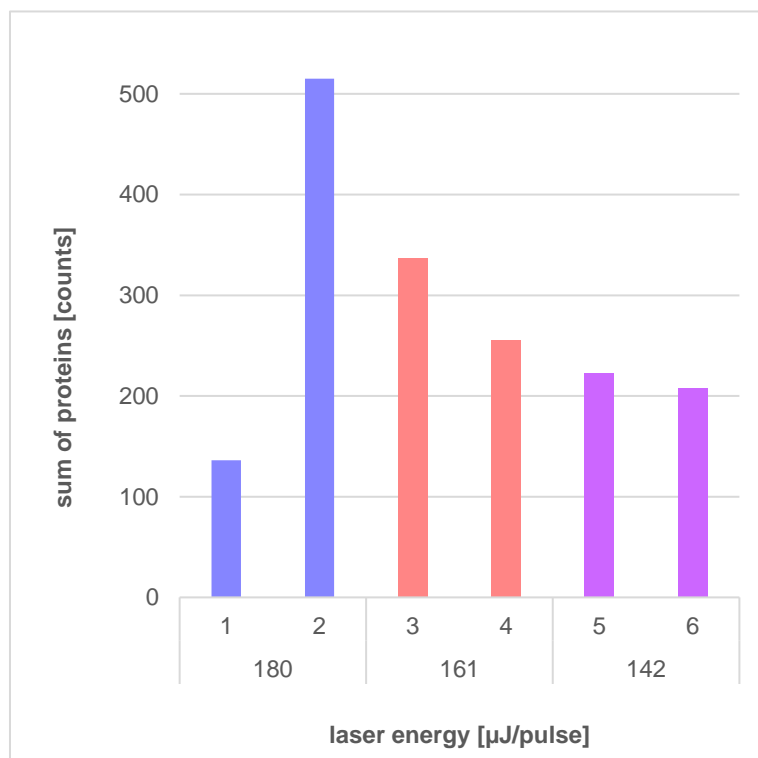


Figure 46: Statistical analysis of the LC-MS/MS data from tryptic digested peptides from six different tissues of four donors of different ages. The bar chart diagram shows the total number of identified proteins (unique peptides ≥ 1) in each ablated sample using the PIRL-DIVE technique. (sample 1: 56w, sample 2: 61w, both ablated with a laser energy of 180 $\mu\text{J}/\text{pulse}$; sample 3: 23w, sample 4: 61w, both ablated with a laser energy of 161 $\mu\text{J}/\text{pulse}$; sample 5: 61w and sample 6: 33w, both ablated with a laser energy of 142 $\mu\text{J}/\text{pulse}$).

The data analysis of tandem mass spectrometry – figured as a bar chart in figure 46 – indicated that with the highest laser energy, a deeper ablation was achieved due to the high identified number of proteins with more than 500 (exempted the sample one with 136 proteins). The high number of identified proteins was observed in the last experiment as well (listed in table 12). Hence, the second sample with the considerable low number of identified proteins ensued as a failure by collecting of the ablation plume. It can be assumed that, the tubing system to the trap was frozen again by liquid nitrogen (occurred in *experiment PIRL optimization III*) and caused the pressure failure within the chamber and as a consequence induced a turbulent air flow in the chamber. As explained before, the ablation took less than 10 seconds that an observation of low pressure in the pump detector in so short time was complicated. In addition to fast ablation time and undetectable pressure failure, it is presumed that, the ablation plume could be condensed into the long tubes before catching the cooling trap, without freezing and blocking the tube system. Continuing with the data, using a laser energy level of 161 $\mu\text{J}/\text{pulse}$ promoted the expectation that, by decreasing the laser energy fewer cell layers can be ablated and a lower number of proteins can be identified accordingly. In sample 3 about 337 and in sample 4 about 255 proteins were identified in total. A decrease in number of proteins was observed for sample 5 with 223 and sample 6 with 208, which were ablated with a PIRL laser energy of 142 $\mu\text{J}/\text{pulse}$. The sample 1 (with the low identified protein number) excluded, a linear correlation between the descending laser energies and decreasing in the protein numbers was noticeable as similar to the decreasing ablation depth.

By considering the images of H&E stained tissue sections the age-related thinning of epidermal layers was observed the older the tissues were as stated in literature. The skin aging makes itself noticeable by dermis aging as well as epidermis aging induced by reduction and fragmentation of extracellular collagen matrix, the rate of keratinocytes circulation and the change of protein composition of cornified envelope which is responsible for the barrier function [1]. In figure 47 the image of H&E-stained section of ablated skin tissue (56w) with the laser energy 180 $\mu\text{J}/\text{pulse}$ is shown. The zoom-in image illustrates strikingly that the laser irradiations went through epidermal cell layers and the basement membrane partly and reached the papillary dermis. In figure 48, the H&E-image of ablated skin tissue (23w) with the laser energy 161 $\mu\text{J}/\text{pulse}$ is shown, the left zoom-in image visualizes the passage from the non-ablated area with a 100 μm epidermis deepness to the ablated area with 30 μm remaining epidermis. The right zoom-in image exemplified the problem of the naturally-occurring rete ridge structure of the skin. The different skin depths within the same domain (the skin rete ridge pattern) affected the layer-by-layer ablation as shown in figure 48. In figure 49 the H&E- the image of ablated skin tissue (61w) with the laser energy 144 $\mu\text{J}/\text{pulse}$ is shown. The zoom-in image visualizes the ablated areas of the tissue in outermost layers of the epidermis as scheduled.

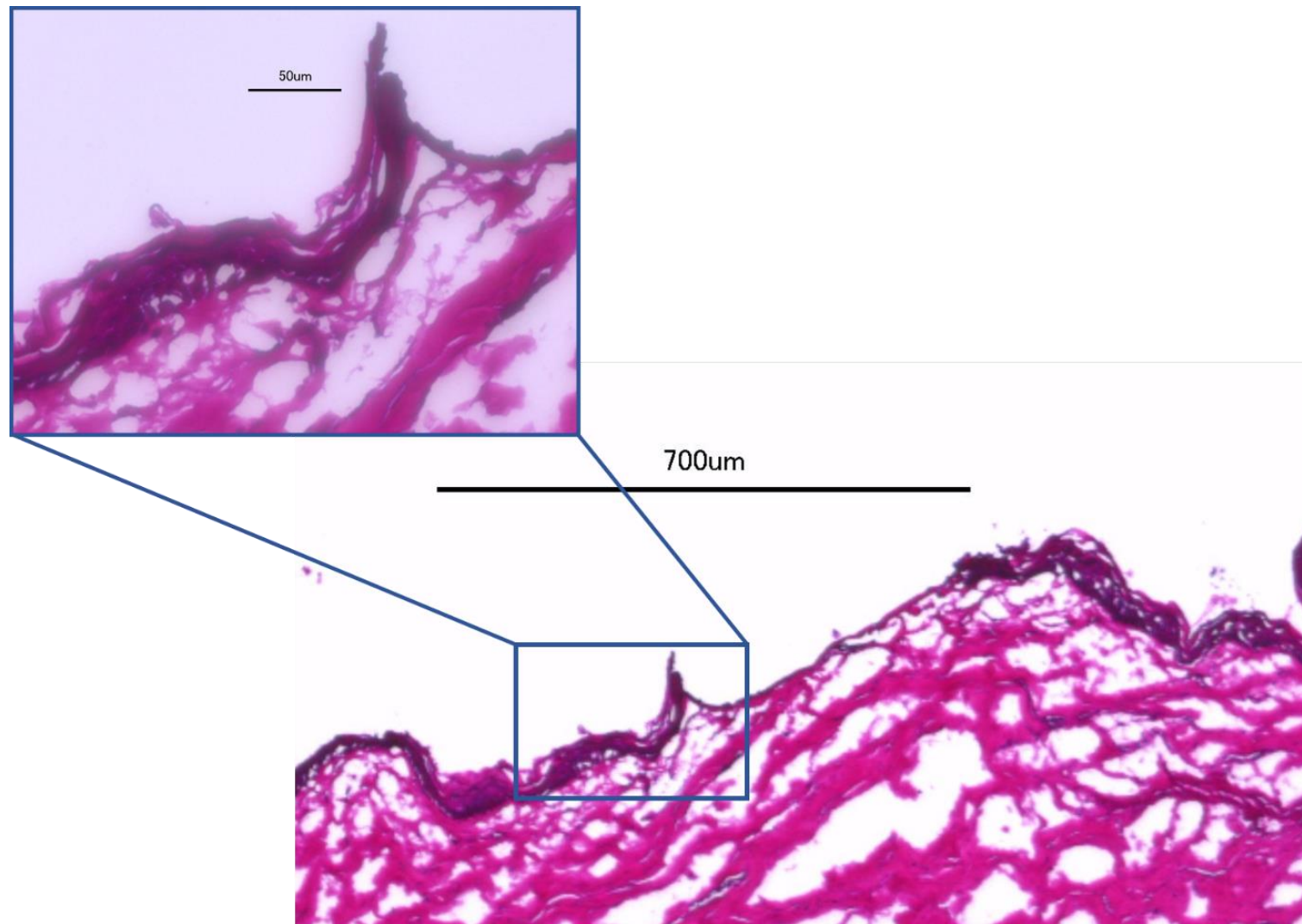


Figure 47: Image of H&E-stained section of ablated skin tissue (56w) using PIRL-DIVE with the laser energy 180 µJ/pulse. The zoom-in image shows the ablated area of the tissue through the stratum basale to the papillary dermis.

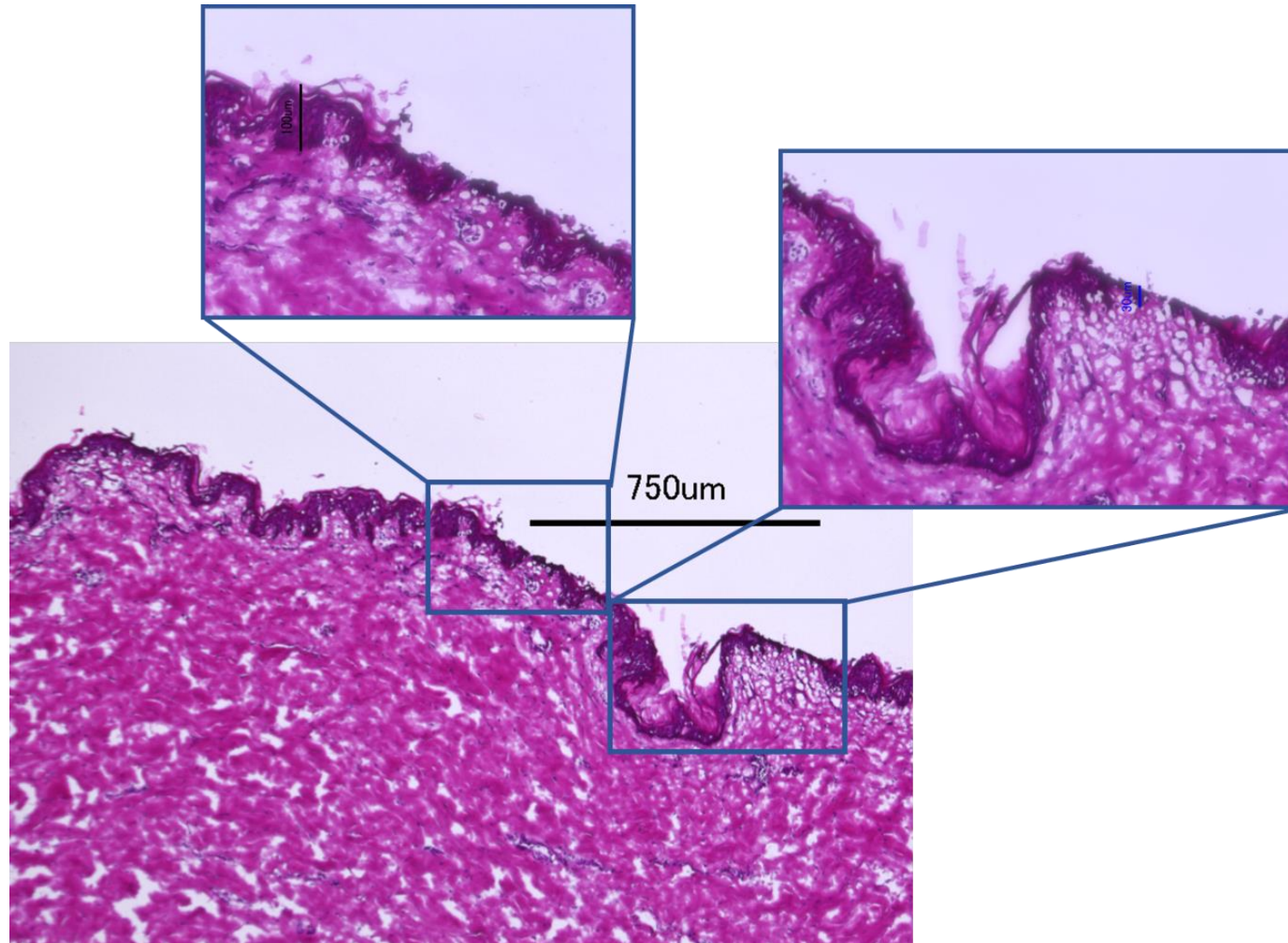


Figure 48: Image of H&E-stained section of ablated skin tissue (23w) using PIRL-DIVE with the laser energy $161 \mu\text{J}/\text{pulse}$. The zoom-in images visualize the ablated areas of the tissue up to the basement membrane (in some domains). The epithelial rete ridge structure of the skin is shown in both enlarged images.

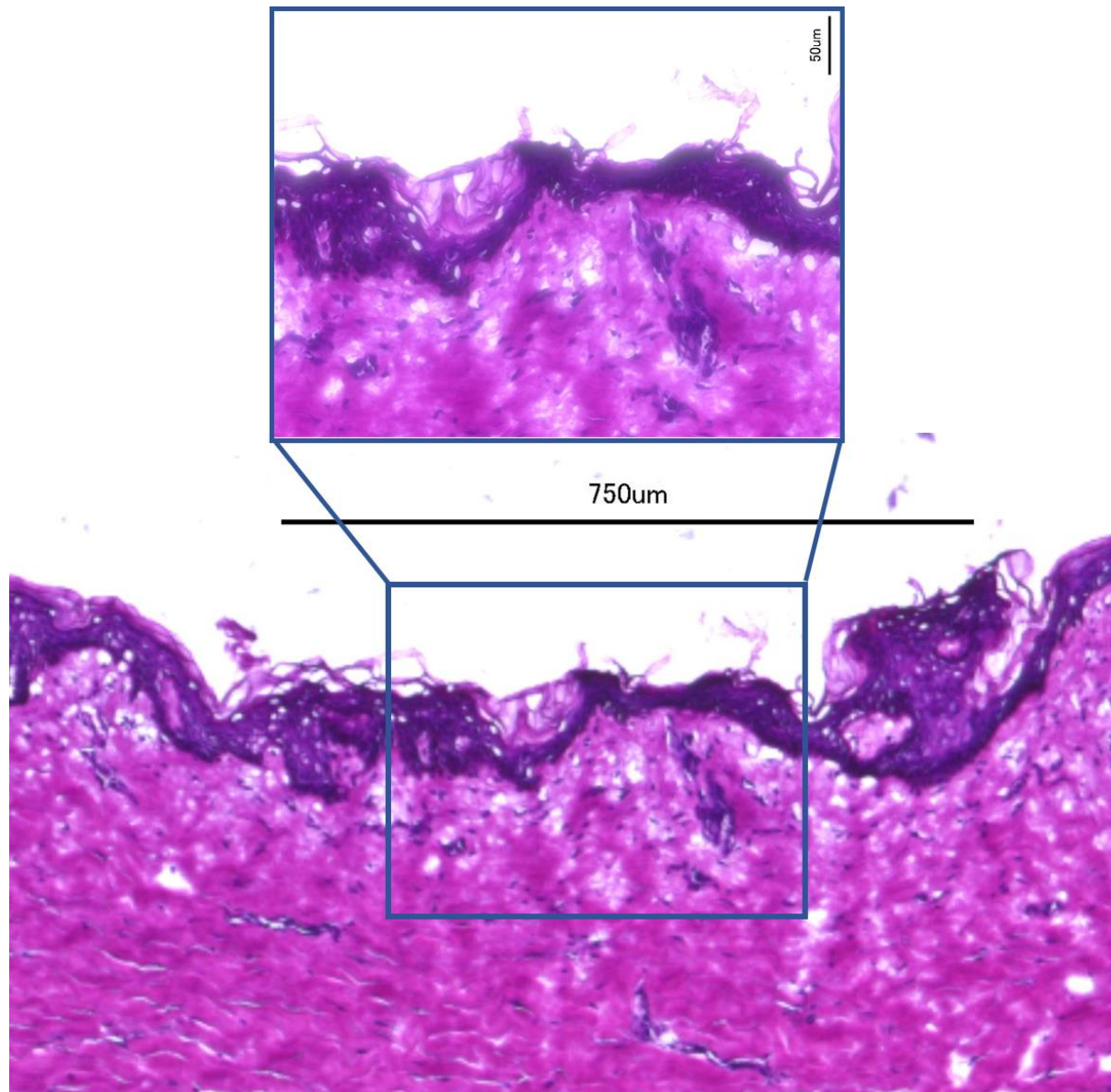


Figure 49: Image of H&E-stained section of ablated skin tissue (61w) using PIRL-DIVE with the laser energy 144 μJ/pulse. The zoom-in image visualizes the ablated areas of the tissue in outermost layers of the epidermis.

4.4.2. Layer-by-layer ablation of skin tissues with the optimized laser parameters

After optimization of laser parameters, the layer-by-layer ablation of skin tissues proceeded.

4.4.2.1. Experiment PIRL layer-by-layer I:

With the laser energy 140 $\mu\text{J}/\text{pulse}$, which was the optimized laser energy, the tissue underwent two or three ablations of cell layers with an ablation depth of approximately 15 μm for each laser scan through the selected area within 11 seconds. The spot diameter was 145 μm and the grid spacing 10 μm . The experiment was executed for two biological breast biopsies from different donors and two and three technical replicates. The homogenates included in the ablation aerosol, were collected in the cooling trap. The proteins were digested and finally analyzed by tandem mass spectrometry. In table 13, the samples are listed from 1 to 5 (termed as exp-1 up to exp-5). The samples 1 and 2 originated from one donor with age 58 and the last three came from a second donor with age 66. In the first ablated layer of the first biological sample for exp-1 and -2, about 75 and 98 proteins were identified which resulted in 86 proteins on average (for the first biological sample 58w). For the second layer, 29 and 102 proteins were identified. The low protein number in exp-2 achieved during the 2nd ablation bears resemblance to the protein number in control (21 proteins). In other words, the homogenate collection failed contingently as a result of the tube freezing or premature condensation in the tube or leak in the chamber. All can affect the aerodynamics in the system as explained before. In the first ablated layer of the second biological sample for exp-3, -4 and -5, 351, 157 and 110 proteins were identified respectively which resulted in 206 proteins on average. In the second layer 285, 212 and 134 proteins were counted (averagely 210 proteins). Three samples (exp-2, -3 and -5) were ablated for the third time and the protein identification resulted in 123 proteins in the exp-2, 243 proteins in the exp-3 and again 123 proteins in the exp-5 (at average 163 proteins). In the control, 21 proteins were identified as contamination, whereby 16 of these proteins were identified in all five samples too. These human proteins cannot be excluded as contamination because they are proteins originally from skin (potentially from the shedding of dead corneocytes cells). The numbers of detected unique peptides and PSMs for these 16 proteins are higher in all five samples than the numbers in the control sample. They are mainly cytoskeletal Keratin proteins type II (Keratin 1, 2 epidermal, 2 oral, 4, 5, 6a, 6b, 6c, 7, 8 and 80) and type I cytoskeletal Keratin 10 protein.

Table 13: Proteins identified in the first Layer-by-layer approach using the PIRL-DIVE method, with its optimized parameters. In total five samples were ablated. Some underwent two ablations and some three ablations. The number of identified proteins for 1st, 2nd, and 3rd layers are listed. The mean value plus the corresponded standard deviation is carried out for each biological sample and all together as well.

samples	number of proteins in 1st layer	number of proteins in 2nd layer	number of proteins in 3rd layer
exp - 1	75	29	---
exp - 2	98	102	123
mean (58w)	86	66	---
standard deviation	11.5	36.5	---
exp - 3	351	285	243
exp - 4	157	212	---
exp - 5	110	134	123
mean (66w)	206	210	183
standard deviation	104.3	61.7	60.0
mean (all)	158	152	163
standard deviation (all)	100.0	88.6	56.6

When comparing the number of identified proteins in each layer it becomes clear immediately that there is no correlation between either the identified protein numbers or the ablated cell layers (1st, 2nd, and 3rd layers) or even within the same ablated layer in different biological samples. This observation can be traced back to the irregular airflow in the chamber affected by blocked tubes and trap or a premature condensation or the leaking chamber or leaking lid of the cooling trap as set out. Besides, the dilution factor due to condensed water in the air humidity played a major role as well (a molecular sieve was later built to reduce the air humidity). A further conjecture is the naturally existing inter-individual variation in the proteome. In the first two samples (originating from a 58w donor), the number of identified proteins in both

1st and 2nd ablated layers were much lower than in the samples 3 to 5 (originating from a 66w). Attention should be paid to the fact that, ablation of skin goes through the stratum corneum. The stratum corneum contains a layer of unique surface lipids of fatty acids, cholesterol, and ceramides produced by keratinocytes which makes up 30 to 35% of the entire skin lipids [72]. The molecular structures of these three lipid classes are shown in figure 50.

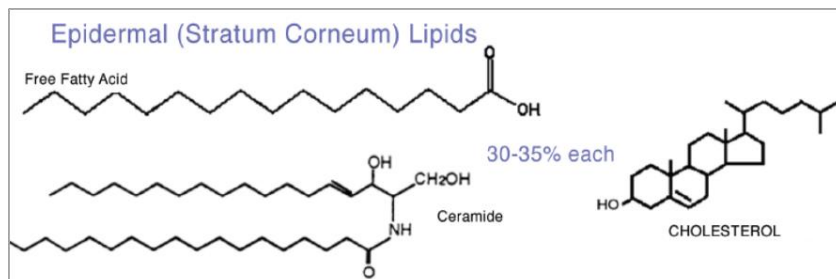


Figure 50: Molecular structures of three lipid classes in stratum corneum. These three lipid classes: free fatty acids, ceramides, and cholesterol make up 30–35% of lipid content in skin [72].

The high lipid content of the skin makes the proteomics of skin tissue challenging [3]. It is supposed that the lipid content from an individual to the other varies. Due to the presence of these lipids, the signals of peptides are suppressed during MS-measurement. Additionally, there is no background information about biopsy donors and their health conditions. Diseases, like neurodermatitis, psoriasis, ichthyosis, diabetes mellitus, hormone disorders etc., and also factors like nutrition and environmental exposures are responsible for lipid housekeeping. The higher the lipid content the more complicated the proteome analysis.

Additionally, the variation within the technical replicates is irregularly high as well. This indicates perhaps that the manual tissue ablation and a simultaneously switching-on and -off of the vacuum pump did not take place congruently.

All these suspected points –

- a turbulent airflow in the chamber, caused by blocked tubes through freezing or premature condensation in the tubes,
- leaking chamber or leaking lid of cooling trap vial,
- dilution factor as a result of air humidity,
- manual performance of laser and vacuum pump (simultaneously)
- the biological aspect dependent on biopsy origin (age, lipid housekeeping, diseases and environmental exposures that the skin biopsy was set out)

explain the irregularity in the achieved number of proteins identified in the ablated layers. The mean value of all three ablated layers is demonstrated in a bar chart in figure 51 with the corresponded standard deviation.

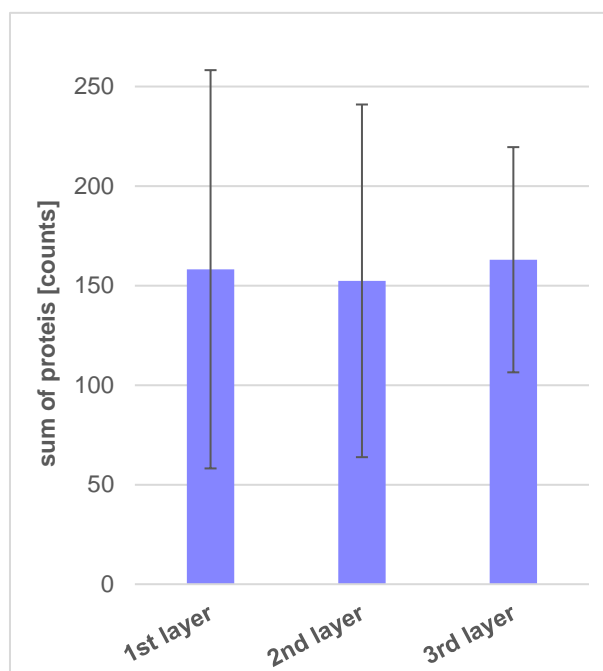


Figure 51: Statistical analysis of the LC-MS/MS data from tryptic digested peptides of layer-by-layer ablated samples using PIRL-DIVE. The bar chart shows the mean and corresponded standard deviation of achieved proteins for 1st and 2nd ablated layers of five tissues (replicates n=5) and 3rd ablated layer of three tissues (replicates n=3). The samples originated from 58 and 66w donors from breast reduction surgeries (biological replicates n=2).

Back to the mass spectrometry data, in the 1st layer 158 proteins were identified on average with a standard deviation of 100.0 within the five replicates. Comparing the results to the epidermis and dermis protein marker libraries, it yielded in 20 epidermis and 3 dermis protein markers whereby most of them were detected in exp-3. The GO analysis in STRING database [73] against the whole human genome describes 13 proteins of these 20 proteins that were extracellular exosomes (GO0070062) with respect to significantly enriched GO-term of cellular component aspect with FDR rate of 3.6×10^{-5} . The functional enrichment of these referred as protein markers are shown in a network in figure 52 where each node that represents all the proteins produced by a single protein-coding gene. In other words, all proteoforms induced by splicing or post-translational modifications which were produced by a protein-coding gene are collapsed together. The lines (with are different in thickness which indicating the strength of data support) illustrate the protein-protein associations e.g. associated in the same pathway or indicates protein-protein interaction or even co-mentioned in publications. For example, looking at the network in figure 51, histone H1.1 (HIST1H1A) and histone H1.5 (HIST1H1B) are associated with curated biological pathways. Dermokine (DMKN) and keratinocyte differentiation-associated protein (KRTDP) were co-mentioned in several PUBMED [74] Abstracts. Furthermore, proteolipid protein 2 (colonic epithelium-enriched) (PLP2) and NudC domain containing 2 (NUDCD2) curated protein-protein interaction based on succeeding abstract with PMID: 17234964.

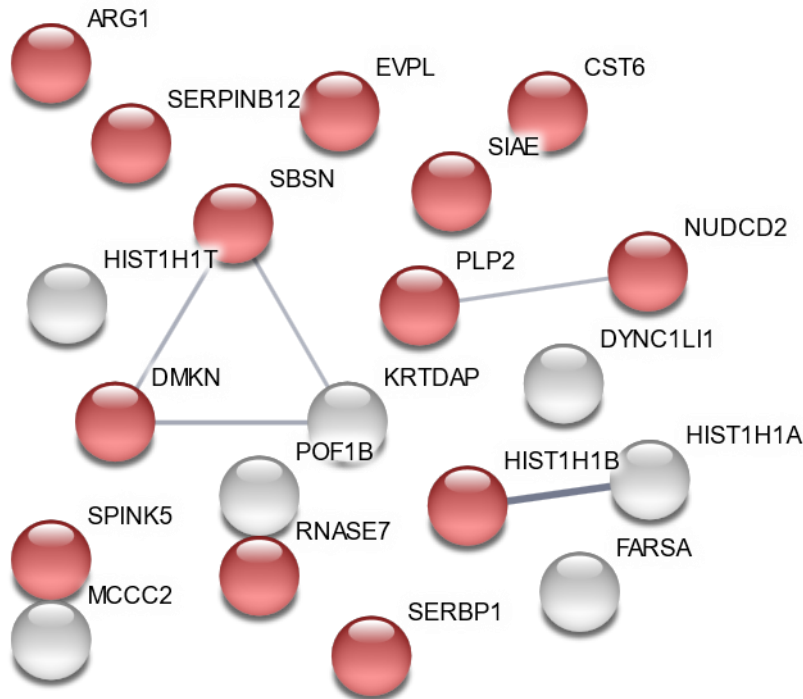


Figure 52: Gene ontology (GO) information of the 20 epidermal protein markers in 1st ablated layers. The 13 network nodes (red) represent proteins produced by a protein-coding gene with respect to the significantly enriched GO-term of CC: extracellular exosome GO0070062 with FDR rate of 3.6×10^{-5} . The lines (with different thickness) indicates the strength of data support due to their protein-protein associations [73].

In the 2nd ablated layer of the same replicates the number of identified proteins was about 152 proteins on average and a standard deviation of 88.6 within the five replicates, despite the fact that there was an outlier with 29 identified proteins in total in the exp-1. Also, in the 2nd ablated layers, protein markers were identified: 28 epidermis protein markers and additionally 3 dermis protein markers. The GO analysis with respect to the significantly enriched GO-term of cellular component (CC) describes 16 of these 28 epidermis protein markers in extracellular vesicle (GO:1903561) with a FDR rate of 3.1×10^{-5} ; 15 proteins are classified as extracellular exosomes (GO:0070062) with a FDR rate of 1.2×10^{-4} and 3 proteins are cornified envelope proteins (GO:0001533) with a FDR rate of 7.1×10^{-4} , which are specific for desquamation step of epidermis renewal cycles [11]. The functional enrichment is shown in a network in figure 53, with each node representing all the proteins produced by a single, protein-coding gene as described above. The proteins of interest are those contain in cornified envelopes stratified squamous epithelia, namely IVL (involucrin), CST6 (cystatin-M) and SCEL (sciellin). As mentioned before protein composition of the cornified envelopes are responsible for the skin barrier function and during the aging process, a dramatical change within the protein

composition of these dead cells are observed among other factors such as circulation rate of keratinocytes and reduction and fragmentation of the extracellular collagen matrix in dermis [1].

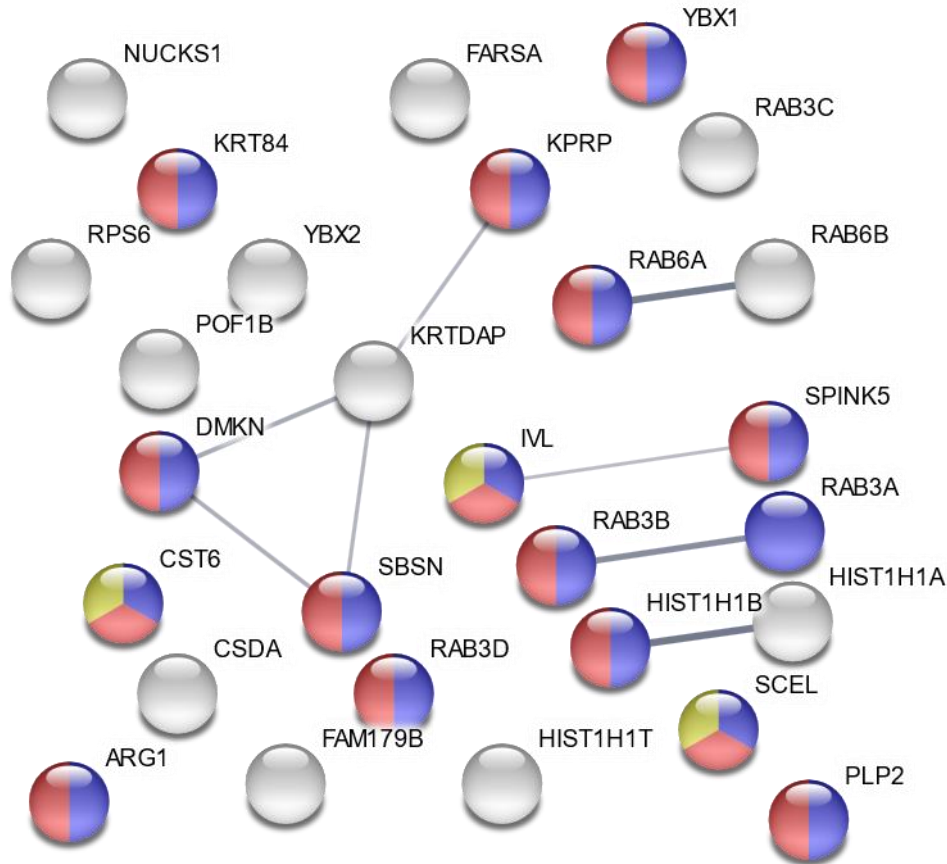


Figure 53: Gene ontology (GO) information of the 28 epidermal protein markers in 2nd ablated layers. The network nodes represent proteins produced by a protein-coding gene with respect to the significantly enriched GO-term of CC: 16 proteins are in extracellular vesicle GO1903561 (blue) with FDR rate of 3.1×10^{-5} ; 15 proteins in extracellular exosome GO0070062 (red) with FDR rate of 1.2×10^{-4} and 3 proteins in cornified envelope GO0001533 (yellow) with FDR rate of 7.1×10^{-4} . The lines (with different thickness) indicates the strength of data support due to their protein-protein associations [73].

In the 3rd layer 163 proteins were averagely identified with an error factor of 56.6 within the three replicates. In the 3rd layer, 26 epidermis protein markers and no dermis protein marker were identified. The GO analysis classified proteins with respect to significantly enriched GO-terms of cellular component (CC) as shown in the network figure 54 (left): 19 proteins belong to the GO-term extracellular region (GO:0005576) with a FDR rate of 2.3×10^{-6} , 16 proteins belong to to the GO-term extracellular exosome (GO:0070062) with a FDR rate of 2.3×10^{-6} and 4 proteins to the cornified envelope (GO:0001533) with a FDR rate of 3.5×10^{-6} . A further

GO analysis is the biological process (BP). The proteins are categorized in the respect to significantly enriched GO-terms of BP as shown in the network figure 54 (right). 6 proteins are involved in epidermis development process (GO:0008544) with a FDR rate of 0.0085 and 5 proteins in skin development (GO:0043588) with a FDR rate of 0.0225. These proteins are EVPL (envoplakin) a linkage component between the cornified envelope and desmosomes and intermediate filaments [11]; IVL (involucrin); SCEL (sciellin) assembles and regulates proteins in the cornified envelope; SPINK5 (serine peptidase inhibitor, kazal type 5) regulates the activity of defense-activating and desquamation-involved proteases; KRT84 (keratin 84) and CST6 (cystatin-M).

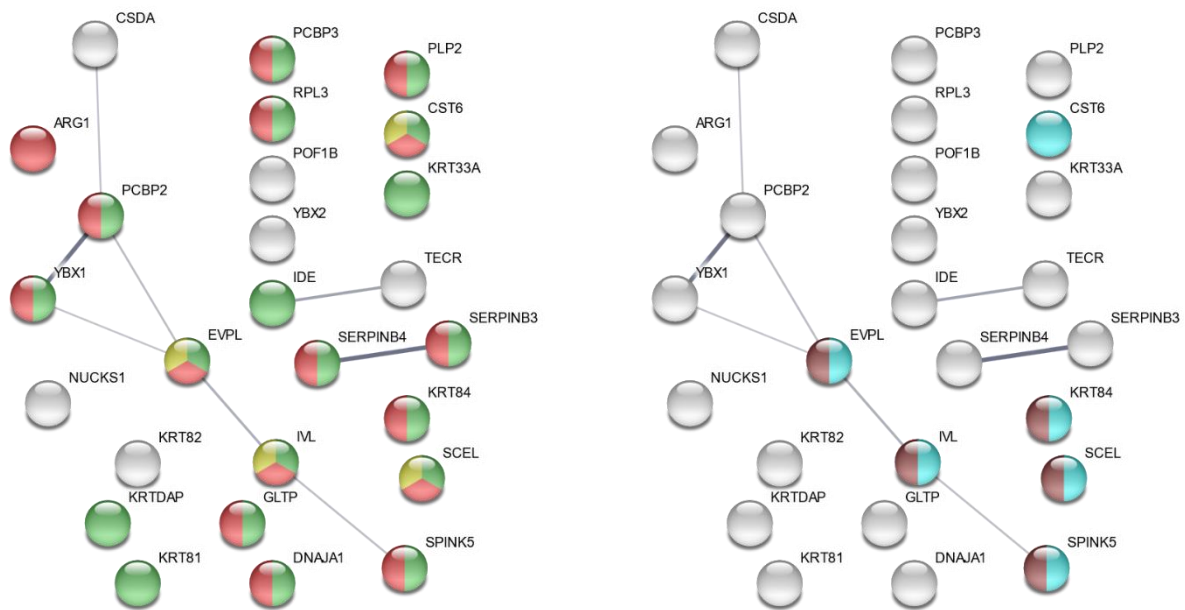


Figure 54: Gene ontology (GO) information of the 26 epidermal protein markers in 3rd ablated layers. The network nodes represent proteins produced by a protein-coding gene with respect to the significantly enriched GO-term. *Left.* CC classification: 19 proteins are in extracellular region GO0005576 (green) with FDR rate 2.3×10^{-6} ; 16 proteins in extracellular exosome GO0070062 (red) with FDR rate 2.3×10^{-6} and 4 proteins in cornified envelope GO0001533 (yellow) with FDR rate 3.5×10^{-6} . *Right.* biological process (BP) classification: 6 proteins are involved in epidermis development GO0008544 (light blue) with FDR rate of 0.0085 and 5 proteins in skin development GO0043588 (brown) with FDR rate of 0.0225. The lines (different thickness) indicates the strength of data support due to their protein-protein associations [73].

Altogether, 48 epidermis protein markers were identified in the ablated layers. These proteins are listed in table 14 and the protein markers identified in each layer are marked by “percentages” from 0.2 to 1.0 with the meaning that protein was identified in biological samples between 1 to 5, while 0.2 means only in one of five and 1.0 means in all five biological replicates. And in the 3rd ablated layers the identified protein markers are labeled by 0.33, 0.66

and 1.0 because of the three-total number of biological samples (e.g. 0.33 means the protein was identified in at least one from three biological replicates).

Table 14: 48 epidermal protein markers discovered in all three ablated layers in “experiment PIRL layer-by-layer P”. There are listed: protein marker categories I, II and III, accession (UNIPROT accession numbers [71]), protein description, gene names, 1st, 2nd and 3rd ablated layers. The numbers 0.2, 0.33, 0.4, 0.6, 0.66, 0.8 and 1.0 show the identification of proteins in each biological replicate. (explanation: 0.2 means the protein was identified in one of five biological sample, while 1.0 means protein was identified in all five biological replicates; in the case of the 3rd ablated layers 0.0.33 means the protein was identified in one of three biological samples and 0.66 means in at least two of three)

categ.	accession (UNIPROT)	protein description	gene name	1st	2nd	3rd
I	Q6E0U4	Dermokine	DMKN	0.2	0.2	
I	Q9NQ38	Serine protease inhibitor Kazal-type 5	SPINK5	0.2	0.4	0.66
I	P60985	Keratinocyte differentiation-associated protein	KRTDAP	0.2	0.2	0.33
I	O95171	Sciellin	SCEL		0.2	0.33
I	P48594	Serpin B4	SERPINB4			0.33
II	Q6UWP8	Suprabasin	SBSN	0.2	0.2	
II	Q8WVV4	Protein POF1B	POF1B	0.2	0.4	0.66
II	Q15828	Cystatin-M	CST6	0.8	0.6	1.0
II	Q9H1E1	Ribonuclease 7	RNASE7	0.2		
II	Q04941	Proteolipid protein 2	PLP2 A4	0.2	0.4	0.33
II	Q9HAT2	Sialate O-acetylerase	SIAE YSG2	0.2		
II	P07476	Involucrin	IVL		0.4	1.0
II	Q5T749	Keratinocyte proline-rich protein	KPRP		0.2	
II	P14735	Insulin-degrading enzyme	IDE			0.33
III	Q92817	Envoplakin	EVPL	0.2		0.33
III	P05089	Arginase-1	ARG1	0.2	0.2	0.33
III	P20336	Ras-related protein Rab-3A	RAB3A		0.2	
III	Q9Y2T7	Y-box-binding protein 2	YBX2		0.4	0.66
III	P29508	Serpin B3	SERPINB3			0.33

Results and discussion

categ.	accession (UNIPROT)	protein description	gene name	1st	2nd	3rd
III	Q9NZ01	Very-long-chain enoyl-CoA reductase	TECR			0.33
III	Q9NSB4	Keratin, type II cuticular Hb2	KRT82			0.33
	Q96P63	Serpin B12	SERPINB12	0.2		
	P16401	Histone H1.5	HIST1H1B	0.2	0.4	
	Q8NC51	Plasminogen activator inhibitor 1 RNA-binding protein	SERBP1	0.2		
	Q9Y6G9	Cytoplasmic dynein 1 light intermediate chain 1	DYNC1LI1	0.2		
	P22492	Histone H1t	HIST1H1T	0.4	0.2	
	Q02539	Histone H1.1	HIST1H1A	0.4	0.2	
	Q9Y285	Phenylalanine--tRNA ligase alpha subunit	FARSA	0.2	0.2	
	Q9HCC0	Methylcrotonoyl-CoA carboxylase beta chain, mitochondrial	MCCC2	0.2		
	Q8WVJ2	NudC domain-containing protein 2	NUDCD2	0.2		
	P16989	Y-box-binding protein 3	YBX3		0.4	0.66
	O95716	Ras-related protein Rab-3D	RAB3D		0.2	
	P62753	40S ribosomal protein S6	RPS6		0.2	
	P67809	Nuclease-sensitive element-binding protein 1	YBX1		0.4	0.66
	P20340	Ras-related protein Rab-6A	RAB6A		0.2	
	Q9NRW1	Ras-related protein Rab-6B	RAB6B		0.2	
	Q9H1E3	Nuclear ubiquitous casein and cyclin-dependent kinase substrate 1	NUCKS1		0.8	1.0
	P20337	Ras-related protein Rab-3B	RAB3B		0.2	
	Q96E17	Ras-related protein Rab-3C	RAB3C		0.2	
	Q9NSB2	Keratin, type II cuticular Hb4 (Keratin-84)	KRT84		0.2	0.33
	Q9Y4F4	Crescerin-1	TOGARAM1		0.2	
	Q14533	Keratin, type II cuticular Hb1 (Keratin-81)	KRT81			0.33
	P39023	60S ribosomal protein L3	RPL3			0.33
	O76009	Keratin, type I cuticular Ha3-I	KRT33A			0.33
	Q15366	Poly(rC)-binding protein 2	PCBP2			0.33
	Q9NZD2	Glycolipid transfer protein (GLTP)	GLTP			0.33
	P31689	Heat shock 40 kDa protein 4	DNAJA1			0.33
	P57721	Poly(rC)-binding protein 3	PCBP3			0.33

Considering the results of the 1st and 2nd ablated layers carried out so far that the most identified protein markers are detected in one or two biological replicates. These results could be affected by the suppression of signals during the LC-MS/MS analysis caused by the abundant proteins such as albumin, desmoplakin, filaggrin and keratins (e.g. keratins type I: K1C9, K1C10, K1C13, K1C14, K1C15, K1C16, K1C17, K1C25, K1C27, K1C28 and keratins type II: K2C1, K2C4, K2C5, K2C8, K2C6A, K2C6B, K2C6C, K22E, etc.). These proteins comprise 70 to 80% of the skin dry weight and the dynamic ranges of these abundant proteins in skin complicates the detection of lower abundant proteins [10]. Besides, the collecting of aerosol using cooling trap was not efficient due to the facts explained before. Nonetheless, there were protein markers for epidermis which can elucidate the depth of ablated areas by PIRL-DIVE.

The first five proteins are specifically marked as category I protein markers (see in table 8 the top 50 epidermis protein markers). The cellular location of these proteins and their proteoforms together with their regulation factors describe their biological functions in the epidermis. Disruption in the functions and structure caused by mutation or environmental stress leads to diseases. In the following chapter, five of these epidermal protein markers are explained with respect to their function and possible associated diseases by reference to “THE HUMAN PROTEIN ATLAS” database [67] and OPEN TARGETS PLATFORM [75]. In terms of the knowledge on the locus of proven proteoforms, the ablation depth of each layer can be estimated.

Dermokine is a protein coded by the DMKN gene. Besides the known differentiation genes KRT1 (encoding Keratin 1) and FLG (encoding filaggrin), DMKN is one of the most highly expressed genes. Dermokine operates as a soluble regulator of keratinization and is one of main component of cornified envelop assembly. Furthermore, a highly regulation of DMKN proteoforms β and γ are secreted by the lamellar bodies and are observed in granular keratinocytes (in stratum granulosum, between the granular and the cornified layers) whereby the proteoforms α and δ exhibit an equal amount in the whole epidermis [76,77,83]. DMKN is associated in 23 diseases: six of these are categorized as skin diseases. In figure 55, the IHC image of dermokine in skin tissue as well as the profile of the diseases associated with DMKN gene is shown.

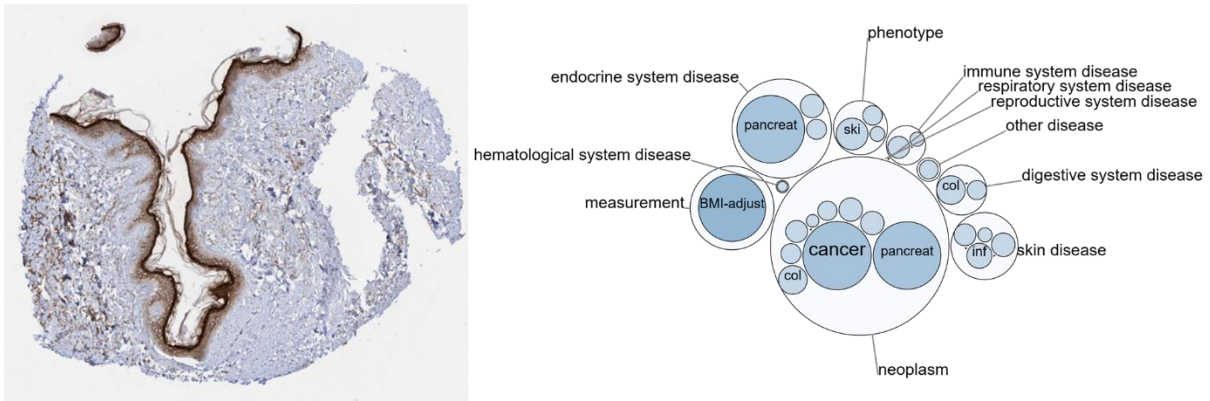


Figure 55: IHC image of stained human skin tissue section represented the dermokine (gene name: DMKN) with respect to the HPA029406 antibody [77] as well as the profile of the diseases [75]. *Left:* IHC image, the stained brown area shows keratinocytes and Langerhans cells and melanocytes whereby the protein is synthesized mainly in stratum granulosum. *Right:* Diseases profile: DMKN is associated in 23 diseases as currently known, whereas six of these are skin diseases.

Dermokine was identified in the first and second ablated layers. Due to the information about the DMKN gene expression, the PIRL ablated through the stratum corneum and stratum granulosum.

Serine peptidase inhibitor Kazal type 5 (Serine protease inhibitor, protein-coding gene SPINK5) has an alternative name: Lympho-epithelial Kazal-type-related inhibitor or LEKT1, because of its function in the production of white blood cells known as lymphocytes. This protein has anti-inflammatory and antimicrobial properties and therefore plays a crucial role in the protection of mucous epithelia but also in the morphogenesis and development of protective epidermal barrier function by regulating the activity of proteases which are involved in defense-activating as well as in desquamation. Thus, SPINK5 participates in the physiological renewal of skin by exhibiting various inhibitory potentials for multiple proteases such as KLK5, KLK7, KLK14, CASP14, and trypsin. The protein is secreted mainly in extracellular spaces of the superficial stratum granulosum and in stratum corneum, which is the outermost layer of skin and provides a steady barrier between body and environment. In stratum corneum, several serine peptidase enzymes exist with a target of breaking the connection of cells. Controlling their activity has an enormous primness for the immune system. Lack of this protein causes serine peptidases to stay in their activite form and destroy proteins in the stratum corneum. This results in excessive skin shedding and leads to an immune dysfunction. So far, SPINK5 is involved in 131 diseases from those 76 are associated with skin diseases. One of the most common skin diseases is an autosomal recessive skin disorder

caused by a mutation of the SPINK5 gene, termed Netherton syndrome [78-80]. The diseases profile associated with the SPINK5 gene and the IHC image of Serine peptidase inhibitor Kazal type 5 are presented in figure 56.

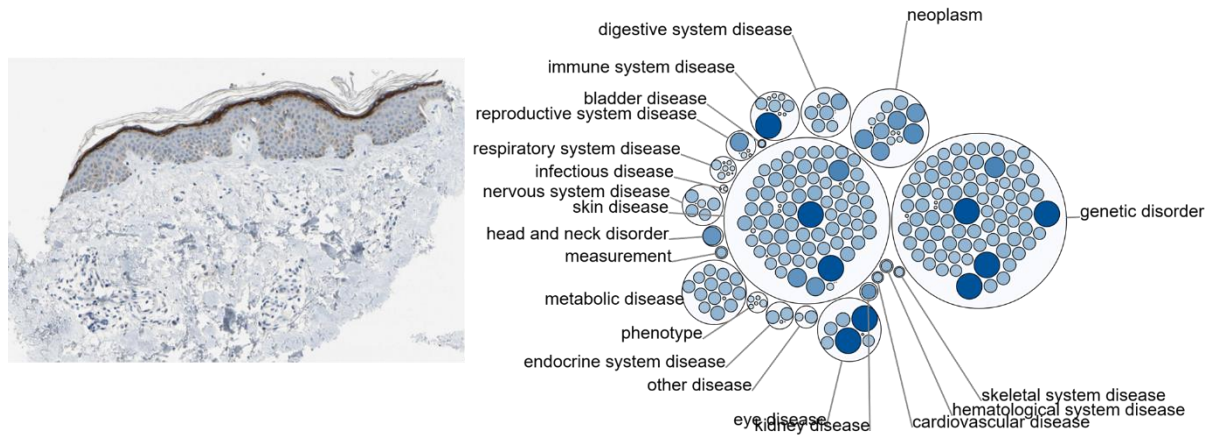


Figure 56: IHC image of stained human skin tissue section represented the Serine peptidase inhibitor Kazal type 5 (gene name: SPINK5) with respect to the HPA009067 antibody [80] as well as the profile of the diseases [75]. *Left:* IHC image: the stained brown area shows the secreted proteins in keratinocytes whereby the protein is detected highly in extracellular spaces of the superficial stratum granulosum and in stratum corneum with the main task of regulating the activity of epidermal proteases involved in the barrier formation. *Right:* Diseases profile: SPINK5 is associated in 131 diseases as currently known, whereas 76 of these are skin diseases.

Serine peptidase inhibitor Kazal type 5 was identified in all three ablated layers (1st, 2nd, and 3rd layers). It is presumed that the PIRL ablation of epidermal layers succeeded as the detected protein is common for the first outermost strata in the epidermis, namely the stratum corneum and the granulosum.

Keratinocyte differentiation-associated protein (protein-coding gene KRTDAP) serves as a soluble regulator of keratinocytes differentiation, maintenance of stratified squamous epithelia as well as one of the key regulators in the embryonic skin morphogenesis. It is secreted by keratinocytes and mainly detected in lamellar granules of granular keratinocytes and in the intercellular space of cornified envelopes [81]. An upregulation of KRTDAP encoded protein is observed in chronic skin diseases that arise by disrupted skin barrier due to altered keratinocyte differentiation, such as psoriasis, ichthyosis and atopic dermatitis [81-84]. KRTDAP is involved in psoriasis disease, next to 3800 targets associated with psoriasis as per the information of “OPEN TARGETS PLATFORM” [75]. This example shows the complexity of

epidermal protein composition and the importance of the knowledge about their function, their intra- and extracellular correlation and their dysfunction. In figure 57, the IHC image of stained keratinocyte differentiation-associated proteins in keratinocytes in stratum granulosum and stratum corneum and the disease profile are shown.

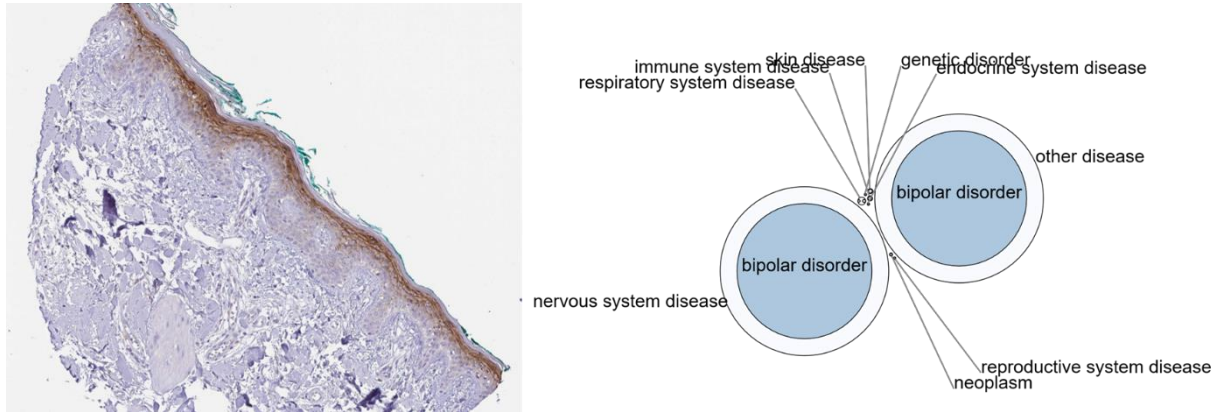


Figure 57: IHC image of stained human skin tissue section represented Keratinocyte differentiation-associated protein (gene name: KRTDAP) with respect to the HPA063474 antibody [84] as well as the profile of the diseases [75]. *Left:* IHC image: the stained brown area shows the secreted proteins in keratinocytes whereby the protein is detected mainly in lamellar granules of granular keratinocytes and in the intercellular space of cornified envelopes. It may function as a regulator of keratinization and is responsible for maintenance of stratified epithelia. *Right:* Diseases profile: KRTDAP is associated with four diseases as currently known.

Keratinocyte differentiation-associated protein was identified like SPINK5 in all three ablated layers of the skin tissues. It indicates that the PIRL irradiation penetrates the stratum corneum and stratum spinosum by the first as well as by the second and third ablations.

Sciellin (encoded by SCEL) is a plasma protein which may function as a precursor to the cornified envelopes of the terminally differentiated keratinocytes. It is synthesized in the stratum granulosum. Its pathophysiological importance touched up in assembly or regulation of proteins in cornified envelopes and may be involved in homotypic or heterotypic associations of keratinization [85,86]. There 25 are known diseases associated with SCEL, and six of these are categorized as skin diseases (figure 58).

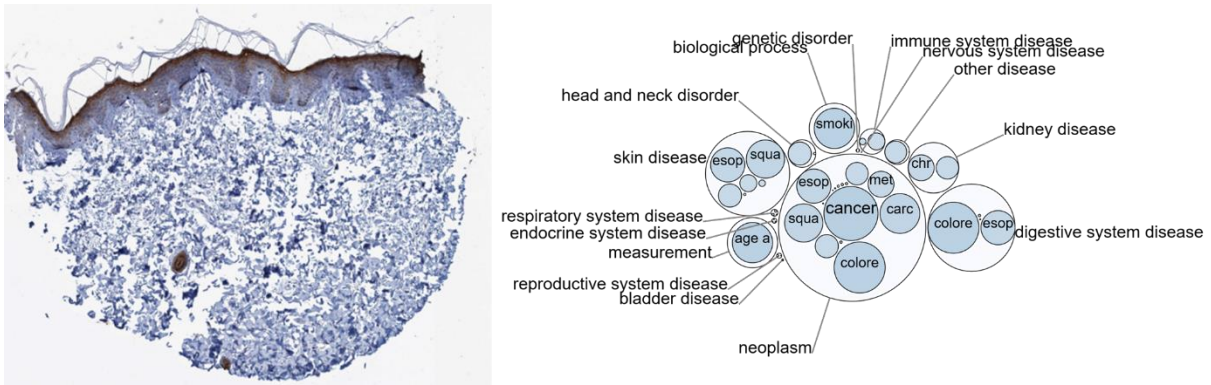


Figure 58: IHC image of stained human skin tissue section represented Sciellin (gene name: SCEL) with respect to the HPA040154 antibody [85] as well as the profile of the diseases [75]. *Left.* IHC image: the stained brown area shows the plasma proteins in keratinocytes whereby the protein is detected mainly in stratum granulosum and in cornified envelopes. SCEL may act in the assembly or regulation of proteins in the cornified envelopes. *Right.* Diseases profile: SCEL is associated in 25 diseases as currently known, whereas six of these are skin diseases.

Sciellin is another marker for stratum granulosum and was identified in the 2nd and 3rd ablated cell layers. It proves the PIRL achieved the stratum granulosum already during the 2nd ablation.

Serpin B4 is encoded by the SERPINB4 gene. It is the member 4 of the serpin family of serine protease inhibitor (family B) which regulates the host immune response against tumor cells. It inactivates the granzyme M, which kills the tumor cells. Serpin B4 is associated with 47 diseases such as chromosome 18Q Deletion Syndrome and Squamous cell Carcinoma (SCC) (shown in figure 59). Among these known diseases, 13 are skin diseases. The protein B4 and its paralog B3 can be decomposed into smaller fragments. The aggregation of fragments of both proteins may form autoantigen in psoriasis, which is presumed to be the reason for the chronic inflammation in patients.

cell has a size of 30 μm averagely [89]. The size of keratinocytes is presumed to be between 10 to 20 μm [88, 90] and the size of fibroblasts is presumed to be 80 to 100 μm [91]. This indicates in each layer, 1.5 of dead and living keratinocytes are removed by PIRL-DIVE as expected with an ablation depth of 15 μm . Challenging is the knowledge about the thickness of the tissue before ablating. The thickness of the tissue as explained before is dependent on the age of the donor (the older the donor the thinner the epidermis and more fragile the collagen fibers which induce deep wrinkles [1]), also the body region where the biopsy comes from (face, breast, abdominal or palm, etc. [97]) and finally the epithelial rete ridges pattern [53] exacerbates the problem to remove epidermal cell layers definable from each other and ultimately from the dermis. In a few of the replicates of the 1st and 2nd ablated layers 4 dermis protein markers were identified: KRT20, KRT222, a tubulin beta-8 chain-like protein and RAB4B. This could be explained by the rete ridges structure of skin which increases the difficulty factor of a linear ablation by PIRL-DIVE. Nevertheless, mistakes can never be completely ruled out given the fact that the PIRL is a prototype laser system. Within a longer time while the device was running a change of the shape of laser spot was observed. The circle was changed to an ellipse which greatly influenced the laser frequency. The laser energy within an ellipse-shaped spot is not distributed equally compared to a circle-shaped spot. The laser energy decrease along the edge of the ellipse, while in the circle-shaped spot the laser energy is almost the same. For this reason, it cannot be ruled out, that the laser energy achieved deeper the tissue in some areas of the spots where the energy is higher.

4.4.2.2. Experiment PIRL layer-by-layer II:

Due to the previous results of PIRL ablated skin tissues, several optimized measures were contemplated as follows: a new chamber design (the second-generation chamber with an irregular airfoil shape based on the aerodynamic concept) and the filter holder (the first version) for borosilicate filter paper and in addition the SDC/urea protocol was used for denaturation and digestion.

The layer-by-layer ablation was performed with an energy output level of 135 $\mu\text{J}/\text{pulse}$ and a peak pulse fluence of 0.5 J/cm^2 . To achieve a high protein yield, six domains of each skin tissue was scanned with an area of about 4.7x4.4 mm and all six homogenates were collected on one borosilicate filter paper. The scan duration pro area took about 7 sec. In total, five biological samples with different ages were used for this experiment which came from abdominal and breast reduction surgeries (25w, 33w, 35w, 48w and 70w). The ablation of first layer was repeated twice on two technical replicates of each biological sample and they were termed as e.g. 1st and 1st' layer and so on and the ablation plume was collected on different filter paper. Then the second ablation followed above the same ablated area (only for one technical replicate) and the ablation plumes of all six domains were collected again on a new filter paper. The proteins were denaturated by SDC/urea protocol and digested proteolytically prior to LC-MS/MS analysis. The ablation depths should be analyzed by confocal microscopy, but the contour of ablated areas was not easily defined and therefore it encountered a problem to determine the ablation depth. In table 15 the results of mass spectrometry are listed with the total number of identified proteins in each sample 1 to 5 (termed as exp-1 up to exp-5 and each layer (1st, 1st' and 2nd layer).

Table 15: The proteins identified in the second Layer-by-layer approach using the PIRL-DIVE method with its optimized parameters. The samples are from five donors (25w, 33w, 35w, 48w, 70w). The first technical replicates were ablated (1st layer). The second technical replicates were ablated like the first one (1st-layer). An additional ablation was performed above the area of the second technical replicates (2nd layer). The number of identified proteins for 1st, 2nd, and 3rd layers are listed. The mean value plus the corresponded standard deviation is carried out for each biological sample.

samples	samples (age)	number of proteins in 1st layer (techn. repl. 1)	number of proteins in 1st layer (techn. repl. 2)	number of proteins in 2nd layer
exp - 1	25w	318	389	488
exp - 2	33w	365	332	321
exp - 3	35w	429	336	383
exp - 4	48w	281	276	291
exp - 5	70w	278	339	306
mean	---	334	334	358
standard deviation	---	56.9	35.8	72.2

The first ablated layers are performed twice meaning two technical replicates for each biological sample. Considering the number of identified proteins in the technical replicates of first ablated layers and also the second layers, there is no correlation between the number of identified proteins in all biological samples. The mean value of technical replicate 1 and technical replicate 2 are both 334 protein and the standard deviation values are 56.9 and 35.8. The 2nd ablated layers yield into the same range with 358 proteins at average and a standard deviation of 72.2. Nonetheless, the achieved number of identified proteins with the filter holder with a mean value of 342 within all three ablated layers was much higher than the cooling trap with a mean value of 158. In comparison to the results of *experiment PIRL layer-by-layer I*, this indicates that the filter holder (1st version) with borosilicate filter paper is a better trap construction than the cooling trap. This is largely because of the miniaturized size of trap, continuously generation of laminar air flow, quick powdering of homogenate and absence of dilution factor. Further, the SDC/urea extraction protocol enables a higher and more reproducible protein recovery than the extraction methods with SDC alone or urea alone.

In figure 60, the mass spectrometry results of the tryptic digested peptides analyzed via LC-MS/MS are demonstrated in a bar chart diagram and the Venn diagrams are there to visualize the overlapping between the ablated layers.

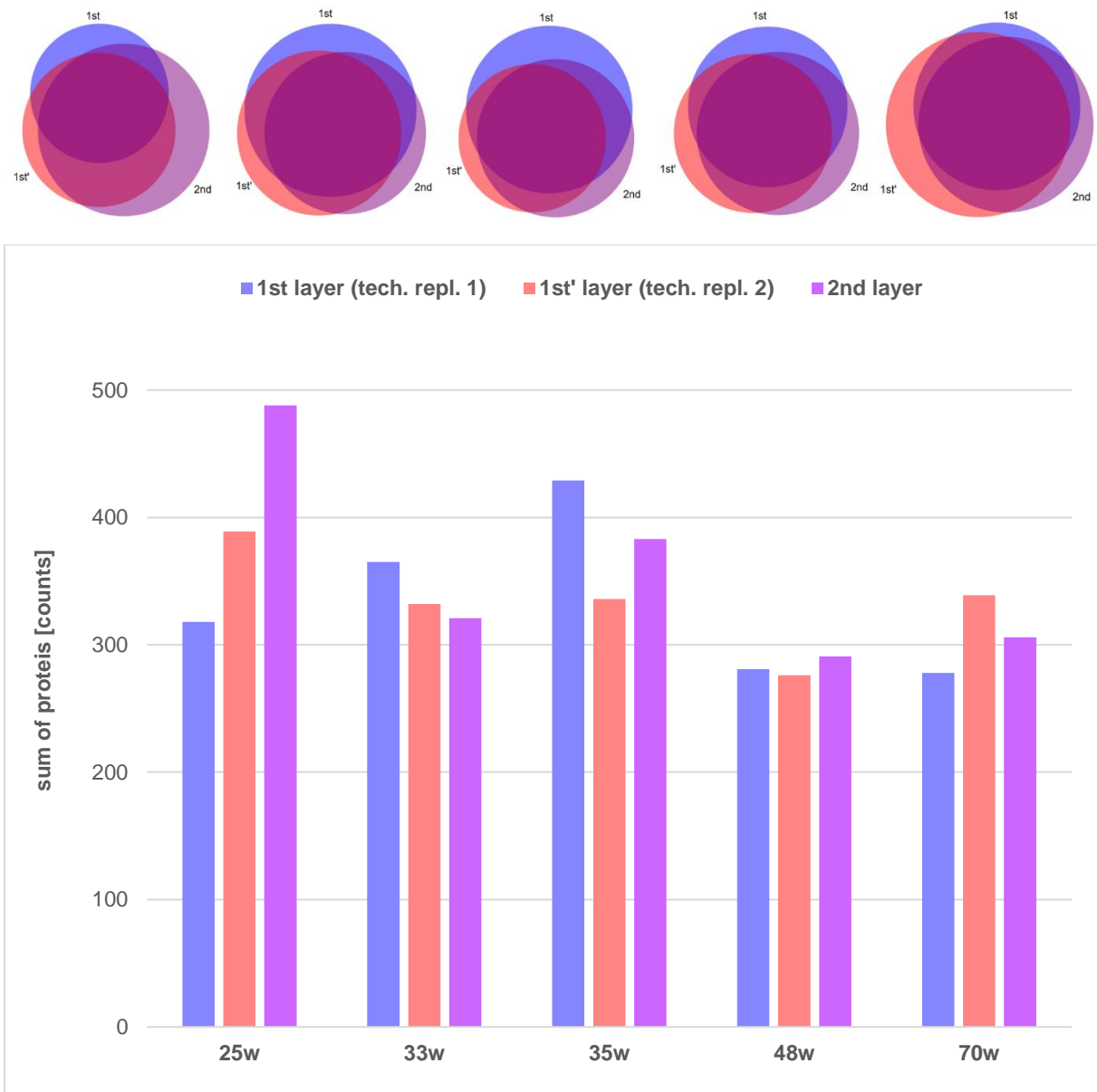


Figure 60: Statistical analysis of the LC-MS/MS data from tryptic digested peptides from ablated skin tissues by a layer-by-layer approach. *Top:* The five Venn diagrams visualize the overlap of all identified proteins (unique peptides ≥ 1) in each biological sample. The overlaps of identified proteins are shown for 1st ablated layer of two technical replicates [1st layer (tech. repl. 1) and 1st layer (tech. repl. 2)] and 2nd ablated layer of only one technical sample of each biological origin. The five biological samples originated in breast and abdominal reduction surgeries of patients with five different ages, from young to old (25w, 33w, 35w, 48w and 70w). *Bottom:* The bar chart diagram shows the total number of identified proteins in all five samples. The achieved proteins are shown for 1st ablated layer of two technical replicates (blue: 1st layer (tech. repl. 1) and red: 1st layer (tech. repl. 2)) and 2nd ablated layer (purple) of only one technical sample of each biological origin.

The Venn diagrams represent almost the same intersection range at an average of 236 proteins (standard deviation 20.1) in all three ablated layers. The number of proteins identified exclusively in one layer (in each biological sample) was negligibly low, except for the 1st layer in exp-3 and 2nd layer in exp-1 which both had in total a higher number of identified proteins in comparison to the other samples (429 and 488 protein).

In the bar chart diagram, the number of identified proteins for the first layers is ranged between 276 and 429 proteins per replicate and in the second layer 291 to 488. Nevertheless, the variation of identified proteins within the technical and biological replicates are still high, but it is obvious again that the older the tissue, the fewer the number of identified proteins, especially in the first layers. A further point is as explained before the unknown lipid content in epidermis which varies from individual to individual and can affect the protein identification and leads to false positive results.

According to the mass spectrometry results, in 1st ablated layer 334 proteins were identified at average with a standard deviation of 56.9 within the five biological replicates. Comparing the results to the epidermis and dermis protein marker libraries, it yielded in 57 epidermis and 18 dermis biomarkers. The GO analysis in STRING database [73] against the whole human genome describes the 57 epidermis biomarkers with respect to significantly enriched GO-term of cellular component (CC). The functional enrichment of these protein markers is shown in a network in figure 61 (left) with each node that represents all the proteins produced by a single, protein-coding gene. 39 proteins were in the GO-term extracellular region (GO:0005576) with a FDR rate of 2.3×10^{-12} . 32 proteins were extracellular vesicle proteins (GO:1903561) with a FDR rate of 3.1×10^{-12} . 31 proteins were in extracellular exosome (GO:0070062) with a FDR rate of 1.5×10^{-11} . 5 proteins were cornified envelope proteins (GO:0001533) with a FDR rate of 5.9×10^{-7} and 3 proteins epidermal lamellar body proteins (GO:0097209) with a FDR rate of 3.2×10^{-5} . The lamellar bodies are produced in the stratum spinosum and granulosum and are the main component for continuing formation of cornified envelopes. The secreted lamellar body's contents are primarily intended for permeability barrier as well as antimicrobial properties of skin [1]. The biological process GO analysis (shown in the network in figure 61 (right)) yielded in 12 proteins that are involved in epidermis development (GO:0008544) with a FDR rate of 4.5×10^{-8} ; 10 proteins in skin development (GO:0043588) with a FDR rate of 1.6×10^{-6} ; 6 of these proteins are involved as well in epidermal cell differentiation (GO:0009913) with a FDR rate of 0.00358 and five of these proteins in keratinocyte differentiation (GO:0030216) with a FDR rate of 0.00744. Most of these proteins are of significance due to their functions: KLK5 (Kallikrein-related peptidase 5) and KLK 7 (Kallikrein-related peptidase 7) are involved in desquamation, both peptidases catalyze the degradation process of intercellular cohesive structures of cornified envelopes [79]. TGM1 (Transglutaminase 1)

catalyze the cross-linking of Ca²⁺-dependent proteins such as envoplakin, involucrin and periplakin [1]. LOR (loricrin) is a major component of keratinocyte cell envelope protein [93]. ALOXE3 (arachidonate lipoxygenase 3) and ALOX12B (arachidonate 12-lipoxygenase, 12R type) belong to the arachidonate lipoxygenases enzyme family. Both enzymes were involved in the lipid metabolism pathway, namely the hydroperoxy eicosatetraenoic acid biosynthesis. In presence of oxygen, the non-heme iron-containing dioxygenases catalyze the stereospecific peroxidation of polyunsaturated fatty acids, to generate fatty acid hydroperoxides that plays crucial role in the synthesis of the lipid containing cornified layers and the maintenance of the water-repellent epidermal barrier function [94,95].

The results of 1st ablated layers for technical replicates of the five biological replicates was similar to the results obtained for the 1st layer. The average number of identified proteins was about 334 proteins and the standard deviation was about 35.8. In total, 66 epidermis and 10 dermis biomarkers were identified. The GO analysis in STRING database [73] describes the 66 epidermis biomarkers with respect to significantly enriched GO-term of cellular component (CC) and they are shown in figure 62 (left). 40 of these proteins are classified in extracellular region GO term (GO:0005576) with FDR rate of 1.2×10^{-10} . 32 proteins are extracellular vesicle proteins (GO:1903561) with FDR rate of 2.6×10^{-10} and 31 are extracellular exosome proteins (GO:0070062) with FDR rate of 9.6×10^{-10} . 6 of these proteins are cornified envelopes proteins (GO:0001533) with FDR rate of 1.1×10^{-8} . The BP GO analysis is illustrated as network in figure 62 (right) and describes 13 of these 66 epidermis biomarkers in the epidermis development process (GO:0008544) with a FDR rate of 9.2×10^{-9} ; 11 proteins are involved in skin development (GO:0043588) with a FDR rate of 2.5×10^{-7} ; 7 of these proteins are involved in epidermal cell differentiation process (GO:0009913) with a FDR rate of 5.1×10^{-4} and 6 in keratinocyte differentiation (GO:00030216) with a FDR rate of 7.7×10^{-4} .

The achieved number of proteins in the 2nd ablated layer yielded in 358 proteins at average and an error factor of 72.2 within the five biological replicates. The comparison of the protein lists with epidermis and dermis protein libraries resulted into 88 epidermis proteins markers and 9 dermis protein markers. The GO analysis in STRING database [73] clustered the proteins with respect to CC Go terms (figure 62, left): 44 proteins are extracellular vesicle proteins (GO:1903561) with FDR rate of 2.9×10^{-16} ; 43 extracellular exosome proteins (GO:0070062) with a FDR rate of 1.0×10^{-15} ; 51 extracellular region proteins (GO:0005576) with FDR rate of 6.9×10^{-15} ; 7 cornified envelope proteins (GO:0001533) with FDR rate of 3.2×10^{-10} and 3 proteins are epidermal lamellar bodies (GO:0097209) with FDR rate of 7.2×10^{-5} . The BP GO analysis shows in the network in figure 63 (right) 15 proteins in the process of epidermis development (GO:0008544) with a FDR rate of 4.7×10^{-10} ; 14 proteins are involved in skin development (GO:0043588) with a FDR rate of 4.7×10^{-10} ; 8 in epidermal

cell differentiation process (GO:0009913) with a FDR rate of 2.3×10^{-4} and 7 proteins in keratinocyte differentiation (GO:00030216) with a FDR rate of 2.7×10^{-4} . The most part of these proteins are the decisive factor for pathways of keratinization and desquamation within epidermis as explained above.

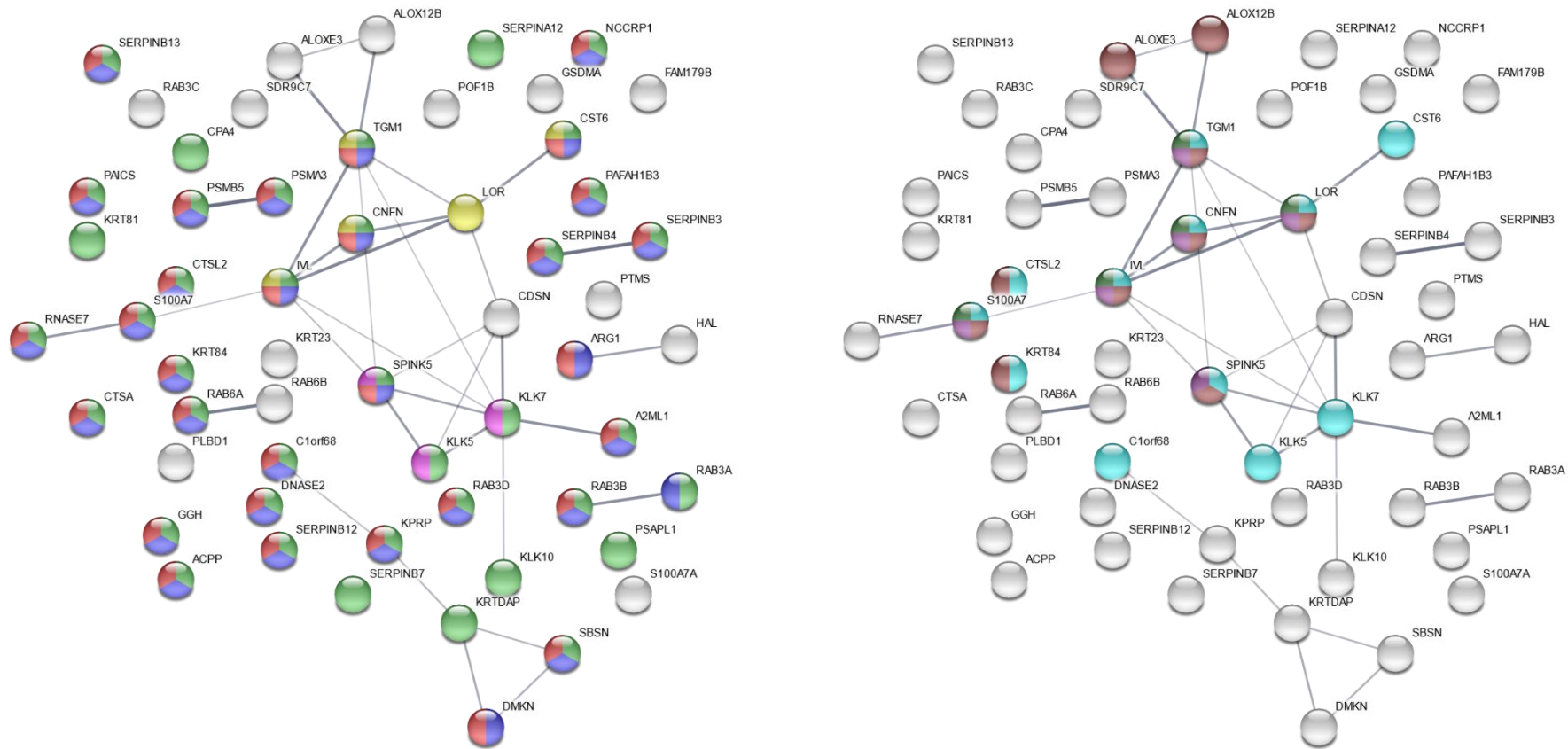


Figure 61: Gene ontology (GO) information of the 57 epidermal protein markers in 1st ablated layers. The network nodes represent proteins produced by a protein-coding gene with respect to the significantly enriched GO-term. *Left:* CC classification: 39 proteins are in extracellular region GO0005576 (green) with FDR rate 2.3×10^{-12} ; 32 proteins extracellular vesicle GO1903561 (blue) with FDR rate 3.1×10^{-12} , 31 proteins in extracellular exosome GO0070062 (red) with FDR rate 1.5×10^{-11} ; 5 proteins in cornified envelope GO0001533 (yellow) with FDR rate 5.9×10^{-7} and 3 proteins in epidermal lamellar body GO0097209 (purple) with FDR rate 3.1×10^{-5} . *Right:* biological process (BP) classification: 12 proteins are involved in epidermis development GO0008544 (light blue) with FDR rate of 4.5×10^{-8} ; 10 proteins in skin development GO0043588 (brown) with FDR rate of 1.6×10^{-6} ; 6 proteins in epidermal cell differentiation GO0009913 (violet) with FDR rate of 0.0036 and 5 proteins in keratinocyte differentiation GO0030216 (dark green) with FDR rate of 0.0074. The lines (different thickness) indicates the strength of data support due to their protein-protein associations [73].

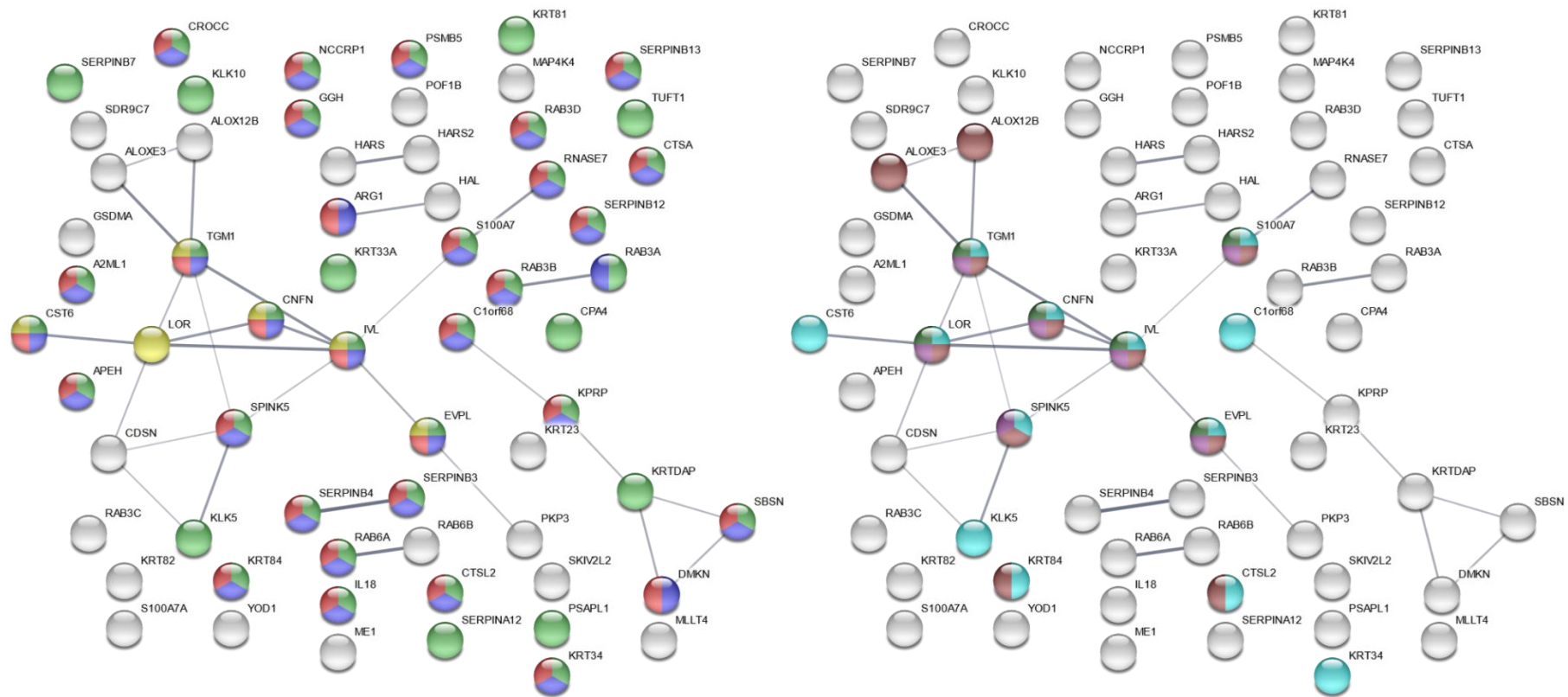


Figure 62: Gene ontology (GO) information of the 66 epidermal protein markers in 1st ablated layers. The network nodes represent proteins produced by a protein-coding gene with respect to the significantly enriched GO-term. *Left:* CC classification: 40 proteins are in extracellular region GO0005576 (green) with FDR rate 1.2×10^{-10} ; 32 proteins in extracellular vesicle GO1903561 (blue) with FDR rate 2.59×10^{-10} , 31 proteins in extracellular exosome GO0070062 (red) with FDR rate 9.6×10^{-10} and 6 proteins in cornified envelope GO0001533 (yellow) with FDR rate 1.1×10^{-8} . *Right:* biological process (BP) classification: 13 proteins are involved in epidermis development GO0008544 (light blue) with FDR rate of 9.2×10^{-9} ; 11 proteins in skin development GO0043588 (brown) with FDR rate of 2.5×10^{-7} ; 7 proteins in epidermal cell differentiation GO0009913 (violet) with FDR rate of 5.1×10^{-4} and 6 proteins in keratinocyte differentiation GO0030216 (dark green) with FDR rate of 7.7×10^{-4} . The lines (different thickness) indicates the strength of data support due to their protein-protein associations [73].

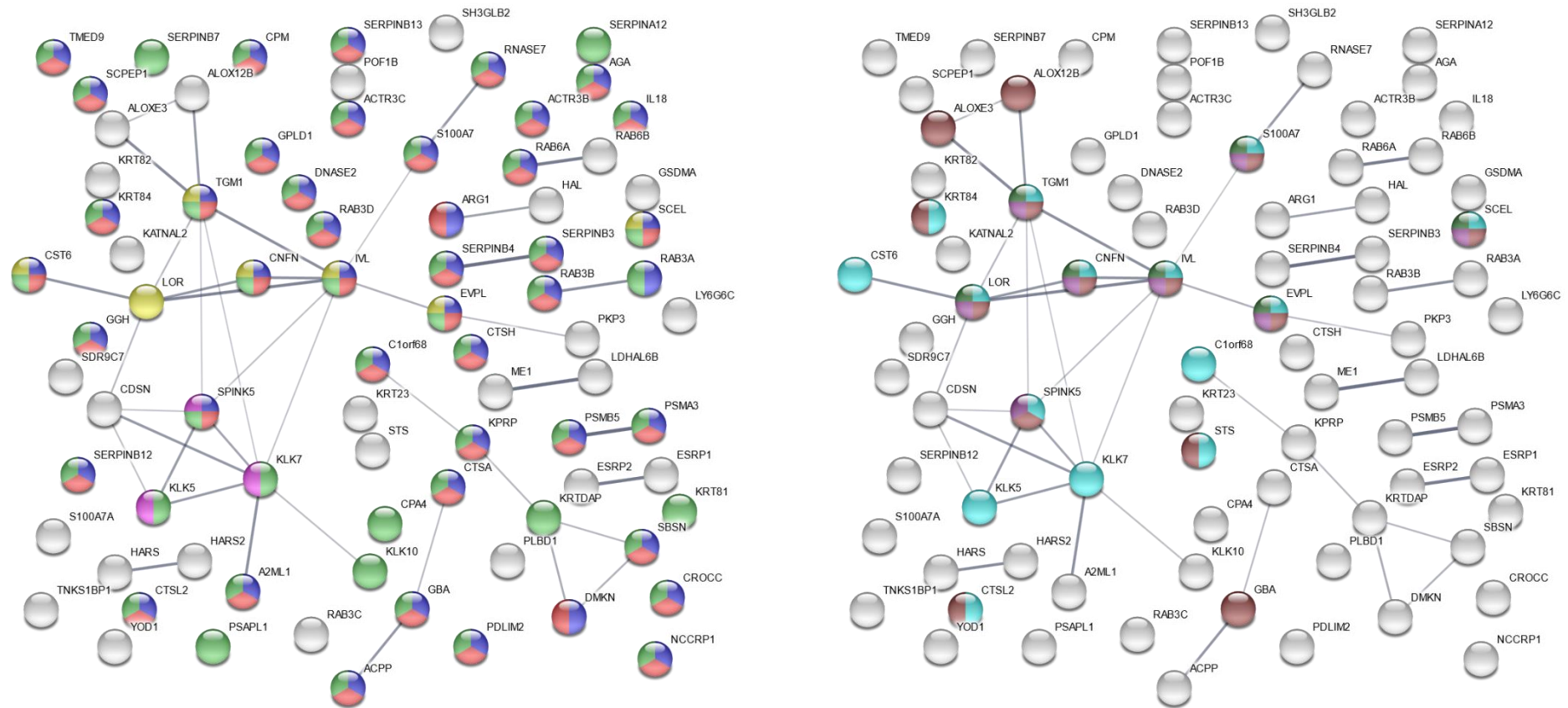


Figure 63: Gene ontology (GO) information of the 82 epidermal protein markers in 2nd ablated layers. The network nodes represent proteins produced by a protein-coding gene with respect to the significantly enriched GO-term. *Left:* CC classification: 44 proteins are in extracellular vesicle GO1903561 (blue) with FDR rate 2.9×10^{-16} ; 43 proteins in extracellular exosome GO0070062 (red) with FDR rate 1.0×10^{-15} ; 51 proteins in extracellular region GO0005576 (green) with FDR rate 6.9×10^{-15} ; 7 proteins in cornified envelope GO0001533 (yellow) with FDR rate 3.2×10^{-10} and GO0097209 (purple) with FDR rate 7.2×10^{-5} . *Right:* biological process (BP) classification: 15 proteins are involved in epidermis development GO0008544 (light blue) with FDR rate of 4.7×10^{-10} ; 14 proteins in skin development GO0043588 (brown) with FDR rate of 4.7×10^{-10} ; 8 proteins in epidermal cell differentiation GO0009913 (violet) with FDR rate of 2.3×10^{-4} and 7 proteins in keratinocyte differentiation GO0030216 (dark green) with FDR rate of 2.7×10^{-4} . The lines (different thickness) indicates the strength of data support due to their protein-protein associations [73].

Altogether, 94 epidermis protein markers were identified in the ablated layers. These proteins are listed in table 16 and the protein markers identified in each layer are marked by the numbers 0.2, 0.4, 0.6, 0.8 and 1.0 with the meaning that protein was identified in biological samples between 1 to 5, while 0.2 means only in one of five and 1.0 means in all five biological replicates.

Table 16: 94 epidermal protein markers discovered in all three ablated layers in “experiment PIRL layer-by-layer IP”. There are listed: protein marker categories I, II and III, accession (UNIPROT accession numbers [71]), protein description, gene names, 1st, 1^{st'} and 2nd ablated layers. The numbers 0.2, 0.4, 0.6, 0.8 and 1.0 show the identification of proteins in each biological replicate. (explanation: 0.2 means the protein was identified in one of five biological sample, while 1.0 means protein was identified in all five biological replicates).

categ.	accession (UNIPROT)	protein description	gene name	1st	1st'	2nd
I	A8K2U0	Alpha-2-macroglobulin-like protein 1	A2ML1	1.0	1.0	0.8
I	Q6E0U4	Dermokine	DMKN	0.8	0.8	1.0
I	Q9NQ38	Serine protease inhibitor Kazal-type 5	SPINK5	0.4	0.6	0.8
I	Q86SG5	Protein S100-A7A	S100A7A	0.4	0.8	1.0
I	P48594	Serpin B4	SERPINB4	1.0	1.0	1.0
I	P60985	Keratinocyte differentiation-associated protein	KRTDAP	0.8	0.4	1.0
I	O15231	Zinc finger protein 185	ZNF185		0.2	
I	O95171	Sciellin	SCEL			0.2
I	P04062	Glucosylceramidase	GBA			0.2
II	P23490	Loricrin	LOR	0.2	0.4	0.2
II	Q9BYD5	Cornifelin	CNFN	0.4	0.2	0.2
II	Q6UWP8	Suprabasin	SBSN	1.0	1.0	1.0
II	Q8WVV4	Protein POF1B (Premature ovarian failure protein 1B)	POF1B	0.8	0.8	1.0
II	P07476	Involucrin	IVL	0.4	0.2	0.4
II	Q5T749	Keratinocyte proline-rich protein (hKPRP)	KPRP	1.0	1.0	1.0
II	O75342	Arachidonate 12-lipoxygenase, 12R-type (12R-LOX)	ALOX12B	0.4	0.8	0.6
II	P31151	Protein S100-A7 (Psoriasin)	S100A7	1.0	0.8	1.0
II	Q9BYJ1	Hydroperoxide isomerase ALOXE3	ALOXE3	0.6	0.8	0.6
II	P49862	Kallikrein-7	KLK7	0.2		0.2

Results and discussion

categ.	accession (UNIPROT)	protein description	gene name	1st	1st'	2nd
II	Q15517	Corneodesmosin	CDSN	1.0	1.0	1.0
II	Q15828	Cystatin-M	CST6	1.0	1.0	1.0
II	Q9H1E1	Ribonuclease 7	RNASE7	0.4	0.4	0.4
II	Q9UIV8	Serpin B13	SERPINB13	0.2	0.2	0.4
II	P09668	Pro-cathepsin H	CTSH			0.4
III	P29508	Serpin B3	SERPINB3	1.0	1.0	1.0
III	Q6ZVX7	F-box only protein 50	NCCRP1	0.8	1.0	1.0
III	P22735	Protein-glutamine gamma-glutamyltransferase K	TGM1	1.0	1.0	0.8
III	P05089	Arginase-1	ARG1	1.0	1.0	1.0
III	P15309	Prostatic acid phosphatase (PAP)	ACPP	0.4		0.4
III	P20336	Ras-related protein Rab-3A	RAB3A	1.0	0.8	0.6
III	Q969L2	Protein MAL2	MAL2	0.4	0.8	0.4
III	Q92817	Envoplakin	EVPL		0.2	0.4
III	Q5TZA2	Rootletin	CROCC		0.2	0.2
III	Q9NSB4	Keratin, type II cuticular Hb2	KRT82		0.2	0.2
III	P20933	N(4)-(beta-N-acetylglucosaminy)-L-asparaginase	AGA			0.6
	Q96QA5	Gasdermin-A	GSDMA	1.0	1.0	1.0
	P42357	Histidine ammonia-lyase (Histidase)	HAL	0.8	0.8	1.0
	P22234	Multifunctional protein ADE2	PAICS	0.2		
	Q9C075	Keratin, type I cytoskeletal 23	KRT23	1.0	1.0	1.0
	O75635	Serpin B7	SERPINB7	1.0	1.0	1.0
	P25788	Proteasome subunit alpha type-3	PSMA3	0.4		0.2
	Q9UI42	Carboxypeptidase A4	CPA4	0.4	1.0	0.8
	P10619	Lysosomal protective protein	CTSA	0.4	0.4	0.6
	Q9NRW1	Ras-related protein Rab-6B	RAB6B	1.0	0.6	0.6
	Q6NUJ1	Proactivator polypeptide-like 1	PSAPL1	0.4	0.4	0.8
	Q9Y337	Kallikrein-5	KLK5 SCTE	1.0	0.8	0.6
	P20340	Ras-related protein Rab-6A (Rab-6)	RAB6A	1.0	0.8	0.6
	Q92820	Gamma-glutamyl hydrolase	GGH	0.4	0.6	0.6
	O95716	Ras-related protein Rab-3D	RAB3D	1.0	0.8	0.6
	O60911	Cathepsin L2	CTSV	0.4	0.4	1.0
	P20962	Parathymsin	PTMS	0.2		

Results and discussion

categ.	accession (UNIPROT)	protein description	gene name	1st	1st'	2nd
	Q8IW75	Serpin A12 (OL-64)	SERPINA12	0.8	1.0	1.0
	Q96P63	Serpin B12	SERPINB12	1.0	1.0	1.0
	Q5T750	Skin-specific protein 32	XP32	1.0	1.0	1.0
	Q8NEX9	Short-chain dehydrogenase/reductase family 9C member 7	SDR9C7	0.4	0.6	0.8
	O43240	Kallikrein-10	KLK10	0.4	0.4	0.4
	Q14533	Keratin, type II cuticular Hb1	KRT81	0.2	0.4	0.2
	P28074	Proteasome subunit beta type-5	PSMB5	0.4	0.8	0.8
	O00115	Deoxyribonuclease-2-alpha	DNASE2	0.2		0.2
	Q15102	Platelet-activating factor acetylhydrolase IB subunit gamma	PAFAH1B3	0.2		
	Q6P4A8	Phospholipase B-like 1	PLBD1	0.4		0.2
	P20337	Ras-related protein Rab-3B	RAB3B	1.0	0.8	0.6
	Q96E17	Ras-related protein Rab-3C	RAB3C	1.0	0.8	0.6
	Q9NSB2	Keratin, type II cuticular Hb4	KRT84	0.2	0.4	0.4
	Q9Y4F4	TOG array regulator of axonemal microtubules protein 1 (Crescerin-1)	TOGARAM1	0.2		
	Q9Y446	Plakophilin-3	PKP3		0.2	0.2
	P42285	Exosome RNA helicase MTR4	MTREX		0.2	
	Q14116	Interleukin-18 (IL-18)	IL18		0.2	0.4
	P13798	Acylamino-acid-releasing enzyme (AARE)	APEH		0.2	
	P55196	Afadin	AFDN		0.2	
	O95819	Mitogen-activated protein kinase kinase kinase 4	MAP4K4		0.2	
	P12081	Histidine--tRNA ligase, cytoplasmic	HARS		0.2	0.2
	Q9NNX1	Tuftelin	TUFT1		0.2	
	P49590	Probable histidine--tRNA ligase, mitochondrial	HARS2		0.2	0.2
	P48163	NADP-dependent malic enzyme (NADP-ME)	ME1		0.2	0.2
	Q5VVQ6	Ubiquitin thioesterase OTU1	YOD1		0.2	0.2
	A6NCN2	Putative keratin-87 protein	KRT87P		0.4	0.4
	O76009	Keratin, type I cuticular Ha3-I	KRT33A		0.4	
	O76011	Keratin, type I cuticular Ha4	KRT34		0.4	
	Q9C0C2	182 kDa tankyrase-1-binding protein	TNKS1BP1			0.2
	Q96JY6	PDZ and LIM domain protein 2	PDLIM2			0.2
	Q6NXG1	Epithelial splicing regulatory protein 1	ESRP1			0.2
	Q9BVK6	Transmembrane emp24 domain-containing protein 9 (GMP25)	TMED9			0.2

Results and discussion

categ.	accession (UNIPROT)	protein description	gene name	1st	1st'	2nd
	Q9P1U1	Actin-related protein 3B (ARP3-beta)	ACTR3B			0.2
	Q8IYT4	Katanin p60 ATPase-containing subunit A-like 2	KATNAL2			0.2
	Q9H6T0	Epithelial splicing regulatory protein 2	ESRP2			0.2
	P80108	Phosphatidylinositol-glycan-specific phospholipase D	GPLD1			0.2
	Q9C0K3	Actin-related protein 3C	ACTR3C			0.2
	Q9NR46	Endophilin-B2	SH3GLB2			0.2
	O95867	Lymphocyte antigen 6 complex locus protein G6c	LY6G6C			0.2
	P08842	Steryl-sulfatase	STS			0.2
	P14384	Carboxypeptidase M (CPM)	CPM			0.2
	Q9BYZ2	L-lactate dehydrogenase A-like 6B	LDHAL6B			0.2
	Q9HB40	Retinoid-inducible serine carboxypeptidase	SCPEP1			0.4

Comparing the identified proteins per replicate in each layer, it was noticeable that the most epidermal protein markers were identified in all layers (with a high reproducibility rate: 0.6 to 1.0). For determination of the ablation depth, each protein may be compared with existing database, which proves to be very time-consuming. The interpretation of the images obtained by the STRING data base allows a faster overview of related proteins due to their biological functions which can help to distinguish between the localization of proteins in the cell layers. However, the topographical organization of cells regarding the rete ridges patterns of skin makes the ablation of cells challenging. This was proved by the identification of dermal protein markers in each layer. Despite the fact, that the most identified proteins belong to the epidermis and gives the impression that the ablation was successfully done within the epidermal cells, there were some protein candidates from the dermis which prove the opposite. Due to the low number of identified dermal protein markers, it can be explained that the laser beams achieve the top of the dermal ridges. For distinction between epidermal cell layers and dermal area, a 3-dimensional navigation system has to be coupled to the PIRL to visualize the ablation area of interest and to avoid the ablation of dermis.

5 Conclusion and outlooks

The biological significance of the knowledge about the skin proteomes (in the existing five epidermal layers) is the main key for answering this durable organ and its regenerative function. This knowledge may lead to pathologies and therapeutic treatments. The overall aim of this study was to investigate and determine the skin proteomes by a layer-by-layer approach using mass spectrometric analysis and picosecond-infrared laser (PIRL) homogenization technique.

Due to the novelty of the PIRL system, a comparison of this homogenization technique to the existing classical homogenization techniques was required. Then a protein marker library for epidermis and dermis had to be generated. Therefore, a dispase treatment was used to separate the epidermal and dermal layers of skin. After optimization of several parameters of the PIRL system, it served as an ultrafast homogenization method with a reduce risk of contamination, as expected. Additionally, this study demonstrated that the obtained proteome data of PIRL resulting in higher reproducibility rates and better protein recoveries. One finding of interest was the optimization of the extraction protocol with SDC and urea combined for a better solubility and denaturization of more proteins fixed on the top of borosilicate filter paper. One further finding was the distinction between the breast and abdominal tissue with the aid of existing mass spectrometric proteome data for both where six epidermal protein markers were identified exclusively in breast tissues. The layer-by-layer approach of skin cell layers was conducted by using PIRL method, which enabled an ablation depth of 15 μm per scan within 7 seconds.

Taken together, the results of these studies provide support for the conclusion that with PIRL ablation, epidermal cell layers could be ablated, and the proteins of each ablated layer was identified by using tandem mass spectrometry with a bottom-up approach.

In this study, skin proteomics emphasizes a non-presumptive characterization as well as determination of high dynamic range of proteomes in comparison to the histochemical structure characterization techniques. This study allowed to identify a huge number of proteomes of skin main layers (dermis and epidermis) as well as the epidermal cell layers, while the histochemical characterization techniques require prohibitive-costly and time-consuming approaches. Nevertheless, the PIRL ablation of skin cell layers is challenging due to not only the rete ridges structure of skin [53] and the different thickness of different cell types, but also the missing information about the depth of epidermal layer, which varies depending

on diverse factors from individuum to individuum: area in the human body, age, nutrition, environmental stress, etc. Due to the fact that the stratum corneum is composed of dead cells, stratum spinosum, granulosum and basale are composed of living cells and the basal membrane built the thinnest layer with 100 nm [1, 6], and additionally the topographically organization of these cells due to the rete ridges pattern of epidermis, they all constrain the use of PIRL ablation. Therefore, an online guiding of laser irradiation during the ablation is required. It is recommended that the PIRL ablation may be connected to an optical coherence tomography (OCT) device. The OCT enables a rapid 3-dimensional endoscopic navigation of tissue and provides an online tracking of the laser beams through the skin main layers (dermis and epidermis) [98-100]. In the next studies in the working group of PROF. DR. H. SCHLÜTER the investigation of skin tissues with OCT imaging will follow.

6 References

- [1] Rinnerthaler M, Streubel MK, Bischof J, Richter K. Skin aging gene expression and calcium. *Experimental Gerontology* **2015**, Volume 68, Pages 59-65.
- [2] Huang CM, Xu H, Wang CC, Elmets CA. Proteomic characterization of skin and epidermis in response to environmental agents. *Expert Review of Proteomics* **2005**, Volume 2, Issue 5, 809-820.
- [3] Bliss E, Heywood WE, Benatti M, Sebire NJ, Mills. An optimised method for the proteomic profiling of full thickness human skin. *Biological Procedures Online* **2016**,18:15.
- [4] de Veer SJ, Furio L, Harris JM, Hovnanian A. Proteases and proteomics: cutting to the core of human skin pathologies. *Proteomics Clin Appl.* **2014**; 8(5-6):389-402.
- [5] Hashmi S, Marinkovich MP. Molecular organization of the basement membrane zone. *Clin Dermatol.* **2011**, 29(4):398-411.
- [6] Mikesh LM, Aramadhaka LR, Moskaluk C, Zigrino P, Mauch C, Fox JW. Proteomic anatomy of human skin. *J Proteomics.* **2013**, 12;84:190-200.
- [7] Malissen B, Tamoutounour S, Henri S. The origins and functions of dendritic cells and macrophages in the skin. *Nat Rev Immunol.* **2014**; 14(6):417-28.
- [8] Oikarinen A. Aging of the skin connective tissue: How to measure the biochemical and mechanical properties of aging dermis. *Photodermatol Photoimmunol Photomed.* **1994**, 10(2):47-52.
- [9] Shoulders MD, Raines RT. Collagen structure and stability. *Annu Rev Biochem.* **2009**, 78:929-58.
- [10] Winget JM, Watts JD, Hoopmann MR, DiColandrea T, Robinson MK, Huggins T, Bascom CC, Isfort RJ, Moritz RL. Quantitative proteogenomic profiling of epidermal barrier formation in vitro. *J Dermatol Sci.* **2015**, 78(3):173-80.
- [11] Candi E, Schmidt R, Melino G. The cornified envelope: a model of cell death in the skin. *Nat Rev Mol Cell Biol.* **2005**, 6(4):328-40.
- [12] Sturgeon D. Introduction to Anatomy and Physiology for Healthcare Students. *Verlag: Routledge*; 1st edition, Oxon, **2018**.
- [13] Klein AM, Nikolaidou-Neokosmidou V, Doupé DP, Jones PH, Simons BD. Patterning as a signature of human epidermal stem cell regulation. *J R Soc Interface.* **2011**, 8(65):1815-24.
- [14] Zelenin AV, Rodionov AV, Bolsheva NL, Badaeva ED, Muravenko OV. Genome: Origins and Evolution of the Term. *Molecular Biology* **2016**, Volume 50, Issue 4, pp 542-55.

- [15] Wilkins MR, Williams K, Appel R, Hochstrasser D. Proteome Research: New Frontiers in Functional Genomics. *Springer Verlag*, Berlin, **1997**, P. 1.
- [16] Mueller M, Martens L, Apweiler R. Annotation the human proteome: beyond establishing a parts list. *Biochim Biophys Acta* **2007**, 1774, (2), 175-191.
- [17] Schlüter H, Apweiler R, Holzhütter HG, Jungblut PR. Finding one's way in proteomics: a protein species nomenclature. *Chemistry Central Journal* **2009**, 3(1):11.
- [18] Jungblut P, Thiede B, Zimny-Arndt U, Muller EC, Scheler C, Wittmann-Liebold B, Otto A. Resolution power of two-dimensional electrophoresis and identification of proteins from gels. *Electrophoresis* **1996**, 17, 839-847.
- [19] Kelleher NL. A cell-based approach to the human proteome project. *J Am Soc Mass Spectrom.* **2012**; 23(10): 1617-1624.
- [20] Jungblut PR, Holzhütter HG, Apweiler R, Schlüter H. The Speciation of the Proteome. *Chem Cent J* **2008**, 2:16.
- [21] Edited by Coelho AV, Ferraz Franco CM. Tandem Mass Spectrometry - Molecular Characterization. Published by *InTech*, **2013**.
- [22] Padula MP, Berry IJ, O'Rourke MB, Raymond BBA, Santos J, Djordjevic SP. A Comprehensive Guide for Performing Sample Preparation and Top-Down Protein Analysis. *Proteomes* **2017**, 5(2), 11.
- [23] Zhang Y, Fonslow BR, Shan B, Baek MC, Yates JR. Protein Analysis by Shotgun/Bottom-up Proteomics. *Chem. Rev.* **2013**, 113, 2343-2394
- [24] Lipton MS, Paša-Tolić L. Mass Spectrometry of Proteins and Peptides, Methods and Protocols. Second Edition, Pacific Northwest National Laboratory, Richland, WA, USA, *Humana Press* **2009**.
- [25] Patwardhan BK, Chaguturu R. Innovative Approaches in Drug Discovery Ethnopharmacology, Systems Biology and Holistic Targeting. Edition: 1st Publisher: Academic Press ELSEVIER **2017**, Chapter 9: proteomics, Pages 273-294.
- [26] Ali I, Aboul-Enein HY, Singh P, Singh R, Sharma B. Separation of biological proteins by liquid chromatography. *Saudi Pharmaceutical Journal* **2010**, 18,59-73.
- [27] Garfin D, Ahuja S. Handbook of Isoelectric Focusing and Proteomics. Volume 7, Pages 1-334, *Elsevier* **2005**.
- [28] Chait BT. Mass Spectrometry _ Bottom-Up or Top-Down? *Science* **2006**, Vol. 314, Issue 5796, pp. 65-66.
- [29] Meier F, Geyer PE, Winter SV, Cox J, Mann M. BoxCar acquisition method enables single-shot proteomics at a depth of 10,000 proteins in 100 minutes. *Nat Methods.* **2018**, 15(6):440-448.

- [30] Krisp C, McKay MJ, Wolters DA, Molloy MP. Multidimensional Protein Identification Technology-Selected Reaction Monitoring Improving Detection and Quantification for Protein Biomarker Studies. *Anal. Chem.* **2012**, 84, 1592-1600.
- [31] Chandramouli K, Qian PY. Proteomics: Challenges, Techniques and Possibilities to Overcome Biological Sample Complexity. *Human Genomics and Proteomics* **2009** Volume, Article ID 239204.
- [32] Burden DW. Guide to the Homogenization of Biological Samples. *Random Primers* **2012** Issue No., Page 1-25.
- [33] Graham, JM, Rickwood D. Homogenization of tissues and cells, Subcellular Fractionation: A Practical Approach. *Oxford University Press*, **1997** (173): p. p. 12ff.
- [34] QIAGEN®, TissueLyser II, www.qiagen.com (access in June **2018**).
- [35] Franjic K, Cowan ML, Kraemer D, Miller DRJ. Laser selective cutting of biological tissues by impulsive heat deposition through ultrafast vibrational excitations. *Optics express* **2009**. 17(25), pp. 22937-22959.
- [36] Böttcher A, Clauditz TS, Knecht R, Kucher S, Wöllmer W, Wilczak W, Krötz P, Jowett N, Dalchow CV, Münscher A, Miller RJ. A Novel Tool in Laryngeal Surgery: Preliminary Results of the Picosecond Infrared Laser. *Laryngoscope.* **2013**, 123(11):2770-5.
- [37] Peng Q, Juzeniene A, Chen J, Svaasand LO, Warloe T, Giercksky KE, Moan J. Lasers in medicine. *Reports on Progress in Physics*, **2008**, Volume 71, Number 5.
- [38] Petersen J, Møller KB, Rey R, Hynes JT. Ultrafast Librational Relaxation of H₂O in Liquid Water. *Phys. Chem. B*, **2013**, 117 (16), pp 4541-4552.
- [39] Imoto S, Xantheas SS, Saito S. Ultrafast Dynamics of Liquid Water: Energy Relaxation and Transfer Processes of the OH Stretch and the HOH Bend. *J. Phys. Chem. B*, **2015**, 119 (34), pp 11068-11078.
- [40] Jowett N, Wöllmer W, Mlynarek AM, Wiseman P, Segal B, Franjic K, Krötz P, Böttcher A, Knecht R, Miller RJ. Heat Generation During Ablation of Porcine Skin With Erbium:YAG Laser vs a Novel Picosecond Infrared Laser. *JAMA Otolaryngol Head Neck Surg.* **2013**; 139(8):828-33.
- [41] Kwiatkowski M, Wurlitzer M, Krutilin A, Kiani P, Nimer R, Omid M, Mannaa A, Bussmann T, Bartkowiak K, Kruber S, Uschold S, Steffen P, Lübberstedt J, Küpker N, Petersen H, Knecht R, Hansen NO, Zarrine-Afsar A, Robertson WD, Miller RJD, Schlüter H. Homogenization of tissues via picosecond-infrared laser (PIRL) ablation: Giving a closer view on the in-vivo composition of protein species as compared to mechanical homogenization. *Journal of Proteomics* **2016**, 134, 193-202.
- [42] Linke SJ, Frings A, Ren L, Gomolka A, Schumacher U, Reimer R, Hansen NO, Jowett N, Richard G, Miller RJ. A New Technology for Applanation Free Corneal Trephination: The Picosecond Infrared Laser (PIRL). *PLoS One.* **2015**. 10(3).

- [43] Hess M, Hildebrandt MD, Müller F, Kruber S, Kroetz P, Schumacher U, Reimer R, Kammal M, Püschel K, Wöllmer W, Miller D. Picosecond infrared laser (PIRL): an ideal phonomicrosurgical laser? *Eur Arch Otorhinolaryngol.* **2013**; 270(11):2927-37.
- [44] Böttcher A, Kucher S, Knecht R, Jowett N, Krötz P, Reimer R, Schumacher U, Anders S, Münscher A, Dalchow CV, Miller RJD. Reduction of thermocoagulative injury via use of a picosecond infrared laser (PIRL) in laryngeal tissues. *Eur Arch Otorhinolaryngol* **2015** 272:941-948.
- [45] Petersen H, Tavakoli F, Kruber S, Münscher A, Gliese A, Hansen NO, Uschold S, Eggert D, Robertson WD, Gosau T, Sehner S, Kwiatkowski M, Schlüter H, Schumacher U, Knecht R, Miller RJ. Comparative study of wound healing in rat skin following incision with a novel picosecond infrared laser (PIRL) and different surgical modalities. *Lasers Surg Med.* **2016**; 48(4):385-91.
- [46] Jowett N, Wöllmer W, Reimer R, Zustin J, Schumacher U, Wiseman PW, Mlynarek AM, Böttcher A, Dalchow CV, Lörincz BB, Knecht R, Miller RJ. Bone ablation without thermal or acoustic mechanical injury via a novel picosecond infrared laser (PIRL). *Otolaryngol Head Neck Surg.* **2014**; 150(3):385-93.
- [47] Kwiatkowski M, Wurlitzer M, Omid M, Ren L, Kruber S, Nimer R, Robertson WD, Horst A, Miller RJ, Schlüter H. Ultrafast extraction of proteins from tissues using desorption by impulsive vibrational excitation. *Angew Chem Int Ed Engl.* **2015**; 54(1):285-8.
- [48] <http://www.derm-hokudai.jp/shimizu-dermatology/pdf/01-05.pdf> (access in Aug 2018).
- [49] <https://www.earthslab.com/physiology/cells-layers-epidermis/> (access in Aug 2018).
- [50] Dyroff C, Tunable Diode-Laser Absorption Spectroscopy for Trace-Gas Measurements with High Sensitivity and Low Drift, Ph.D. thesis, University of Karlsruhe, ISBN: 978-3-86644-328-0, available at: <http://digbib.ubka.uni-karlsruhe.de/volltexte/1000010030>, 2009.
- [51] Ashihara S, Huse N, Espagne A, Nibbering ET, Elsaesser T. Ultrafast structural dynamics of water induced by dissipation of vibrational energy. *J Phys Chem A.* **2007**; 111(5):743-6.
- [52] Fein H, Maytin EV, Mutasim DF, Bailin PL. Topical protease therapy as a novel method of epidermal ablation: preliminary report. *Dermatol Surg.* **2005**; 31(2):139-48.
- [53] Kitano Y, Okada N. Separation of the epidermal sheet by dispase. *Br J Dermatol.* **1983**; 108(5):555-60.
- [54] Stenn KS, Link R, Moellmann G, Madri J, Kuklinska E. Dispase, a neutral protease from *Bacillus polymyxa*, is a powerful fibronectinase and type IV collagenase. *J Invest Dermatol.* **1989**; 93(2):287-90.

- [55] Scheerlinck E, Dhaenens M, Van Soom A, Peelman L, De Sutter P, Van Steendam K, Deforce D. Minimizing technical variation during sample preparation prior to label-free quantitative mass spectrometry. *Anal Biochem.* **2015**; 490:14-9.
- [56] León IR, Schwämmle V, Jensen ON, Sprenger RR. Quantitative assessment of in-solution digestion efficiency identifies optimal protocols for unbiased protein analysis. *Mol Cell Proteomics.* **2013**; 12(10):2992-3005.
- [57] Glatter T, Ahrné E, Schmidt A. Comparison of Different Sample Preparation Protocols Reveals Lysis Buffer-Specific Extraction Biases in Gram-Negative Bacteria and Human Cells. *J Proteome Res.* **2015**; 14(11):4472-85.
- [58] Krisp C, Yang H, van Soest R, Molloy MP. Online Peptide fractionation using a multiphasic microfluidic liquid chromatography chip improves reproducibility and detection limits for quantitation in discovery and targeted proteomics. *Mol Cell Proteomics.* **2015**; 14(6):1708-19.
- [59] User guide: Pierce BCA Protein Assay Kit., Thermo Scientific™.
- [60] Wiśniewski JR, Zougman A, Nagaraj N, Mann M. Universal sample preparation method for proteome analysis. *Nat Methods.* **2009**; 6(5):359-62.
- [61] Henry H, Meirelles GV, da Silva FR, Telles GP, Minghim R. InteractiVenn: a web-based tool for the analysis of sets through Venn diagrams. *BMC Bioinformatics.* **2015**; 16(1): 169.
- [62] Hulsen T, de Vlieg J, Alkema W. BioVenn – a web application for the comparison and visualization of biological lists using area-proportional Venn diagrams. *BMC Genomics.* **2008**; 9: 488.
- [63] Mi H, Huang X, Muruganujan A, Tang H, Mills C, Kang D, Thomas PD. PANTHER version 11: expanded annotation data from Gene Ontology and Reactome pathways, and data analysis tool enhancements. *Nucl. Acids Res.* **2016**, 45 (D1), D183-D189.
- [64] Oliveros JC. (2007-2015) Venny. An interactive tool for comparing lists with Venn's diagrams. <http://bioinfogp.cnb.csic.es/tools/venny/index.html>
- [65] Huang DW, Sherman BT, Lempicki RA. Systematic and integrative analysis of large gene lists using DAVID Bioinformatics Resources. *Nature Protoc.* **2009**; 4(1):44-57. DAVID Bioinformatics Resources 6.8, The DAVID “Database for Annotation, Visualization and Integrated Discovery, a Gene Functional Classification Tool.
- [66] Haque MA, Adhikari B. Chapter 49: Drying and Denaturation of Proteins in Spray Drying Process Handbook of Industrial Drying © 2015 by Taylor & Francis Group, LLC.
- [67] The Human Protein Atlas, <https://www.proteinatlas.org/humanproteome/skin> (access in 2018).
- [68] The Human Protein Atlas, Immunohistochemical image of SDR16C5; <https://www.proteinatlas.org/ENSG00000170786-SDR16C5/tissue/skin> (access in 2018).

- [69] Olink Proteomics, Protein marker Discovery, <https://www.olink.com/> (access in 2018).
- [70] Chopra K, Calva D, Sosin M, Tadisina KK, Banda A, De La Cruz C, Chaudhry MR, Legesse T, Drachenberg CB, Manson PN, Christy MR. A comprehensive examination of topographic thickness of skin in the human face. *Aesthet Surg J.* **2015**; 35(8):1007-13
- [71] UniProt: the universal protein knowledgebase; *Nucleic Acids Res.* **2017** 45: D158-D169, <https://www.uniprot.org/>
- [72] Pappas A. Epidermal surface lipids. *Dermatoendocrinol.* **2009**; 1(2): 72–76.
- [73] Szklarczyk D, Franceschini A, Wyder S, Forslund K, Heller D, Huerta-Cepas J, Simonovic M, Roth A, Santos A, Tsafou KP, Kuhn M, Bork P, Jensen LJ, von Mering C. STRING v10: protein-protein interaction networks, integrated over the tree of life. *Nucleic Acids Res.* **2015**; 43(Database issue) D447-52.
- [74] PubMed - National Center for Biotechnology Information (US), Bethesda (MD): National Center for Biotechnology Information (US); **2005**.
- [75] Koscielny G, An P, Carvalho-Silva D, Cham JA, Fumis L, Gasparyan R, Hasan S, Karamanis N, Maguire M, Papa E, Pierleoni A, Pignatelli M, Platt T, Rowland F, Wankar P, Bento AP, Burdett T, Fabregat A, Forbes S, Gaulton A, Gonzalez CY, Hermjakob H, Hersey A, Jupe S, Kafkas Ş, Keays M, Leroy C, Lopez FJ, Magarinos MP, Malone J, McEntyre J, Munoz-Pomer Fuentes A, O'Donovan C, Papatheodorou I, Parkinson H, Palka B, Paschall J, Petryszak R, Pratanwanich N, Sarntivijal S, Saunders G, Sidiropoulos K, Smith T, Sondka Z, Stegle O, Tang YA, Turner E, Vaughan B, Vrousitou O, Watkins X, Martin MJ, Sanseau P, Vamathevan J, Birney E, Barrett J, Dunham I. Open Targets: a platform for therapeutic target identification and validation. *Nucleic Acids Res.* 2017; 45(D1): D985-D994.
<https://www.targetvalidation.org/target/ENSG00000136155/associations>
- [76] Leclerc EA, Hucheno A, Kezic S, Serre G, Jonca N. Mice deficient for the epidermal dermokine β and γ isoforms display transient cornification defects. *J Cell Sci.* **2014**, 1;127(Pt 13):2862-72.
- [77] The Human Protein Atlas, Immunohistochemical image of DMKN; https://www.proteinatlas.org/ENSG00000161249-DMKN/tissue/skin+1#imid_8194936 (access in 2018).
- [78] Tartaglia-Polcini A, Bonnart C, Micheloni A, Cianfarani F, Andrè A, Zambruno G, Hovnanian A, D'Alessio M. SPINK5, the defective gene in netherton syndrome, encodes multiple LEKTI isoforms derived from alternative pre-mRNA processing. *J Invest Dermatol.* **2006**; 126(2):315-24.
- [79] Ishida-Yamamoto A, Deraison C, Bonnart C, Bitoun E, Robinson R, O'Brien TJ, Wakamatsu K, Ohtsubo S, Takahashi H, Hashimoto Y, Dopping-Hepenstal PJ, McGrath JA, Iizuka H, Richard G, Hovnanian A. LEKTI is localized in lamellar granules, separated

- from KLK5 and KLK7, and is secreted in the extracellular spaces of the superficial stratum granulosum. *J Invest Dermatol.* **2005**; 124(2):360-6.
- [80] The Human Protein Atlas, Immunohistochemical image of SPINK5; https://www.proteinatlas.org/ENSG00000133710-SPINK5/tissue/skin+1#imid_3141700 (access in 2018).
- [81] Tsuchida S, Bonkobara M, McMillan JR, Akiyama M, Yudate T, Aragane Y, Tezuka T, Shimizu H, Cruz PD Jr, Ariizumi K. Characterization of Kdap, a Protein Secreted by Keratinocytes. *J Invest Dermatol.* **2004**; 122(5):1225-34.
- [82] Edqvist PH, Fagerberg L, Hallström BM, Danielsson A, Edlund K, Uhlén M, Pontén F. Expression of human skin-specific genes defined by transcriptomics and antibody-based profiling. *J Histochem Cytochem.* **2015**; 63(2):129-41.
- [83] Bazzi H, Fantauzzo KA, Richardson GD, Jahoda CA, Christiano AM. Transcriptional profiling of developing mouse epidermis reveals novel patterns of coordinated gene expression. *Dev Dyn.* **2007**; 236(4):961-70.
- [84] The Human Protein Atlas, Immunohistochemical image of KRTDAP; <https://www.proteinatlas.org/ENSG00000188508-KRTDAP/tissue/skin> (access in 2018).
- [85] The Human Protein Atlas, Immunohistochemical image of SCEL; https://www.proteinatlas.org/ENSG00000136155-SCEL/tissue#gene_information (access in 2018).
- [86] Baden HP, Champliand MF, Sundberg JP, Viel A. Targeted deletion of the sciellin gene resulted in normal development and maturation. *Genesis.* **2005**; 42(4):219-28.
- [87] The Human Protein Atlas, Immunohistochemical image of SERPINB4; [https://www.proteinatlas.org/ENSG00000206073-SERPINB4/tissue/skin skin](https://www.proteinatlas.org/ENSG00000206073-SERPINB4/tissue/skin%20skin) (access in 2018).
- [88] Barrandon Y, Green H. Cell size as a determinant of the clone-forming ability of human keratinocytes. *Proc Natl Acad Sci U S A.* **1985**; 82(16):5390-4.
- [89] Sun TT, Green H. Differentiation of the epidermal keratinocyte in cell culture: Formation of the cornified envelope. *Cell.* **1976**; 9(4 Pt 1):511-21.
- [90] Ginzberg MB, Kafri R, Kirschner M. On being the right (cell) size. *Science.* **2015** 15; 348(6236): 1245075.
- [91] Roberts DJ, Waelbroeck M. G protein activation by G protein coupled receptors: ternary complex formation or catalyzed reaction? *Biochem Pharmacol.* **2004**; 68(5):799-806.
- [92] Moll R, Divo M, Langbein L. The human keratins: biology and pathology. *Histochem Cell Biol.* **2008**; 129(6): 705-733.
- [93] Ishida-Yamamoto A, Takahashi H, Iizuka H. Loricrin and human skin diseases: molecular basis of loricrin keratodermas. *Histol Histopathol.* **1998**; 13(3):819-26.

- [94] de Juanes S, Epp N, Latzko S, Neumann M, Fürstenberger G, Hausser I, Stark HJ, Krieg P. Development of an ichthyosiform phenotype in Alox12b-deficient mouse skin transplants. *J Invest Dermatol.* **2009**; 129(6):1429-36.
- [95] Jobard F, Lefèvre C, Karaduman A, Blanchet-Bardon C, Emre S, Weissenbach J, Ozgüc M, Lathrop M, Prud'homme JF, Fischer J. Lipoxygenase-3 (ALOXE3) and 12(R)-lipoxygenase (ALOX12B) are mutated in non-bullous congenital ichthyosiform erythroderma (NCIE) linked to chromosome 17p13.1. *Hum Mol Genet.* **2002**; 11(1):107-13.
- [96] Whitaker S. Introduction to Fluid Mechanics. Englewood Cliffs, N.J.: Prentice-Hall, **1968**.
- [97] Evans ND, Oreffo RO, Healy E, Thurner PJ, Man YH. Epithelial mechanobiology, skin wound healing, and the stem cell niche. *J Mech Behav Biomed Mater.* **2013**; 28:397-409.
- [98] Hariri LP, Adams DC, Wain JC, Lanuti M, Muniappan A, Sharma A, Colby TV, Mino-Kenudson M, Mark EJ, Kradin RL, Goulart H, Tager AM, Suter MJ. Endobronchial Optical Coherence Tomography for Low-Risk Microscopic Assessment and Diagnosis of Idiopathic Pulmonary Fibrosis In Vivo. *Am J Respir Crit Care Med.* **2018**; 197(7):949-952.
- [99] Zhuo S, Chen J, Luo T, Zou D. Multimode nonlinear optical imaging of the dermis in ex vivo human skin based on the combination of multichannel mode and Lambda mode. Optical Society of America, *Opt Express.* **2006**; 14(17):7810-20.
- [100] Farage MA, Miller KW, Elsner P, Maibach HI. Structural characteristics of the aging skin: a review. *Cutan Ocul Toxicol.* **2007**; 26(4):343-57.
- [101] <http://www.dguv.de/ifa/Gefahrstoffdatenbanken>, GESTIS-Stoffdatenbank (access in Jul 2018).
- [102] <http://www.sigmaaldrich.com>, Sigma-Aldrich-Products (access in Jul 2018).
- [103] Tschachler E, Reinisch CM, Mayer C, Paiha K, Lassmann H, Weninger W. Sheet preparations expose the dermal nerve plexus of human skin and render the dermal nerve end organ accessible to extensive analysis. *J Invest Dermatol.* **2004**; 122(1):177-82.

7 Risk and safety statements

Table 23: Safety and Disposal [91]. Pictograms based on GHS (Globally Harmonized System of Classification and Labelling of Chemicals), GHS hazard and precautionary statements.

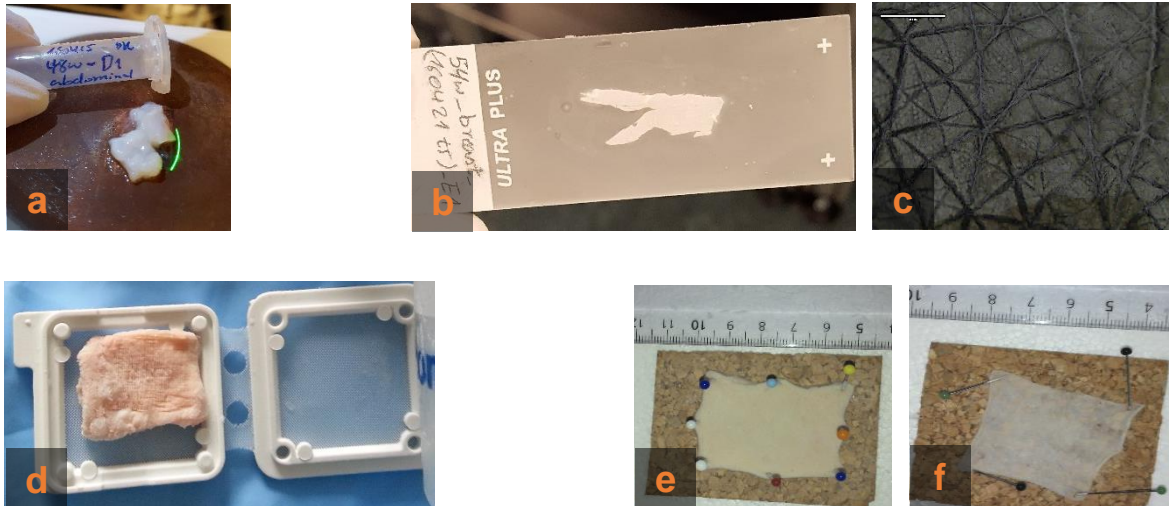
Chemicals	GHS Symbols	GHS hazard statements	GHS precautionary statements	Disposal key
acetitrile (Li-Chrosolv®)	GHS02  GHS07 	H225 H332 H302 H312 H319	P210 P240 P302+P352 P305+P351+P338 P403+P233	1
acidic acid	GHS05 	H226 H290 H314	P210 P280 P301+P330+P331 P305+P351+P338 P308+P310	5
ammonium bicarbonate	GHS07 	H302	P301+P312 P330	2
dithiotreitol	GHS07 	H302 H315 H319 H335	P261 P305+P351+P338	2
eosin	GHS07 	H319	P260 P305+P351+P338	1
formic acid	GHS02  GHS05  GHS06 	H226 H302 H314 H331 EUH071	P210 P280 P303+P361+P353 P304+P340+P310 P305+P351+P338 P403+P233	5
haematoxylin	GHS07 	H302 H315 H319 H335	P261 P305+P351+P338	1

Risk and safety statements

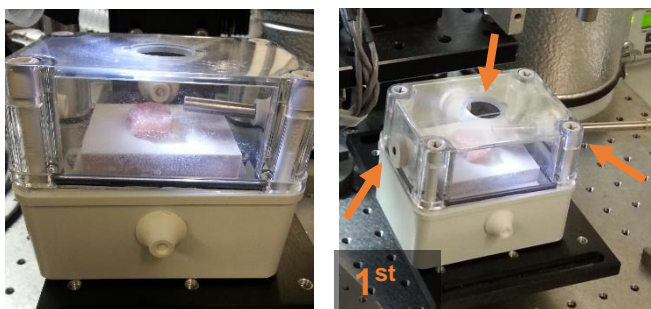
Chemicals	GHS Symbols	GHS hazard statements	GHS precautionary statements	Disposal key
iodoacetamide	GHS06  GHS08 	H301 H317 H334 H413	P261 P280 P301 + P310 P342 + P311	2
methanol (Li-Chrosolv®)	GHS02  GHS06  GHS08 	H225 H331 H311 H301 H370	P210 P233 P280 P302+P352 P304+P340 P308+P310 P403+P235	1
phosphoric acid	GHS05 	H314 H290	P280 P301+P330+P331 P305+P351+P338 P309+P310	5
sodium deoxycholate	GHS07 	H302	P301+P312+P330 P330	2
trypsin	GHS07  GHS08 	H315 H319 H334 H335	P261 P280 P284 P304+P340 P337+P313 P342+P311	3
urea	No hazardous substance or mixture according to GHS			2

- 1: Disposal in canister for halogen-free organic solvents
- 2: Disposal in canister for salt-containing solvents, pH set to 6-8
- 3: Biomaterials were collected in a collection-container for autoclavation
- 4: Disposal in canister for bases
- 5: Disposal in canister for acids

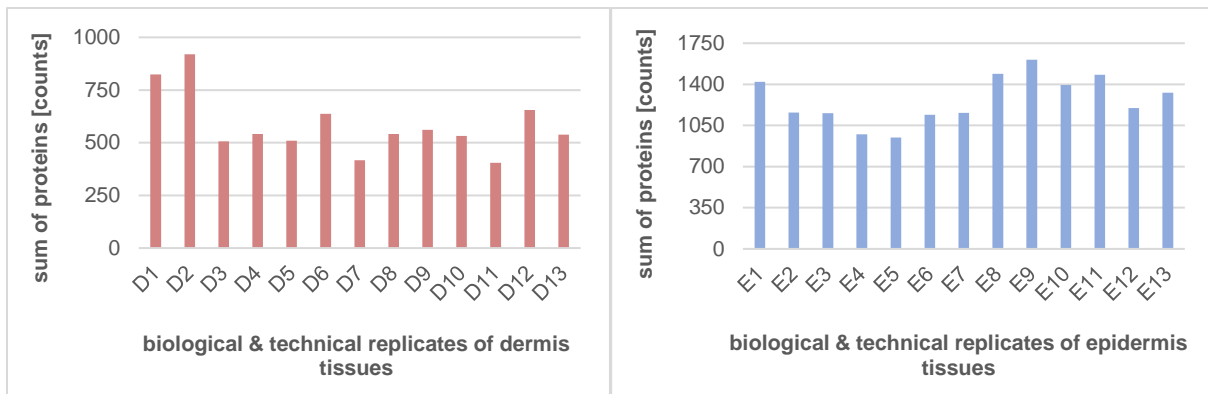
8 Supplement



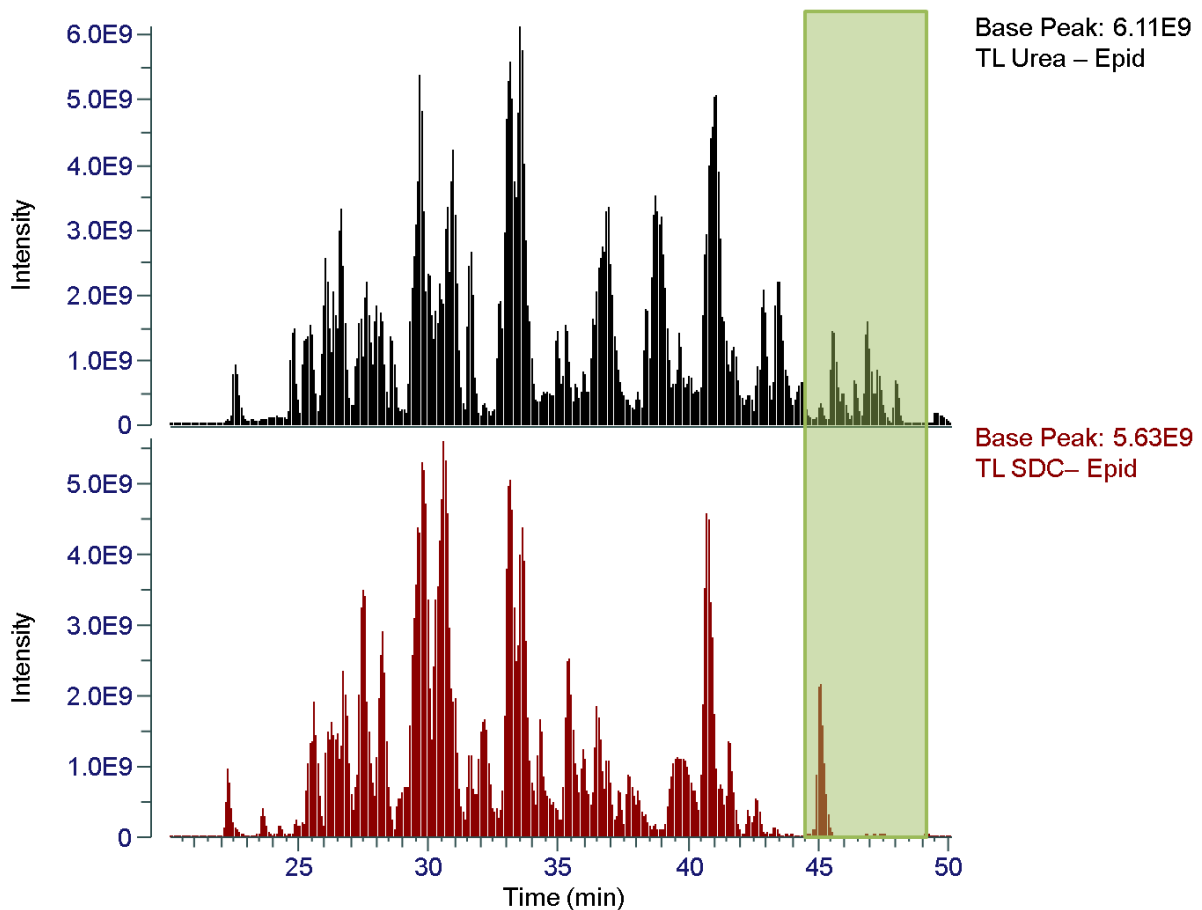
S. 1: Prepared skin samples prior to PIRL ablation or classical homogenization. *a*: frozen, dispase-separated dermis tissue; *b*: frozen, dispase-separated epidermis tissue on glass slide; *c*: light microscopic top view of dispase-separated epidermis tissue on glass slide (scale range 400 µm); *d*: frozen, human skin tissue in biopsy capsules; *e*: fresh skin biopsy fixed on the top of cork plate with pins; *f*: fresh skin biopsy cut by using dermatome 200 µm thick fixed on the top of cork plate with pins.



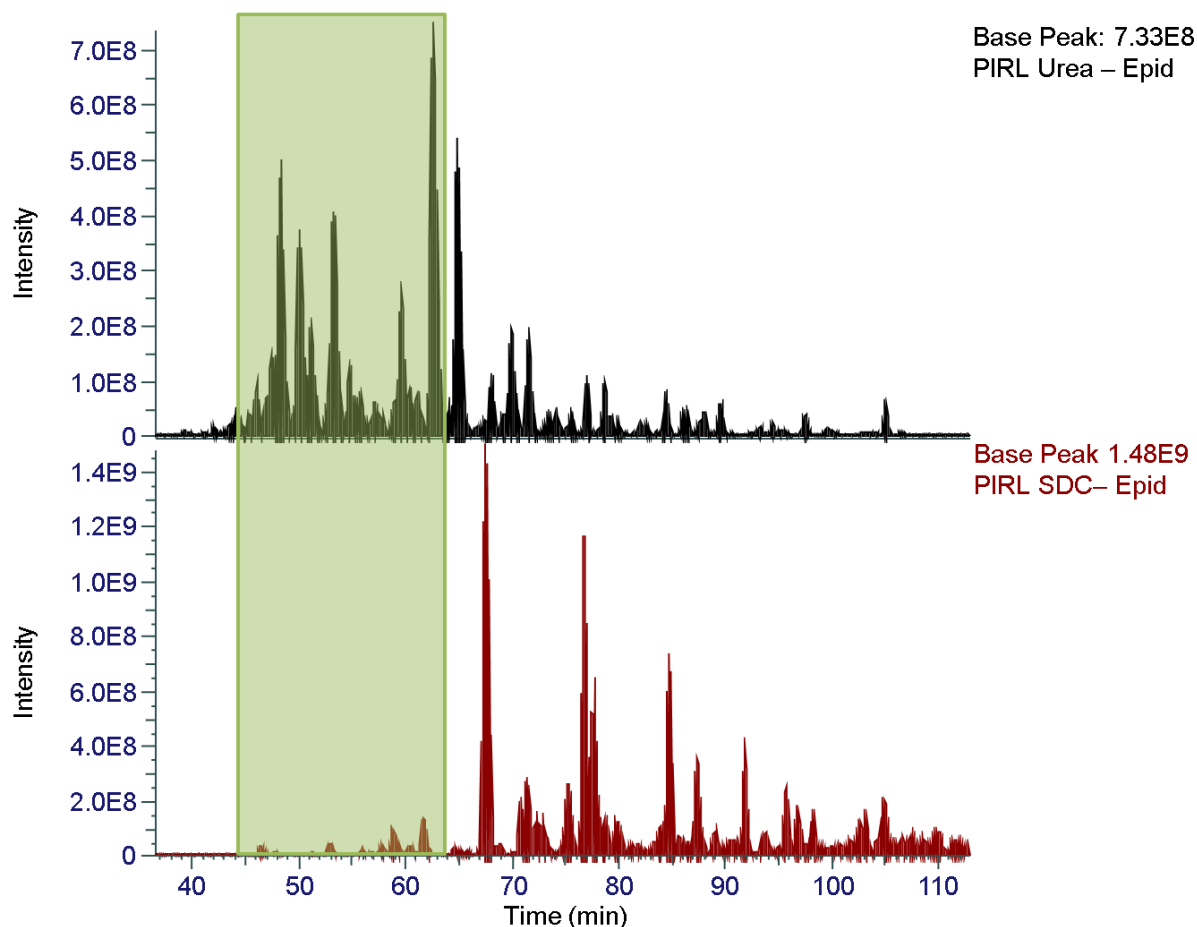
S. 2: Two images of the 1st chamber generation. A semi-closed system with three opened orifices (shown with orange arrows), one on the top of the chamber for letting through the laser irradiation to the targeted sample, another one for controlled air permeable dynamic and the third one for vacuum tubing system to draw the aerosol in the sample trap.



S. 3: Comparison of protein yields of two different type skin tissues homogenized by TissueLyser (TL) with biological and technical replicates (up to seven sample donors different ages). Left: achieved protein yields of dermis tissues; right: achieved protein yields of epidermis tissues.



S. 4: Exemplary comparison of Base peak chromatogram (full MS) of epidermal samples homogenized by TissueLyser (TL) and extracted with urea and SDC. The green part visualizes the missing signals in case of SDC extracted sample compared to the urea extracted sample.



S. 5: Exemplary comparison of Base peak chromatogram (full MS) of epidermal samples homogenized by PIRL and extracted with urea and SDC. The green part visualizes the missing signals in case of SDC extracted sample compared to the urea extracted sample.

S. 6: Protein marker library for epidermis (319 proteins). The following information are listed: categories I (high), II (medium) and III (low), protein description, gene names, accession (UNIPROT accession numbers) and molecular weight (MW in kDa). The proteins in each category are listed descending order due to their numbers of detected unique peptides.

category	protein description	gene name	accession (UniProt)	MW [kDa]
I	Alpha-2-macroglobulin-like protein 1	A2ML1	A8K2U0	181.7
I	Sciellin	SCEL	O95171	35.9
I	Zinc finger protein 185	ZNF185	O15231	138.3
I	Dermokine	DMKN	Q6E0U4	81.8

category	protein description	gene name	accession (UniProt)	MW [kDa]
	T-complex protein 1 subunit eta	CCT7	Q99832	73.3
	Serine protease inhibitor Kazal-type 5	SPINK5	Q9NQ38	11.6
	Prostaglandin G/H synthase 1	PTGS1	P23219	88.8
	Serpin B4	SERPINB4	P48594	23.8
	FACT complex subunit SSRP1	SSRP1	Q08945	23.7
	Epidermal retinol dehydrogenase 2	SDR16C5	Q8N3Y7	11.7
	Keratinocyte differentiation-associated protein	KRTDAP	P60985	24.7
	60S ribosomal protein L35	RPL35	P42766	46.4
	Phosphatidylinositol transfer protein beta isoform	PITPNB	P48739	21.4
	Ankyrin repeat domain-containing protein 35	ANKRD35	Q8N283	29.2
	Eukaryotic translation initiation factor 3 subunit K	EIF3K	Q9UBQ5	28.9
	Poly(U)-specific endoribonuclease	ENDOOU	P21128	16.4
	40S ribosomal protein S4. Y isoform 1	RPS4Y1	P22090	26.2
	Serine/threonine-protein phosphatase 2A 55 kDa regulatory subunit B alpha isoform	PPP2R2A	P63151	89.4
	Serine/arginine-rich splicing factor 9	SRSF9	Q13242	51.8
	Protein S100-A7A	S100A7A	Q86SG5	39.6
	Nucleolar RNA helicase 2	DDX21	Q9NR30	32.0
	Nucleolar protein 3	NOL3	O60936	110.4
	Glucosylceramidase	GBA	P04062	20.0
	Desmocollin-2	DSC2	Q02487	83.7
	Eukaryotic translation initiation factor 3 subunit G	EIF3G	O75821	61.7
	Phosphatidylinositol transfer protein alpha isoform	PITPNA	Q00169	119.3
	Protein FAM83B	FAM83B	Q5T0W9	48.9
	Tumor susceptibility gene 101 protein	TSG101	Q99816	17.7
	Specifically androgen-regulated gene protein	SARG	Q9BW04	22.4
	Protein FAM49B	FAM49B	Q9NUQ9	142.1
	Melanocyte protein PMEL	PMEL	P40967	68.2
	NADH dehydrogenase [ubiquinone] iron-sulfur protein 4. mitochondrial	NDUFS4	O43181	80.5
	Lymphocyte antigen 6D	LY6D	Q14210	47.3
	p53 apoptosis effector related to PMP-22	PERP	Q96FX8	46.5

category	protein description	gene name	accession (UniProt)	MW [kDa]
I	Leucine-rich repeat-containing protein 1	LRRC1	Q9BTT6	39.3
I	AP-1 complex subunit mu-1	AP1M1	Q9BXS5	59.2
I	Calcium-activated chloride channel regulator 2	CLCA2	Q9UQC9	61.2
I	Exocyst complex component 5	EXOC5	O00471	107.5
I	Cytochrome b-c1 complex subunit 8	UQCRQ	O14949	309.2
I	Kallikrein-8	KLK8	O60259	23.5
I	Isocitrate dehydrogenase [NAD] subunit gamma. mitochondrial	IDH3G	P51553	59.9
I	Ribosome biogenesis regulatory protein homolog	RRS1	Q15050	43.4
I	Splicing factor 3B subunit 5	SF3B5	Q9BWJ5	36.7
I	Protein dpy-30 homolog	DPY30	Q9C005	57.7
I	Claudin-1	CLDN1	O95832	58.4
II	Suprabasin	SBSN	Q6UWP8	22.4
II	Protein POF1B	POF1B	Q8WVV4	19.5
II	Involucrin	IVL	P07476	45.1
II	Keratinocyte proline-rich protein	KPRP	Q5T749	38.5
II	Arachidonate 12-lipoxygenase. 12R-type	ALOX12B	O75342	38.4
II	Insulin-degrading enzyme	IDE	P14735	53.3
II	Desmoglein-3	DSG3	P32926	22.4
II	V-type proton ATPase subunit B. brain isoform	ATP6V1B2	P21281	87.6
II	Dynammin-2	DNM2	P50570	134.5
II	Protein S100-A7	S100A7	P31151	118.2
II	Hydroperoxide isomerase ALOXE3	ALOXE3	Q9BYJ1	16.6
II	Actin-related protein 2/3 complex subunit 1A	ARPC1A	Q92747	276.7
II	Kallikrein-7	KLK7	P49862	26.0
II	Transforming acidic coiled-coil-containing protein 2	TACC2	O95359	44.3
II	Casein kinase I isoform alpha	CSNK1A1	P48729	90.9
II	Isoleucine--tRNA ligase. mitochondrial	IARS2	Q9NSE4	46.8
II	Kinesin light chain 3	KLC3	Q6P597	115.2
II	Tumor-associated calcium signal transducer 2	TACSTD2	P09758	18.0
II	Ladinin-1	LAD1	O00515	134.4

category	protein description	gene name	accession (UniProt)	MW [kDa]
II	Mitochondrial proton/calcium exchanger protein	LETM1	O95202	108.8
II	Inositol 1.4.5-trisphosphate receptor type 3	ITPR3	Q14573	26.7
II	26S proteasome non-ATPase regulatory subunit 3	PSMD3	O43242	34.1
II	Corneodesmosin	CDSN	Q15517	77.4
II	60S ribosomal protein L18	RPL18	Q07020	20.2
II	Vacuolar protein sorting-associated protein 4B	VPS4B	O75351	37.5
II	Aldehyde dehydrogenase, dimeric NADP-preferring	ALDH3A1	P30838	36.2
II	Lanosterol synthase	LSS	P48449	80.2
II	Cysteine-rich protein 2	CRIP2	P52943	108.6
II	Structural maintenance of chromosomes protein 1A	SMC1A	Q14683	45.2
II	Serpin B13	SERPINB13	Q9UIV8	33.3
II	Cystatin-M	CST6	Q15828	42.0
II	Succinyl-CoA:3-ketoacid coenzyme A transferase 1, mitochondrial	OXCT1	P55809	36.0
II	Interleukin-1 receptor antagonist protein	IL1RN	P18510	37.5
II	E3 UFM1-protein ligase 1	UFL1	O94874	51.5
II	S-adenosylmethionine synthase isoform type-2	MAT2A	P31153	115.4
II	Four and a half LIM domains protein 2	FHL2	Q14192	51.4
II	Inositol 1.4.5-trisphosphate receptor type 2	ITPR2	Q14571	111.7
II	Protein transport protein Sec23A	SEC23A	Q15436	43.9
II	E3 ubiquitin-protein ligase UBR4	UBR4	Q5T4S7	94.1
II	Calcium-binding mitochondrial carrier protein SCaMC-1	SLC25A24	Q6NUK1	29.0
II	Ribonuclease 7	RNASE7	Q9H1E1	39.1
II	Exocyst complex component 1	EXOC1	Q9NV70	52.5
II	60S ribosomal protein L26-like 1	RPL26L1	Q9UNX3	23.4
II	NHP2-like protein 1	SNU13	P55769	53.1
II	NADH dehydrogenase [ubiquinone] iron-sulfur protein 6, mitochondrial	NDUFS6	O75380	60.9
II	Bifunctional epoxide hydrolase 2	EPHX2	P34913	33.7
II	Ras-related C3 botulinum toxin substrate 3	RAC3	P60763	23.6
II	Prostaglandin reductase 1	PTGR1	Q14914	36.8

category	protein description	gene name	accession (UniProt)	MW [kDa]
II	Electron transfer flavoprotein-ubiquinone oxidoreductase. mitochondrial	ETFDH	Q16134	13.3
II	TOM1-like protein 2	TOM1L2	Q6ZVM7	19.1
II	Nuclear pore complex protein Nup93	NUP93	Q8N1F7	61.0
II	Epidermal growth factor receptor kinase substrate 8-like protein 1	EPS8L1	Q8TE68	10.1
II	Regulator of microtubule dynamics protein 1	RMDN1	Q96DB5	21.6
II	Nectin-4	NECTIN4	Q96NY8	132.7
II	Thioredoxin-related transmembrane protein 1	TMX1	Q9H3N1	33.9
II	DCC-interacting protein 13-alpha	APPL1	Q9UKG1	35.2
II	Loricrin	LOR	P23490	509.8
II	Pro-cathepsin H	CTSH	P09668	21.4
II	Sorting nexin-12	SNX12	Q9UMY4	55.6
II	Syntaxin-binding protein 3	STXBP3	O00186	170.5
II	Transportin-2	TNPO2	O14787	11.5
II	Interferon regulatory factor 6	IRF6	O14896	45.6
II	PDZ domain-containing protein GIPC1	GIPC1	O14908	88.5
II	Glutathione S-transferase A4	GSTA4	O15217	27.5
II	Surfeit locus protein 4	SURF4	O15260	110.3
II	Huntingtin-interacting protein 1-related protein	HIP1R	O75146	105.3
II	Glutaredoxin-3	GLRX3	O76003	21.6
II	Annexin A9	ANXA9	O76027	100.2
II	Integrin alpha-3	ITGA3	P26006	73.7
II	Adenylosuccinate synthetase isozyme 2	ADSS	P30520	33.4
II	40S ribosomal protein S30	FAU	P62861	43.0
II	Uncharacterized protein C6orf132	C6orf132	Q5T0Z8	34.8
II	Estradiol 17-beta-dehydrogenase 8	HSD17B8	Q92506	88.8
II	Protein FAM162A	FAM162A	Q96A26	68.3
II	N-alpha-acetyltransferase 15. NatA auxiliary subunit	NAA15	Q9BXJ9	22.6
II	BolA-like protein 2	BOLA2	Q9H3K6	21.7
II	Ketosamine-3-kinase	FN3KRP	Q9HA64	12.2
II	Vacuolar protein sorting-associated protein 45	VPS45	Q9NRW7	26.8

category	protein description	gene name	accession (UniProt)	MW [kDa]
II	Vacuolar protein sorting-associated protein 18 homolog	VPS18	Q9P253	150.7
II	Serine/threonine-protein kinase 26	STK26	Q9P289	37.6
II	Neudesin	NENF	Q9UMX5	13.1
II	Ribosome maturation protein SBDS	SBDS	Q9Y3A5	33.5
II	Serine/threonine-protein phosphatase 2A 55 kDa regulatory subunit B delta isoform	PPP2R2D	Q66LE6	8.5
II	Serine hydroxymethyltransferase. cytosolic	SHMT1	P34896	15.8
II	Ras-related protein Rab-25	RAB25	P57735	131.5
II	Homeodomain-only protein	HOPX	Q9BPY8	29.8
II	40S ribosomal protein S26	RPS26	P62854	46.5
II	Pirin	PIR	O00625	56.5
II	Syntaxin-7	STX7	O15400	74.4
II	Eukaryotic translation elongation factor 1 epsilon-1	EEF1E1	O43324	60.8
II	Synaptogyrin-2	SYNGR2	O43760	35.7
II	Mitochondrial import inner membrane translocase subunit Tim8 A	TIMM8A	O60220	40.5
II	CAAX prenyl protease 1 homolog	ZMPSTE24	O75844	82.5
II	CD59 glycoprotein	CD59	P13987	34.3
II	DNA replication licensing factor MCM2	MCM2	P49736	42.8
II	Succinate-semialdehyde dehydrogenase. mitochondrial	ALDH5A1	P51649	74.1
II	Serine/threonine-protein kinase PAK 2	PAK2	Q13177	103.9
II	BRO1 domain-containing protein BROX	BROX	Q5VW32	21.8
II	Metallo-beta-lactamase domain-containing protein 2	MBLAC2	Q68D91	54.1
II	Basic leucine zipper and W2 domain-containing protein 1	BZW1	Q7L1Q6	58.9
II	Ceramide synthase 3	CERS3	Q8IU89	51.4
II	Glutamine amidotransferase-like class 1 domain-containing protein 1	GATD1	Q8NB37	40.6
II	Neurobeachin	NBEA	Q8NFP9	70.2
II	Thiosulfate sulfurtransferase/rhodanese-like domain-containing protein 1	TSTD1	Q8NFU3	19.7
II	5'(3')-deoxyribonucleotidase. cytosolic type	NT5C	Q8TCD5	42.8
II	Nicastrin	NCSTN	Q92542	68.4
II	Coiled-coil domain-containing protein 47	CCDC47	Q96A33	50.3
II	Prefoldin subunit 5	PFDN5	Q99471	12.5

category	protein description	gene name	accession (UniProt)	MW [kDa]
II	Microsomal glutathione S-transferase 2	MGST2	Q99735	48.6
II	Haloacid dehalogenase-like hydrolase domain-containing protein 3	HDHD3	Q9BSH5	22.3
II	SRA stem-loop-interacting RNA-binding protein. mitochondrial	SLIRP	Q9GZT3	42.0
II	Phospholysine phosphohistidine inorganic pyrophosphate phosphatase	LHPP	Q9H008	67.0
II	Protein argonaute-4	AGO4	Q9HCK5	97.6
II	Gephyrin	GPHN	Q9NQX3	47.8
II	H/ACA ribonucleoprotein complex subunit 2	NHP2	Q9NX24	16.4
II	Costars family protein ABRACL	ABRACL	Q9P1F3	122.6
II	GMP reductase 2	GMPR2	Q9P2T1	42.9
II	Junctional adhesion molecule A	F11R	Q9Y624	112.0
II	Basic leucine zipper and W2 domain-containing protein 2	BZW2	Q9Y6E2	26.9
II	Caspase recruitment domain-containing protein 18	CARD18	P57730	42.2
II	UBX domain-containing protein 1	UBXN1	Q04323	20.7
II	Proteolipid protein 2	PLP2	Q04941	106.3
II	Protein Red	IK	Q13123	39.6
II	Optic atrophy 3 protein	OPA3	Q9H6K4	27.1
II	Mast/stem cell growth factor receptor Kit	KIT	P10721	86.4
II	Protein transport protein Sec61 subunit gamma	SEC61G	P60059	29.6
II	Cyclin-dependent-like kinase 5	CDK5	Q00535	15.7
II	Methylsterol monooxygenase 1	MSMO1	Q15800	52.7
II	HD domain-containing protein 2	HDDC2	Q7Z4H3	108.7
II	COMM domain-containing protein 2	COMMD2	Q86X83	22.2
II	N-terminal Xaa-Pro-Lys N-methyltransferase 1	NTMT1	Q9BV86	46.7
II	Charged multivesicular body protein 4a	CHMP4A	Q9BY43	54.0
II	Cornifelin	CNFN	Q9BYD5	21.6
II	pre-mRNA 3' end processing protein WDR33	WDR33	Q9C0J8	28.5
II	Sialate O-acetyltransferase	SIAE	Q9HAT2	24.1
II	40S ribosomal protein S29	RPS29	P62273	47.6
II	Endoribonuclease LACTB2	LACTB2	Q53H82	46.5
II	Cornulin	CRNN	Q9UBG3	151.4

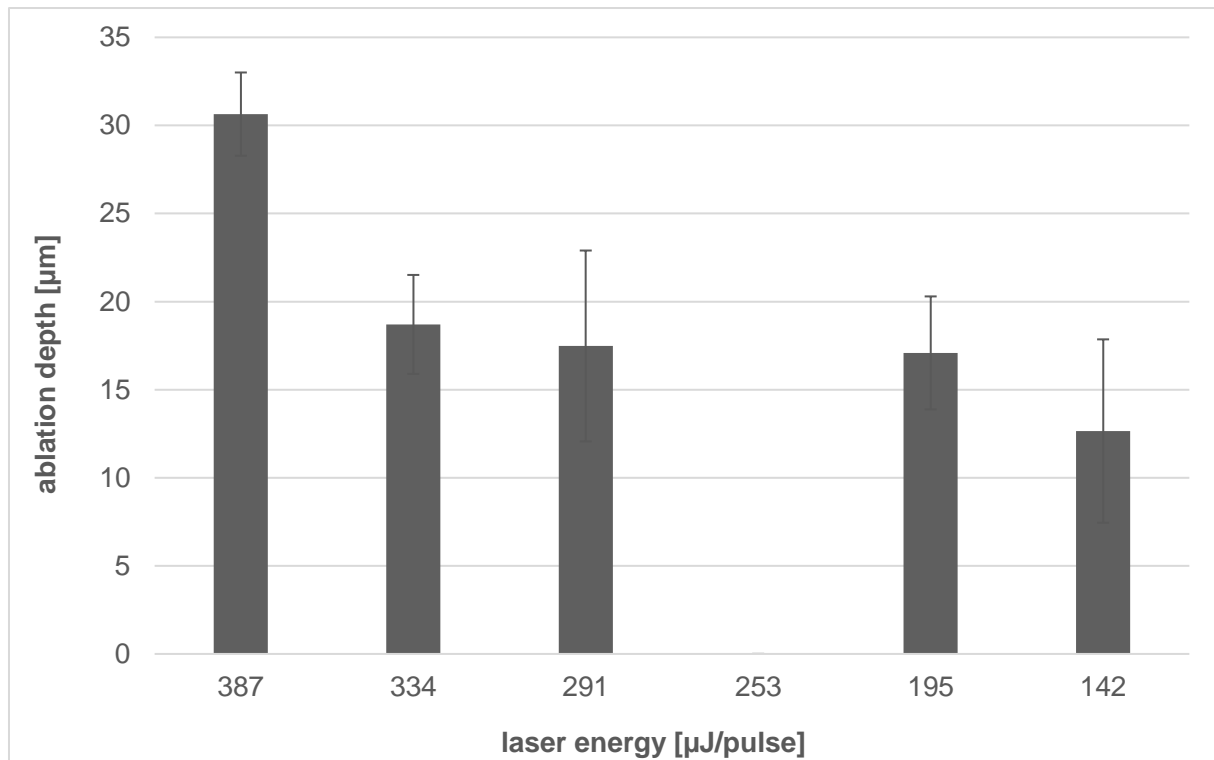
category	protein description	gene name	accession (UniProt)	MW [kDa]
III	Envoplakin	EVPL	Q92817	65.6
III	Protein-glutamine gamma-glutamyltransferase K	TGM1	P22735	24.6
III	Serpin B3	SERPINB3	P29508	85.2
III	Arginase-1	ARG1	P05089	47.1
III	Plasminogen activator inhibitor 2	SERPINB2	P05120	59.0
III	Phenylalanine--tRNA ligase beta subunit	FARSB	Q9NSD9	19.9
III	Exportin-2	CSE1L	P55060	24.6
III	Phosphoserine aminotransferase	PSAT1	Q9Y617	53.5
III	40S ribosomal protein S11	RPS11	P62280	28.4
III	Peptidyl-prolyl cis-trans isomerase FKBP4	FKBP4	Q02790	59.1
III	Heterochromatin protein 1-binding protein 3	HP1BP3	Q5SSJ5	40.8
III	rRNA 2'-O-methyltransferase fibrillar	FBL	P22087	13.4
III	Heat shock 70 kDa protein 4L	HSPA4L	O95757	41.3
III	Prostatic acid phosphatase	ACPP	P15309	109.9
III	Cytosolic phospholipase A2 zeta	PLA2G4F	Q68DD2	82.5
III	Ras-related protein Rab-18	RAB18	Q9NP72	7.3
III	Adenylate kinase 4. mitochondrial	AK4	P27144	97.5
III	Sorting nexin-6	SNX6	Q9UNH7	74.0
III	Very-long-chain 3-oxoacyl-CoA reductase	HSD17B12	Q53GQ0	27.9
III	Ras-related protein Rab-2B	RAB2B	Q8WUD1	16.6
III	Gamma-butyrobetaine dioxygenase	BBOX1	O75936	112.3
III	Polyadenylate-binding protein 4	PABPC4	Q13310	55.1
III	Triokinase/FMN cyclase	TKFC	Q3LXA3	79.7
III	Sorting nexin-2	SNX2	O60749	70.9
III	Kinesin-like protein KIF13B	KIF13B	Q9NQT8	55.7
III	Very-long-chain enoyl-CoA reductase	TECR	Q9NZ01	22.7
III	SUMO-activating enzyme subunit 2	UBA2	Q9UBT2	51.8
III	40S ribosomal protein S4. Y isoform 2	RPS4Y2	Q8TD47	12.3
III	Inositol monophosphatase 2	IMPA2	O14732	47.4
III	Potassium-transporting ATPase alpha chain 2	ATP12A	P54707	266.8
III	F-box only protein 50	NCCRP1	Q6ZVX7	25.1

category	protein description	gene name	accession (UniProt)	MW [kDa]
III	Cleavage and polyadenylation specificity factor subunit 5	NUDT21	O43809	54.4
III	Protein diaphanous homolog 1	DIAPH1	O60610	25.2
III	Carnitine O-palmitoyltransferase 2. mitochondrial	CPT2	P23786	15.5
III	Twinfilin-1	TWF1	Q12792	99.9
III	Calcium-binding mitochondrial carrier protein Aralar2	SLC25A13	Q9UJS0	40.7
III	Ankyrin repeat domain-containing protein 22	ANKRD22	Q5VYY1	67.8
III	Methylmalonyl-CoA mutase. mitochondrial	MUT	P22033	30.2
III	60S ribosomal protein L29	RPL29	P47914	132.8
III	60S ribosomal protein L19	RPL19	P84098	9.5
III	Protein bicaudal D homolog 2	BICD2	Q8TD16	21.3
III	Golgi resident protein GCP60	ACBD3	Q9H3P7	15.0
III	Casein kinase II subunit alpha 3	CSNK2A3	Q8NEV1	42.2
III	Potassium-transporting ATPase alpha chain 1	ATP4A	P20648	24.7
III	2'.3'-cyclic-nucleotide 3'-phosphodiesterase	CNP	P09543	49.2
III	V-type proton ATPase subunit B. kidney isoform	ATP6V1B1	P15313	222.4
III	Ras-related protein Rab-3A	RAB3A	P20336	97.7
III	Plasma membrane calcium-transporting ATPase 2	ATP2B2	Q01814	76.7
III	Inositol 1.4.5-trisphosphate receptor type 1	ITPR1	Q14643	55.4
III	Y-box-binding protein 2	YBX2	Q9Y2T7	51.3
III	Choline-phosphate cytidylyltransferase B	PCYT1B	Q9Y5K3	38.5
III	Rootletin	CROCC	Q5TZA2	119.8
III	Programmed cell death protein 10	PDCD10	Q9BUL8	61.6
III	Clustered mitochondria protein homolog	CLUH	O75153	30.6
III	4F2 cell-surface antigen heavy chain	SLC3A2	P08195	14.5
III	DNA replication licensing factor MCM3	MCM3	P25205	52.2
III	Probable global transcription activator SNF2L1	SMARCA1	P28370	28.6
III	Cornifin-A	SPRR1A	P35321	40.0
III	Short/branched chain specific acyl-CoA dehydrogenase. mitochondrial	ACADSB	P45954	55.5
III	Rho-related GTP-binding protein RhoG	RHOG	P84095	87.3
III	Adenosylhomocysteinase 3	AHCYL2	Q96HN2	12.1

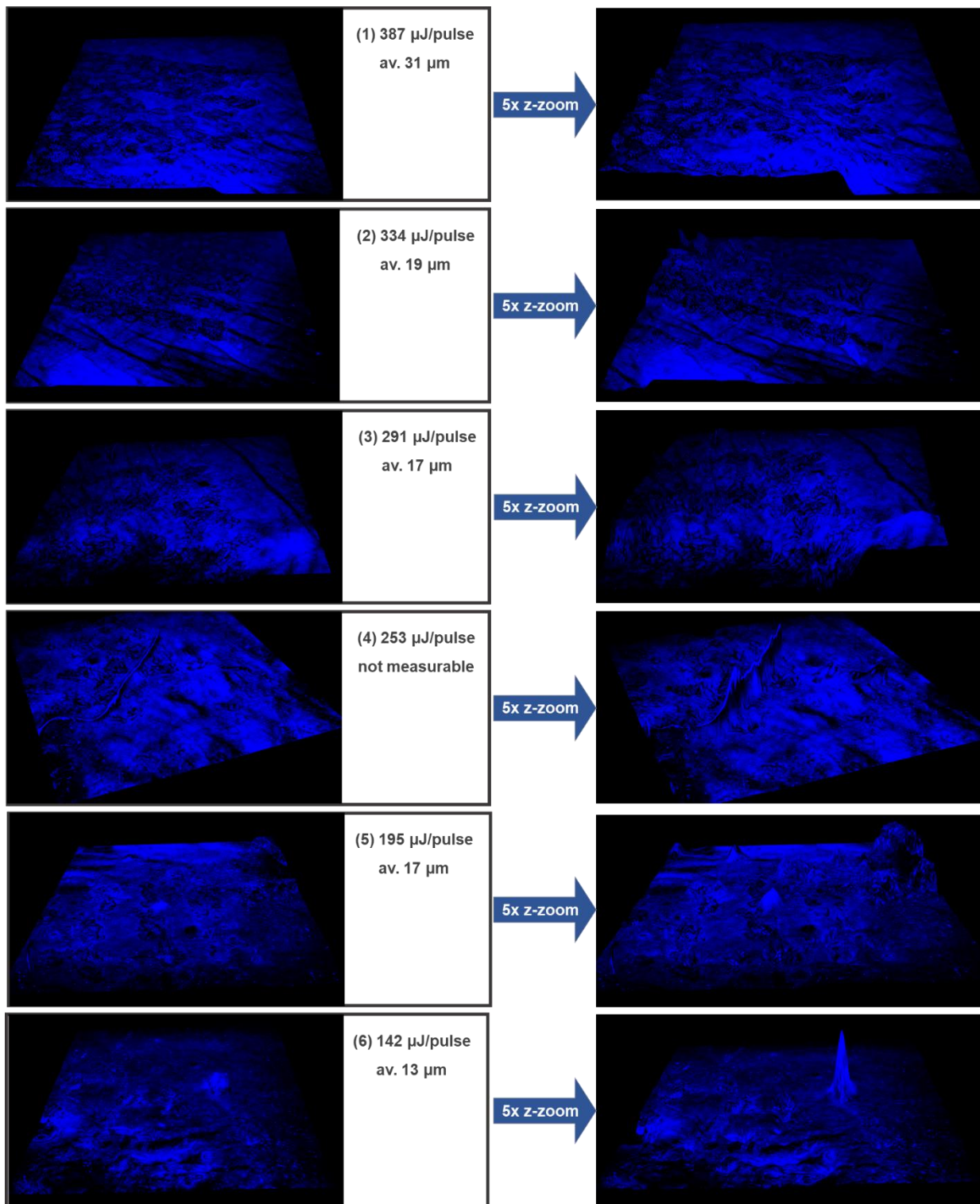
category	protein description	gene name	accession (UniProt)	MW [kDa]
III	Bcl-2-like protein 13	BCL2L13	Q9B XK5	28.0
III	Tight junction protein ZO-2	TJP2	Q9UDY2	11.6
III	Protein SGT1 homolog	SUGT1	Q9Y2Z0	34.6
III	NADH dehydrogenase [ubiquinone] 1 beta subcomplex subunit 9	NDUFB9	Q9Y6M9	33.7
III	Splicing factor 3B subunit 6	SF3B6	Q9Y3B4	25.4
III	Spermidine synthase	SRM	P19623	57.5
III	Tyrosine-protein phosphatase non-receptor type 11	PTPN11	Q06124	40.3
III	Protein PAXX	PAXX	Q9BUH6	21.4
III	2'-deoxynucleoside 5'-phosphate N-hydrolase 1	DNPH1	O43598	123.3
III	Prefoldin subunit 1	PFDN1	O60925	42.8
III	Ras GTPase-activating-like protein IQGAP3	IQGAP3	Q86VI3	29.8
III	5-oxoprolinase	OPLAH	O14841	92.4
III	Syntaxin-binding protein 2	STXBP2	Q15833	27.3
III	Tubulin polymerization-promoting protein	TPPP	O94811	143.1
III	Keratin. type II cuticular Hb2	KRT82	Q9NSB4	15.3
III	Abl interactor 2	ABI2	Q9NYB9	12.5
III	Charged multivesicular body protein 5	CHMP5	Q9NZZ3	30.6
III	Adseverin	SCIN	Q9Y6U3	189.2
III	Unconventional myosin-VI	MYO6	Q9UM54	22.8
III	Inositol monophosphatase 1	IMPA1	P29218	73.4
III	Vacuolar protein sorting-associated protein VTA1 homolog	VTA1	Q9NP79	65.7
III	Death-associated protein-like 1	DAPL1	A0PJW8	468.8
III	Hepatocyte growth factor-regulated tyrosine kinase substrate	HGS	O14964	46.5
III	Protein XRP2	RP2	O75695	24.6
III	GTPase KRas	KRAS	P01116	40.1
III	Syndecan-1	SDC1	P18827	51.1
III	N(4)-(beta-N-acetylglucosaminyl)-L-asparaginase	AGA	P20933	34.6
III	Grancalcin	GCA	P28676	50.6
III	Basigin	BSG	P35613	43.7
III	Glutamate--cysteine ligase catalytic subunit	GCLC	P48506	8.7

category	protein description	gene name	accession (UniProt)	MW [kDa]
III	PDZ and LIM domain protein 4	PDLIM4	P50479	33.9
III	Hexokinase-2	HK2	P52789	20.5
III	Epididymal secretory protein E1	NPC2	P61916	47.4
III	AP-1 complex subunit sigma-1A	AP1S1	P61966	37.1
III	RNA-binding protein with serine-rich domain 1	RNPS1	Q15287	65.9
III	Protein transport protein Sec23B	SEC23B	Q15437	33.3
III	Vacuolar protein sorting-associated protein 26B	VPS26B	Q4G0F5	22.3
III	Coiled-coil domain-containing protein 58	CCDC58	Q4VC31	82.5
III	Ras-related GTP-binding protein A	RRAGA	Q7L523	28.0
III	Ubiquitin recognition factor in ER-associated degradation protein 1	UFD1	Q92890	60.2
III	DCN1-like protein 1	DCUN1D1	Q96GG9	26.3
III	Erbin	ERBIN	Q96RT1	23.3
III	Phosphatidylinositol 4-kinase type 2-alpha	PI4K2A	Q9BTU6	44.6
III	Gasdermin-C	GSDMC	Q9BYG8	39.1
III	Acyl-coenzyme A thioesterase 13	ACOT13	Q9NPJ3	14.2
III	[Pyruvate dehydrogenase [acetyl-transferring]]-phosphatase 1, mitochondrial	PDP1	Q9P0J1	55.7
III	Signal recognition particle subunit SRP68	SRP68	Q9UHB9	13.7
III	Ubiquitin-fold modifier-conjugating enzyme 1	UFC1	Q9Y3C8	10.1
III	Vascular endothelial growth factor receptor 3	FLT4	P35916	87.2
III	Mannose-P-dolichol utilization defect 1 protein	MPDU1	O75352	81.8
III	UDP-glucose:glycoprotein glucosyltransferase 2	UGGT2	Q9NYU1	14.2
III	Trichohyalin	TCHH	Q07283	6.6
III	Septin-4	Sep 04	O43236	67.6
III	Vascular endothelial growth factor receptor 2	KDR	P35968	113.0
III	Cysteine dioxygenase type 1	CDO1	Q16878	23.5
III	Polyadenylate-binding protein 1-like 2	PABPC1L2A	Q5JQF8	151.8
III	RNA-binding Raly-like protein	RALYL	Q86SE5	42.8
III	Protein MAL2	MAL2	Q969L2	44.4
III	Endophilin-A1	SH3GL2	Q99962	47.8
III	HLA class II histocompatibility antigen. DRB1-14 beta chain	HLA-DRB1	Q9GIY3	60.2

category	protein description	gene name	accession (UniProt)	MW [kDa]
III	Probable ATP-dependent RNA helicase DDX4	DDX4	Q9NQI0	45.0
III	Cytochrome P450 4F22	CYP4F22	Q6NT55	32.1
III	Small acidic protein	SMAP	O00193	89.7
III	Enoyl-CoA delta isomerase 2. mitochondrial	ECI2	O75521	94.5
III	Guanine nucleotide-binding protein G(I)/G(S)/G(T) subunit beta-3	GNB3	P16520	42.1
III	Gamma-aminobutyric acid receptor-associated protein-like 2	GABARAPL2	P60520	146.6
III	ER membrane protein complex subunit 2	EMC2	Q15006	57.8
III	Ras-related GTP-binding protein B	RRAGB	Q5VZM2	14.2
III	Eukaryotic peptide chain release factor GTP-binding subunit ERF3B	GSPT2	Q8IYD1	31.3
III	G-protein coupled receptor 98	GPR98	Q8WYG9	24.9
III	DDRKG domain-containing protein 1	DDRKG1	Q96HY6	123.4
III	Nuclear distribution protein nudE homolog 1	NDE1	Q9NXR1	31.4
III	Serine/threonine-protein kinase NLK	NLK	Q9UBE8	69.0
III	Protein MEMO1	MEMO1	Q9Y316	32.0
III	Caspase recruitment domain-containing protein 16	CARD16	Q5EG05	55.9



S. 7: Linear correlation of laser energy setting parameter and the determined PIRL ablation depth with the aid of confocal laser scanning microscopy using collagen autofluorescence measurement. The six adjusted laser energies amounted to (1) 387 μJ/pulse; (2) 334 μJ/pulse; (3) 291 μJ/pulse; (4) 253 μJ/pulse; (5) 195 μJ/pulse; (6) 142 μJ/pulse. The bar chart diagram shows the ablation depth in μm for each ablated area of 200 μm dermatome skin biopsy with a certain laser pulse energy, additionally the corresponded standard deviation within the five measured spots.



S. 8: Confocal laser scanning microscopy images using Hoechst 33342 fluorescence - representing the nuclei of the cells - of ablated 200 μm dermatome skin biopsy to optimize the PIRL setting parameters. The six microscopy images represent the remained structure on skin after PIRL ablation using three different laser energies: (1) 144 $\mu\text{J}/\text{pulse}$; (2) 166 $\mu\text{J}/\text{pulse}$; (3) 184 $\mu\text{J}/\text{pulse}$. Each energy set-up was repeated twice (1a & 1b; 2a & 2b; 3a & 3b). Left: microscopy images of ablated areas; right: microscopy images of ablated areas with the five-fold zoom in the z-axial for realizing the 3D representation.

9 Acknowledgment

Foremost, I would like to thank all the people who helped me in the completion of this thesis.

At this point, I would like to express my sincere gratitude to my supervisor Prof. Dr. Hartmut Schlüter for giving me this interesting thesis topic and the opportunity of working in his fantastic group (at Universitätsklinikum Hamburg-Eppendorf - UKE). With his continuous support through my Ph.D study and research, his guidance and immense knowledge, he accompanied me in all the time of my research.

Besides my supervisor, I would like to sincerely thank my co-supervisor Prof. Dr. Dr. Christian Betzel (at University Hamburg) for his insightful encouragement.

My special thanks go to my advisor in Beiersdorf, Dr. J Hendrik Reuter, for his helpful supports and the interesting and motivating discussions. In that case, I'd like to give many thanks to the working group of Dr. Reuter at Beiersdorf, Dr. Tanja Bußmann, Julia Heusel, Wilfried Siefken, and the other member of the group for their support for sample preparation and microscopy at all time in their laboratory.

My sincere thanks also go to Dr. Nils Owe Hansen, my physicist college from Center for Free Electron Laser Science (CFEL), for helping me through all my experiments at PIRL system, and well as to Dr. Dennis Eggert, Heinrich Pette Institute (HPI), for preparing all confocal laser microscopy data in my thesis.

Also, I am grateful to Sönke Harder for his always support in the laboratory and Core Facility affairs. I would like to say thank you to all of our group members, Fritz, Yudong, Christoph, David, Andrey, Christine, Lorena, Laura, Pascal, Markus, Refat, Marcel, Dennis and Benjamin for the nice atmosphere in our lab.

My dear Manka, I don't know how to thank you for all your mental support during my time at UKE and especially editing my thesis. So happy to have you as a friend and will never forget the enjoyable time we had together. I am thankful to Maryam, my friend, for the fun times inside and outside the office and all sentimental memories.

Last but not least, I would like to thank my family, my lovely mother and my lovely father, my brother Ali, my little sister Minoo and my fiancé Slava, who have encouraged and supported me in all my decisions, and they gave me strength with their infinite loves throughout my life.

10 Declaration

Declaration on oath

I hereby declare, on oath, that I have written the present dissertation by my own and have not used other than the acknowledged resources and aids. The submitted written version corresponds to the version on the electronic storage medium. Additionally, I hereby declare that this content or parts of this thesis in this or similar form have not been presented to any other examination authority and have not been published. I have not previously applied or pursued for a doctorate (Ph.D. studies).

Eidesstattliche Versicherung

Hiermit versichere ich an Eides statt, dass ich die vorliegende Dissertationsschrift selbst verfasst und keine anderen als die angegebenen Quellen und Hilfsmittel benutzt habe. Die eingereichte schriftliche Fassung entspricht der auf dem elektronischen Speichermedium. Außerdem versichere ich, dass diese Arbeit in gleicher oder ähnlicher Form noch nie einer Prüfungsstelle zur Erlangung des Doktorgrades vorgelegt wurde. Es wurden keine früheren Promotionsversuche meinerseits unternommen.

Hamburg, 14.01.2019

city and date

signature